Decoupled Electrolysis Using Silicotungstic Acid as a Redox Mediator for Zero-Carbon Hydrogen Production

Mbang Eze Obeten

Submitted in fulfilment of the requirements for the

Degree of Doctor of Philosophy

School of Chemistry

College of Science and Engineering

University of Glasgow

July, 2025

ABSTRACT

Water electrolysis for hydrogen production has substantial potential to address the current energy crisis while mitigating environmental pollution. However, achieving truly green hydrogen production requires using materials better suited to intermittent power generation, as existing systems pose serious concerns over gas mixing and cell component degradation. This thesis examines the concept of decoupled water electrolysis, utilising silicotungstic acid ($H_4SiW_{12}O_{40}$) as a redox mediator in a flow-cell system to generate hydrogen. Decoupled electrolysis offers exceptional flexibility by enabling the separate production of hydrogen and oxygen at different times and rates, reducing gas crossover issues to a minimum.

Chapter 1 explores the green hydrogen production route in a net-zero world and the various methods employed in green hydrogen production. Furthermore, we introduce the concept of decoupled water electrolysis, an emerging approach for green hydrogen production via electrochemical processes, and discuss how it can potentially address some of the challenges associated with renewable-driven hydrogen production.

Chapter 2 provides background information on the theory underlying the experimental techniques used throughout this study. Various electrochemical and analytical methods were employed to monitor changes in potential, current, charge passed, and the electrode surface during the reduction of the redox mediator.

Chapter 3 highlights the application of decoupled water electrolysis in a flow system using silicotungstic acid as the redox mediator by assembling two electrochemical cells for hydrogen production (mediator re-oxidation) and oxygen production (mediator reduction) while applying a range of commercially relevant current densities (0.05–1.35 A/cm^2) to monitor the liquid mediator behaviour as it was circulated continuously between the two cells as hydrogen was produced.

In Chapter 4, regenerated cellulose dialysis membranes were employed in the oxygen-generating cell, in order to compare the resulting electrochemical system with the one from Chapter 3 (which used only perfluorinated membranes). A comparative analysis of the membrane (before vs after electrolysis), current density, and the decoupling efficiency (%) obtained in this section was conducted.

Chapter 5 contains overall conclusions and discusses future work. It provides a summary of the work and suggestions for future research.

TABLE OF CONTENTS

CHAPTER TWO: EXPERIMENTAL TECHNIQUES/METHODOLOGY

CHAPTER THREE: DECOUPLED WATER ELECTROLYSIS AT HIGH CURRENT DENSITIES USING A SOLUTION-PHASE REDOX MEDIATOR

List of Publications

- **Obeten M. E.** Zeliha Ertekin and Mark D. Symes. Decoupled water electrolysis at high current densities using a solution-phase redox mediator.
  ACS Energy Fuels, **2025,** 39, 7129−7136.

- **Obeten M. E.** Zeliha Ertekin, Paula L. Lalaguna, Malcolm Kadodwala and Mark D. Symes. Solution-phase decoupled water electrolysis in a flow cell with a simple size exclusion membrane separator.
  Available at SSRN 5609435, 2025.

List of Conferences, Workshops, and Courses

- International Network of Polyoxometalate Science (INPOMS), University of Newcastle, UK, 13th - 14th March 2025.
  Oral presentation: "Decoupled water electrolysis using silicotungstic acid as a redox mediator".

- Royal Society Chemistry Electrochem International conference, University of Bristol, UK, 10th -12th September 2023.
  Poster Presentation: "Decoupled water electrolysis using silicotungstic acid as a redox mediator".

- Cryogenic safety training, School of Chemistry, University of Glasgow, UK, 10th February 2022.

- Graduate Employability masterclass workshop, University of Glasgow, UK, 2&3 - 2nd March 2022.

- Royal Society of Chemistry Electrochem International conference, University of Edinburgh – 5th – 7th September 2022.
  Poster Presentation: "Decoupled water electrolysis using silicotungstic acid as a redox mediator".

- Introduction to Research Impact – 15th May 2023.

- Introduction to Python – University of Glasgow, 9th – 13th June 2025.

Acknowledgements

Firstly, I would like to express my profound gratitude to God Almighty for his divine grace throughout my studies.

I want to express my sincere appreciation to my able project supervisor, Professor Mark D. Symes, for his continuous support, motivation, and guidance; for introducing me to new ideas throughout this project; and for providing me with the opportunity to explore the exciting field of Decoupled water electrolysis. I believe I have been extremely fortunate to have met such a wonderful person, an exemplary role model, and I will always remain grateful. I aspire to one day influence someone else's career in the way he has influenced mine.

Also, I want to say a very big thank you to the Symes group family for their hospitality and assistance, despite their busy schedules. Specifically, I would like to thank Dr Zeliha Ertekin for all the assistance throughout this project. She is always available to everyone. I also want to thank all the former members of the Symes group for making my time here enjoyable. They have always been ready to lend a helping hand or provide much-appreciated advice. I also remember my great friend Hossam of blessed memory.

A very special thanks to my sponsors (TETFUND and the University of Cross River State, Nigeria) for their strong belief in my potential. I dedicate this work to my parents, special thanks to my lovely wife, siblings, friends, my children, and my age grade (Kedei, Ketadi, Kofonohnoh).

I am entirely grateful for the pleasant working environment at the School of Chemistry and the University of Glasgow as a whole. I want to extend special thanks to everyone in the A4-39 laboratory for their unwavering support, as well as to the entire management of the School of Chemistry. It's been my pleasure working with you all.

Author's declaration

I declare that, except where explicit reference is made to the contribution of others, this thesis is the result of my own work and has not been submitted for any other degree at the University of Glasgow or any other institution.

I declare that this thesis has been produced under the University of Glasgow's Code of Good Practice in Research.

I acknowledge that if any issues are raised regarding good research practice based on the thesis review, the examination may be postponed pending the outcome of any investigation into these concerns.

Printed name: Mbang Eze Obeten

Signature:

List of Abbreviations and Symbols

AEM Anion Exchange Membrane

AED Atomic Emission Detectors

AFM Atomic Force Microscopy

AWE Alkaline Water Electrolysis

AQDS Anthraquinone 2,7-Sulfonate Acid

CCM Catalyst-Coated Membrane

CPE Controlled Potential Electrolysis

CV Cyclic Voltammetry

DHPS Dihydroxy-2-phenylsulfonic Acid

ECPB Electron Coupled Proton Buffer

ECD Electron Capture Detector

ESG Environmental, Social and Governance

ESS Energy Storage Systems

FID Flame Ionisation Detector

GDL Gas Diffusion Layer

HES Heating Energy Systems

HER Hydrogen Evolution Reaction

HQMS Hydroquinone Monosulfate

MEA Membrane Electrode Assembly

Mt Million tonne

NZE Net Zero Emission

OER Oxygen Evolution Reaction

PEM Proton Exchange Membrane

PMA Phosphomolybdic Acid

PID Photoionisation Detectors

POX Partial oxidation

PTFE Polytetrafluoroethylene

PV Photovoltaic

RESS Renewable Energy Storage Systems

SCOT Support Coated Open Tubular

SDG Sustainable Development Goals

SHE Standard Hydrogen Electrode

SMR Steam Methane Reforming

SOE Solid Oxide Electrolysers

SR Steam Reforming

STA Silicotungstic Acid

TCD Thermal Conductivity Detectors

TMQ Trimethyl-1,2-dihydroquinoline

UN United Nations

WCOT Wall-Coated Open Tubular

WGS Water Gas Shift

CHAPTER ONE

1.1. INTRODUCTION

The world's population is growing steadily, requiring an increasing supply of green energy. Green hydrogen production is essential for advancing sustainable energy systems and achieving a low-carbon economy. Various production methods have been developed, each with distinct technological characteristics, efficiency levels, and environmental impacts.[1] However, most hydrogen is currently produced from natural gas through steam reforming and coal gasification.[1] These hydrocarbon resources are non-renewable and generate greenhouse gases as by-products. For each ton of hydrogen produced by steam methane reforming, approximately 9-10 tons of equivalent carbon dioxide are released into the atmosphere, with long-term environmental effects.[2]

Energy conversion for green hydrogen production primarily involves electrolysis, which converts renewable energy sources (such as solar, wind, or hydro) into hydrogen gas by splitting water molecules into hydrogen and oxygen.[3] This process, often referred to as Power-to-Gas, converts surplus renewable energy into a storable and transportable fuel, producing green hydrogen without generating greenhouse gas emissions, making it a key technology for a carbon-neutral energy system. [3] Energy storage systems (ESS) can be used to balance electrical energy supply and demand. The process involves converting and storing electrical energy from an available source into another form of energy, which can be converted back into electrical energy when needed. The forms of energy storage conversion can be chemical, mechanical, or thermal.[3] Researchers and scientists have classified energy storage technologies based on diverse approaches currently deployed worldwide. Each technology has trade-offs in terms of cost, efficiency, duration, and scalability.[4] Lithium-ion batteries dominate short-term storage, while pumped hydro remains the most widely used solution for long-duration storage.[4] Hydrogen has great potential to be an essential part of a future energy system that is clean, secure, and cost-effective. Its versatility enables renewables such as wind and solar photovoltaic (PV) to contribute more significantly to a sustainable economy.[4,5] This is because the green hydrogen produced by electrolysis can serve as a storage medium for renewable energy.[5] In contrast, the surplus electricity from wind and solar plants must be stored for later use. Electricity from green sources can be used for electrolysis to split water molecules and

produce hydrogen. This hydrogen can, in turn, be used as an energy storage medium, stored in tanks or even underground caves, and transported via pipelines, tankers, or trucks. Hydrogen technology offers renewable energy plants the possibility to generate and store surplus energy produced under favourable weather conditions. [5]

Clean hydrogen is gaining significant attention and support, with an increasing number of global projects and policies being developed. This is because hydrogen has the potential to address a range of energy challenges, including reducing emissions, particularly in industries such as iron and steel, chemicals, and long-distance transportation.[6] It has a variety of uses and applications, for example, in the production of fertilisers and the oil refining sector. Hydrogen aligns with the United Nations' environmental, social, and governance (ESG) principles, as its use is environmentally friendly, socially beneficial, and economically viable. In addition, hydrogen can help achieve several United Nations (UN) Sustainable Development Goals (SDGs), including SDG 7 (Clean and affordable energy), SDG 13 (Climate Action), and SDG 17 (Partnerships for the Goals).[4-7] Moreover, hydrogen production from renewable power processes may become more cost-effective due to the recent sharp decline in the costs of renewable energy. Governments worldwide have adopted hydrogen policies, leading to the development of low-carbon hydrogen generation and related policy initiatives. Fig. 1.1 illustrates the estimated global hydrogen demand by sectors and by region from 2020 to 2025.[6]

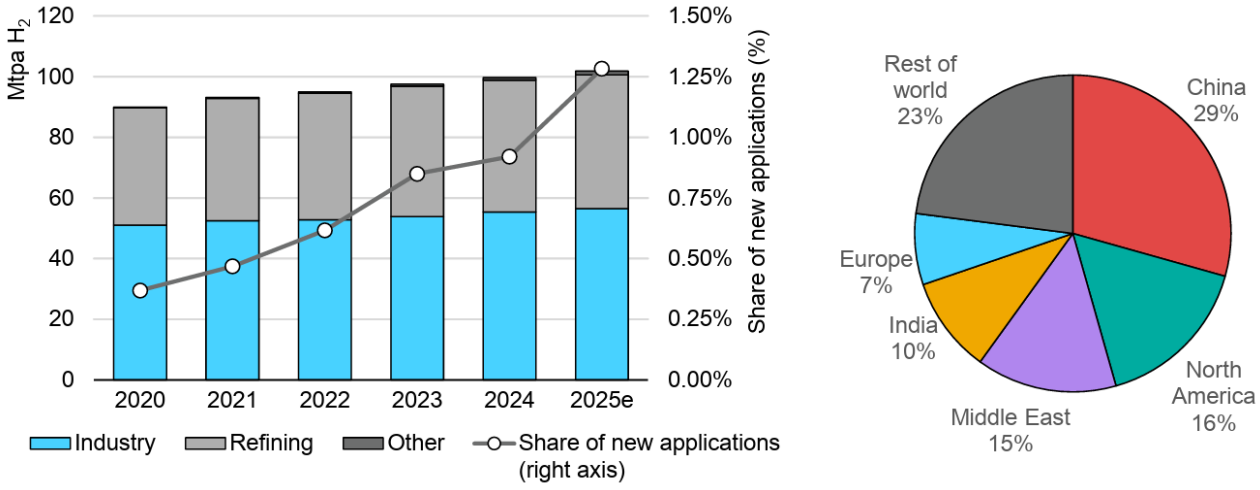

Figure 1.1. *Global Hydrogen demand by sectors (left) and hydrogen use by region (right). "Other" includes transport, power generation, production of hydrogen-based fuels, buildings and biofuels upgrading. The estimated value for 2025 (2025e) is a projection based on trends observed up to August 2025.* ***Sources:*** *IEA* Hydrogen. https://www.iea.org/reports/hydrogen.

Fig. 1.1 illustrates that Global hydrogen consumption reached almost 100 Mt in 2024, just over 2% more than in 2023. This decades-long upward trajectory shows no sign of changing;[6] it was estimated that global hydrogen demand is set to exceed 100 Mt for the first time in 2025.[1,6]

Hydrogen demand by region remained largely consistent with that of previous years. China was the largest consumer, accounting for more than one-quarter of total demand at 29 Mt, almost twice that of North America, the second-largest user with around 16 Mt. China and North America experienced modest growth (2% and 0.5%, respectively), while Europe's demand remained almost the same as in 2023. The Middle East and India experienced more pronounced increases, nearly 6% and over 4%, respectively, primarily attributed to increased use in refining and chemical production, as well as in steel production. Demand growth continues to be driven primarily by established industrial sectors utilising hydrogen as a feedstock, rather than by policies aimed at promoting low-emissions hydrogen to reduce emissions and enhance energy security.[5,6] Demand remains concentrated in traditional uses: oil refining, chemical manufacturing (notably ammonia and methanol production), and steel-making processes using fossil-derived synthesis gas. Demand for new applications increased less than in previous years (primarily driven by the use of hydrogen in biofuel production) and accounts for less than 1% of global hydrogen demand.[6] In addition, nearly all of this demand was met by hydrogen produced from unabated fossil fuels.[6,8]

The widespread use of hydrogen in global energy transitions faces several challenges, including the slow development of hydrogen infrastructure, which prevents its widespread adoption. Furthermore, producing hydrogen from low-carbon energy sources is currently too expensive, and as a result, hydrogen is almost entirely supplied by natural gas and coal at present. Currently, regulations are also hindering the development of a clean hydrogen industry.[9] One major issue is that many regulatory frameworks are still structured around traditional fossil fuel-based energy systems, making it difficult for hydrogen projects to fit within existing policies.[10] Moreover, the complexity of hydrogen regulations has been criticised for being overly complex, which slows down investment decisions and project approvals. In Europe, for example, 90% of hydrogen projects remain in the pre-final investment decision phase due to a lack of long-term regulatory clarity.[10-15] Another challenge is the absence of harmonised international standards for green hydrogen certification, which complicates cross-border trade and investment.[11] Without clear definitions and consistent policies, businesses struggle to secure funding and scale up production. Governments are working to address these challenges, with initiatives like the UK's Hydrogen Production Business Model, which provides revenue

support to hydrogen facilities.[12] However, more streamlined and supportive regulations are needed to accelerate the transition to green hydrogen as a viable energy source.

Water electrolysis is considered one of the most efficient and reliable approaches to producing green hydrogen from renewable energy, particularly for grid-scale energy storage, as the electrolysis of water at room temperature stands out as a scalable technology that requires only water and energy (in the form of electricity) as inputs.[12,13] Some advantages of using hydrogen over conventional fuels include high theoretical energy density, theoretically unlimited availability, and its inoffensive combustion product, water (H_2O). Still, their application remains hampered by the high cost of the cell components, such as catalysts and membranes.[8] Furthermore, the short durability of the membrane makes water electrolysis somewhat expensive for general applications.[14] Many material studies have tried to enhance the performance of the water electrolysis process. These studies are related to the electrode, electrolyte, and separator materials used in an electrolysis cell (see section 1.3).

1.2. Applications/Properties of Hydrogen as an Alternative Energy Source

As global concerns over climate change continue to intensify, the pursuit of alternative energy sources becomes increasingly crucial.[1-15] Hydrogen has gained significant attention in this regard. Its properties make it a promising candidate for the transition to sustainable energy systems. Some of its key advantages include:

a) Grid balancing: Hydrogen can be stored and later used to help balance the grid, providing power during peak demand times and serving as a buffer to accommodate the intermittent nature of renewable energy sources. Thus, it enables higher penetration of renewable energy into the power mix.

b) Versatility: Hydrogen can be used in various applications across sectors. In the power sector, it can generate electricity, serving as an energy carrier. In transportation, it can power fuel-cell vehicles. It can serve as a feedstock for various chemical processes and industrial material processing. In the residential sector, it could provide heating and cooling.

c) Energy Density: Hydrogen has a high specific energy per unit mass (around 120-142 MJ/kg), making it a highly energy-dense fuel per unit of weight, meaning it contains a large amount of energy for its weight, making it suitable for applications where weight is a factor.

d) Decarbonisation of Hard-to-Abate Sectors: Hydrogen is essential for sectors that are difficult to electrify, such as specific high-temperature industrial processes, heavy industry, and long-haul transport, where it can replace fossil fuels.
e) Clean Combustion: When used in a fuel cell or combusted, hydrogen's only byproduct is water vapour, resulting in zero local air pollution or carbon dioxide emissions.

1.2.1. Hydrogen as an Energy Storage System for Renewable Energy

Hydrogen storage is a crucial technology for advancing hydrogen and fuel cell technologies in various applications, including stationary, portable, and transportation.[10-20] Hydrogen has the highest energy per mass of any fuel; however, its low ambient temperature density results in a low energy per unit volume, requiring the development of advanced storage methods with the potential for higher energy density.[21,28] Fig. 1.2 shows the various routes for storing hydrogen. Hydrogen can be stored physically as either a gas or a liquid. The storage of hydrogen as a gas typically requires high-pressure tanks (350–700 bar (5,000–10,000 psi) tank pressure).[28] Hydrogen storage as a liquid requires cryogenic temperatures because the boiling point of hydrogen at one atmosphere pressure is −252.8 °C. [28] Hydrogen can also be stored on the surfaces of solids (by adsorption) or within solids (by absorption).

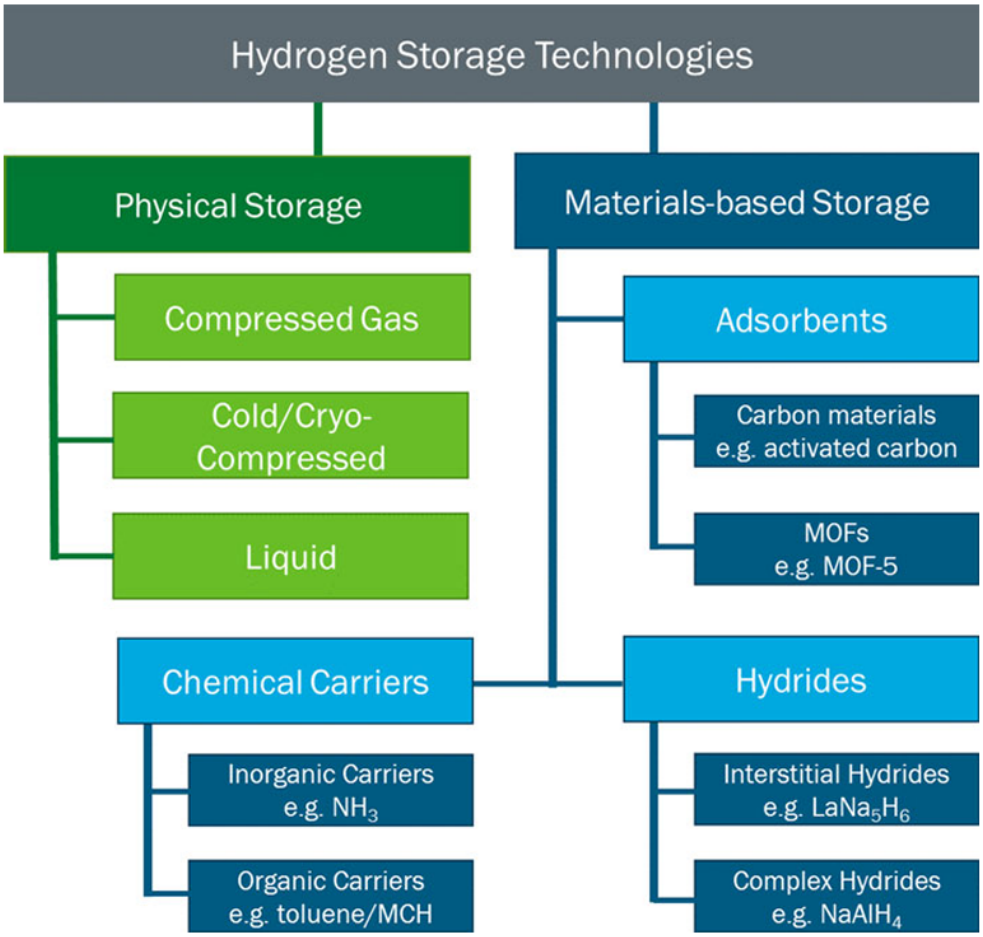

Figure 1.2. *Physical and material-based storage of hydrogen technologies* [2]

Additionally, hydrogen can be used in natural gas pipeline systems and marine and land transportation as a fuel, contributing to lower consumption of conventional fossil fuels.[29] The key feature distinguishing hydrogen energy storage systems from other forms of energy storage (e.g. batteries or compressed air energy storage systems) is their flexibility and the possibility of providing multiple services.[30] This characteristic is crucial for the grid operators to ensure system reliability and renewable energy storage system (RES) integration into multiple energy end-users within the power, heating, and transportation infrastructure.[25-30] With heating energy systems (HES), energy can be stored on a large scale, i.e. 1 GW/h to 1 TW/h, whereas batteries typically range from 10 kW/h to 10 MW/h, and compressed air storage and pumped hydro range from 10 MW/h to 10 GW/h.[23,32] Other interesting opportunities for hydrogen use include fuel cell electric vehicles or devices such as fuel cell forklifts, range extenders for battery electric vehicles, backup power supply, remote power systems, and feedstock supply to multiple industrial processes (e.g., biorefineries).[31,32] The degree to which hydrogen energy

systems can penetrate the energy storage markets will depend on various factors, including non-technological barriers, such as policy, safety, and economic issues.[32] Therefore, if adequate fuelling infrastructure is provided, hydrogen can be profitably applied in transportation and mobility and introduced for fuel cell electric vehicles.[31,32]

1.2.2. Methods of Hydrogen Production

Hydrogen is the most abundant element in the universe. Hydrogen constitutes approximately 75 wt% of the universe's total mass and 90% on an atomic basis.[26,34] However, hydrogen is rarely found in its free form on Earth. Most often, hydrogen is bound to other elements either as hydrocarbons or in water.[35,36] Many technologies exist for producing hydrogen. Many of these are primarily experimental and have not yet been found commercially helpful.[37] In Fig. 1.3, several hydrogen production technologies are listed. The production technologies are divided into columns based on the hydrogen source: fossil or renewable.

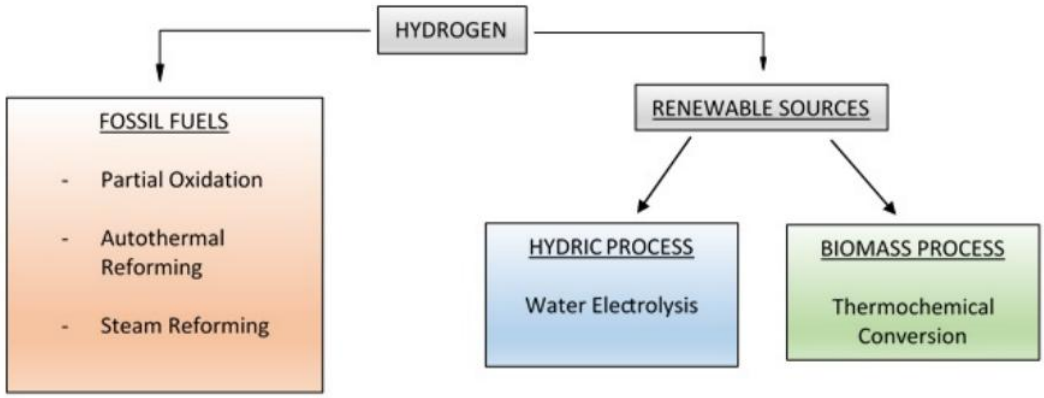

Figure 1.3. *Main hydrogen production technologies.* [17]

Since steam reforming (SR) of methane is the most widely used technology for producing hydrogen, a brief overview of the technology is appropriate.[37,38] The difference between steam reforming (SR) and partial oxidation (POX) of methane lies in the oxidant; SR uses steam as the oxidant, while POX uses oxygen. Equations (1) and (2) show the reactions for SR and POX, respectively.

$$\text{SR:}\quad CH_4 + H_2O \rightleftharpoons CO + 3H_2 \qquad [1]$$

$$\text{POX: } CH_4 + \tfrac{1}{2}O_2 \rightleftharpoons CO + 2H_2 \qquad [2]$$

To increase the hydrogen yield, the steam reforming reaction is often coupled with the water-gas shift (WGS) reaction,[38] where carbon monoxide (CO) is further reacted with additional water to produce carbon dioxide and hydrogen, as shown in Equation 3.

$$\text{WGS: } CO + H_2O \rightleftharpoons CO_2 + H_2 \qquad [3]$$

The steam methane reforming (SMR) reaction is an energy-demanding and endothermic process.[25,41] The steam reforming process of natural gas is not the way to produce clean and sustainable hydrogen because the CO content in the product stream from the WGS reaction is still too high to be fed to low-temperature PEM Fuel cells, and also because these processes convert fossil fuels to CO_2.[38,39]

Consequently, biomass is anticipated to become the most likely renewable organic substitute for petroleum. Biomass is available from a wide range of sources, including animal waste, municipal solid waste, crop residues, short-rotation woody crops, agricultural waste, sawdust, aquatic plants, short-rotation herbaceous species (e.g., switchgrass), wastepaper, corn, and many others.[36,38] Gasification is considered one of the most successful technologies for converting biomass into power, heat and chemical compounds. In gasification, biomass is heated with a gasifying agent, such as air, oxygen, or steam, producing syngas. This process occurs at high temperatures, ranging from 500 to 1400 °C, and is divided into two stages: pyrolysis and gasification. The first stage, pyrolysis, involves thermally breaking down the fuel to create volatile hydrocarbons and char (a solid residue from the devolatilization of biomass).[36,38] The second stage, gasification, involves converting these products into syngas. However, the gasification process typically suffers from low thermal efficiency, since moisture contained in the biomass must also be vaporised and produces significant amounts of “tars” (a complex mixture of higher aromatic hydrocarbons) in the product gas, even when operated at a higher temperature range (800–1000 °C).[36-39]

1.2.3. Current Challenges Confronting Hydrogen Production and Storage

Despite hydrogen`s many benefits, there are challenges to overcome to make hydrogen a significant part of the global energy mix. These include developing efficient and low-cost methods for producing hydrogen from renewable sources, addressing storage and transportation challenges, and establishing infrastructure to deliver hydrogen fuel to end-users.[32,37] Transportation and on-vehicle hydrogen storage are among the most critical factors in introducing the hydrogen economy.[36] A significant contribution to the problem is the low gas density of hydrogen.[36,37] The main obstacle to using hydrogen fuel in automobiles is its low density. Even when the fuel is stored as a liquid in a cryogenic tank or as a gas in a pressurised tank, the amount of energy that can be stored in the available space is limited, and hydrogen cars, therefore, have a limited range compared to their conventional counterparts.[38] Hence, storing hydrogen on board for a 500 km driving range is a significant challenge while meeting the performance (weight, volume, kinetics, etc.), safety, and cost requirements without compromising passenger or cargo space.[38,39] The fuel storage systems in today's gasoline vehicles have an energy density of about 6 kWh/L.[39] Hydrogen, on the other hand, has a higher energy density by weight but a lower energy density by volume than gasoline. This means that while hydrogen holds more energy per kilogram, it requires significantly more space to store the same amount of energy as gasoline. For example:

- Gasoline: ~6 kWh/L (volumetric energy density)
- Liquid Hydrogen: ~2.36 kWh/L (volumetric energy density)
- Compressed Hydrogen (700 bar): ~1.3 kWh/L (volumetric energy density)

This difference presents a challenge for hydrogen storage in vehicles, as it requires high-pressure tanks or cryogenic storage to be viable.[39] However, hydrogen's gravimetric energy density (energy per unit mass) is much higher, making it attractive for applications where weight is critical, such as aerospace. The second major problem is the high cost of making reliable fuel cells. A combination of the two problems is hindering the development of hydrogen automobiles.[40] Also, existing hydrogen dispensers are inadequate to support commercial fueling. Cost, reliability, and safety must be significantly improved for commercial fueling.[38-40]

1.3. Introduction to Water Electrolysis

Water electrolysis is an electrochemical process in which electrical energy is used to drive a non-spontaneous chemical reaction: the decomposition of water into its elemental constituents, hydrogen and oxygen. This reaction is represented by equation 4. The process is conducted in an electrolyser, which facilitates the reaction by applying an external electric potential across two electrodes immersed in water.[35] Electrolysers range from compact, appliance-sized units suitable for decentralised hydrogen generation to industrial-scale systems integrated with renewable energy sources for centralised production. When powered by electricity derived from renewable sources such as solar or wind, the electrolysis process yields hydrogen with minimal carbon emissions. This form of hydrogen is commonly referred to as green hydrogen, reflecting its low environmental impact.[35,36]

The simplest form of water electrolyser is a cell containing water and two electrically conducting electrodes that supply the electricity. When a sufficient potential is applied between the electrodes for current to flow, the water decomposes, and hydrogen gas is liberated at the negative electrode (cathode) and oxygen at the positive electrode (anode).[35] Gases are produced so long as the electricity is supplied (Fig. 1.4).[36] Electrochemical cells are broadly classified into galvanic cells and electrolytic cells.[35,36] In galvanic cells, spontaneous reactions occur. Examples of galvanic cells include batteries and fuel cells, in which chemical reactions are paired with appropriate half-cell reactions, resulting in a negative free-energy change for the overall process. In contrast, electrolysis cells require an external electrical energy input to drive non-spontaneous reactions at the electrodes. The charge-transfer and ionic-flux rates directly depend on the applied voltage.[35,36]

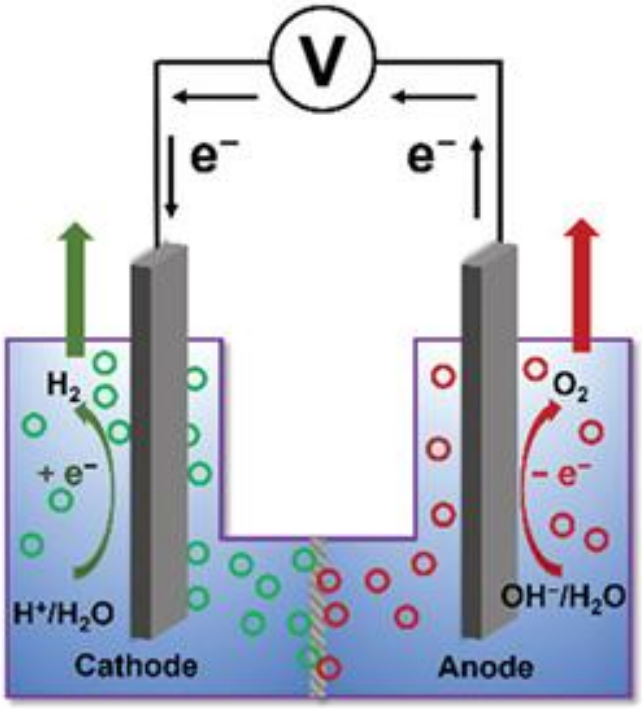

Figure 1.4. *Schematic of a typical water electrolysis cell.* [35]

Adding an electrolyte (Fig. 1.4) increases water's conductivity, facilitating the continuous flow of electricity. Different ions serve as charge carriers, including H^+, OH^-, and O^{2-}, depending on the pH and the type of cell.[37] The water electrolysis reactions at the electrodes with varying charge carriers may differ, but the overall reaction is always the same. At high pH, the cathode reduces water, generating hydrogen (H_2) and hydroxide ions (OH^-) via the hydrogen evolution reaction (HER).[37,38] The OH^- ions migrate to the anode through the electrolyte, where they are oxidised by the OER (oxygen evolution reaction). These two reactions (HER and OER) complete the water-splitting reaction.[39] The two electrochemical reactions occur simultaneously and generally in the same cell.

1.3.1. Fundamentals of Electrochemical Water Splitting

The electrolytic cell was first proposed in 1789 and comprises three parts: the cathode, the anode, and the electrolyte.[39] Water electrolysis is generally conducted at temperatures lower than 100 ℃ but is often limited by the thermal stability of membranes.[39]

$$H_2O\ (l) \rightarrow H_2(g) + \tfrac{1}{2}O_2\ (g) \qquad [4]$$

The two half-reactions are the hydrogen evolution reaction (HER) at the cathode and the oxygen evolution reaction (OER) occurring at the anode in a water electrolyser cell. Both reactions are pH-dependent (Fig. 1.4), of which the equilibrium half-cell potentials (E^0) at 1 atm and 298.15 K versus standard hydrogen electrode (SHE) are shown in the equation as follows:

in acidic electrolytes (pH = 0):

$$\text{Cathode: } 4H^+ + 4e^- \rightarrow 2H_2, \quad E^0 = 0.000\ \text{V} \qquad [5]$$

$$\text{Anode: } 2H_2O \rightarrow O_2 + 4H^+ + 4e^- \quad E^0 = 1.229\ \text{V} \qquad [6]$$

in alkaline electrolytes (pH = 14),

$$\text{Cathode: } 4H_2O + 4e^- \rightarrow 2H_2 + 4OH^- \qquad E^0 = -0.828\ \text{V} \qquad [7]$$

$$\text{Anode: } 4OH^- \rightarrow O_2 + 2H_2O + 4e^- \qquad E^0 = 0.401\ \text{V} \qquad [8]$$

Electricity passes through the electrolyser, thereby splitting water molecules into their two components, hydrogen and oxygen gas.[40] The amount of gas produced per unit of time is directly related to the current that passes through the electrochemical cell. Oxygen accumulates at the positive pole (anode), rises, and escapes into the atmosphere. Hydrogen accumulates at the minus pole (cathode), where it can be captured and stored.[35-46] The stored energy from the water electrolysis process, which is now in the hydrogen molecules, can be rereleased by the reverse reaction of hydrogen with oxygen.

Electrolysers can range from small, appliance-size equipment well-suited for small-scale distributed hydrogen production to large-scale, central production facilities tied directly to renewable or other non-greenhouse-gas-emitting forms of electricity production.[36-43] Water splitting occurs at a considerable cell potential (1.8–2.0 V) for commercial electrolysers, about 0.55 to 0.77 V higher than the theoretical value (1.23 V).[40,43] This excess potential is required

to overcome the energy barrier of the reaction system and is referred to as overpotential. This overpotential may be due to contact and solution resistance at the electrode-electrolyte interface, the distance between them, and the activation barriers associated with the kinetic steps at both the cathode and anode.[40,43] Thus, to practically carry out water splitting, a potential higher than the thermodynamic potential is required.[36-45] A decrease in overpotential can be achieved by utilising electrocatalysts, and other resistances can be minimised by optimising the electrolyser design, thus making electrochemical water splitting greener and more affordable. Different water electrolysis technologies operate differently, primarily due to the varying electrolyte materials used and the ionic species they facilitate.

1.3.2. Alkaline Water Electrolysis

Alkaline water electrolysis (AWE) splits water into oxygen and hydrogen using alkaline electrolytes such as sodium hydroxide (NaOH) and potassium hydroxide (KOH). The major components of a primary alkaline water electrolysis cell are diaphragms/separators, current collectors (gas diffusion layers), separator plates (bipolar plates), and end plates. Asbestos-, zirconium-, and nickel-coated perforated stainless-steel diaphragms are used as separators in alkaline water electrolysis.[46,47] The nickel mesh/foam is used as a gas diffusion layer, and stainless steel/nickel-coated stainless steel separator plates are used as bipolar and end plates. The entire process can be divided into two half-reactions: the anodic and cathodic reactions (Fig. 1.5). The anode in the alkaline water electrolysis process is of significant importance in determining the overall effectiveness and functioning of the system.

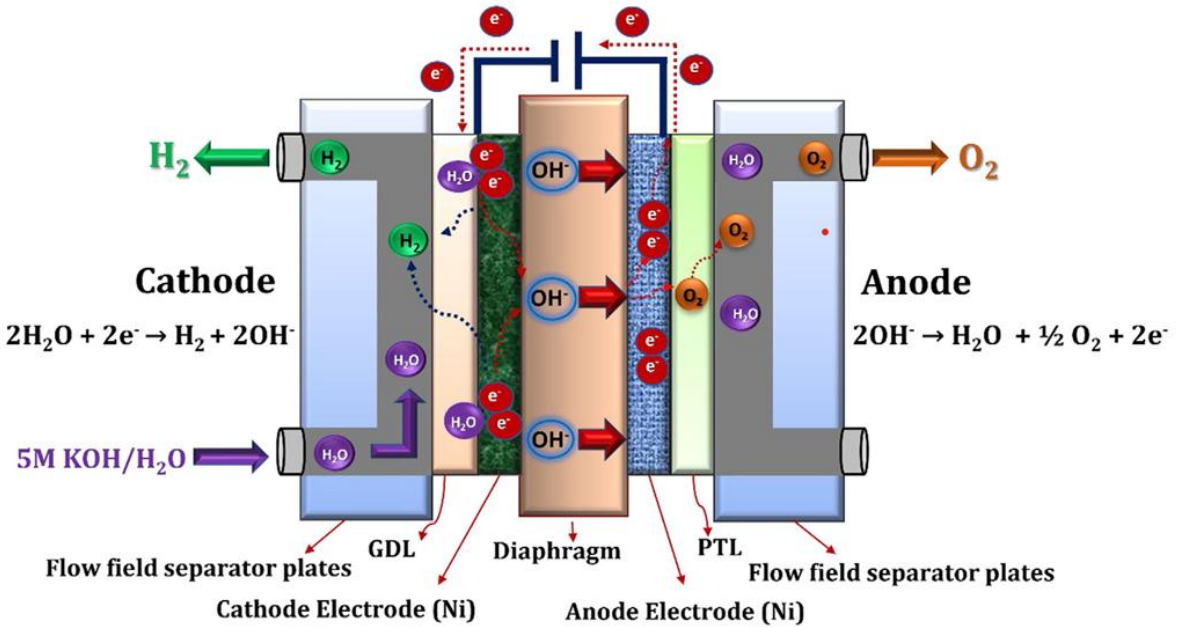

Figure. 1.5. *Operating principle of an alkaline water electrolysis cell.*[49]

In contrast to the relatively uncomplicated hydrogen evolution reaction at the cathode, the oxygen evolution reaction (OER) at the anode is somewhat complicated.[47,49] It comprises several successive stages and intermediate products. The primary OER pathway in alkaline media is the four-electron transfer process, represented by equations 7 & 8. Alkaline electrolysers have been commercially used in industrial applications since the 1920s, making them the most mature electrolyser technology available today. Fig. 1.5 illustrates the working principle of an alkaline water electrolysis cell. As direct current passes through the cell, water is decomposed, generating hydrogen at the cathode and oxygen at the anode. [49,50] The two gases are kept separate by the separator.[50] The voltage drop across the cell is a measure of its energy efficiency, i.e., the percentage of energy in the electricity that is converted to hydrogen.

1.3.3. Anion Exchange Membrane Water Electrolysis

Anion exchange membrane water electrolysis (AEMWE) technology is an emerging technology in its early stages of development, as illustrated in Fig. 1.6. The earliest known research article specifically focused on anion exchange membrane water electrolysis (AEMWE) was published around the early 2000s, [46,49] and in 2012 by Leng *et al.* explored the feasibility of AEMs in water electrolysis and compared their performance to that of proton exchange membranes (PEMs), helping to establish AEMWE as a distinct research area.[47] This technology was developed by merging the merits of both conventional alkaline and PEM electrolysis technologies. In AEM electrolysis, low-cost catalytic materials were adopted from alkaline electrolysis, and the idea of a solid polymer electrolyte architecture was adapted from PEM electrolysis technology.[47,50] Thus, it is expected to produce pressured hydrogen using cost-effective, earth-abundant catalysts and safer alkaline operating conditions.[49] Moreover, AEMs demonstrate excellent gas tightness, preventing gas crossover, and achieve hydrogen purity levels of up to 99.99%, thereby playing a pivotal role in determining the electrolyser's performance.[49] A separator (membrane) is used to space the anode and cathode within a water electrolysis cell. The low-temperature AEM technology consists of two half-cells, with HER at the cathode producing H_2 and OH^- from the reduction of water molecules. Then, at the anode, we observe OER, in which O_2 and H_2O are generated from the oxidation of OH– ions, as illustrated in Fig. 1.6.

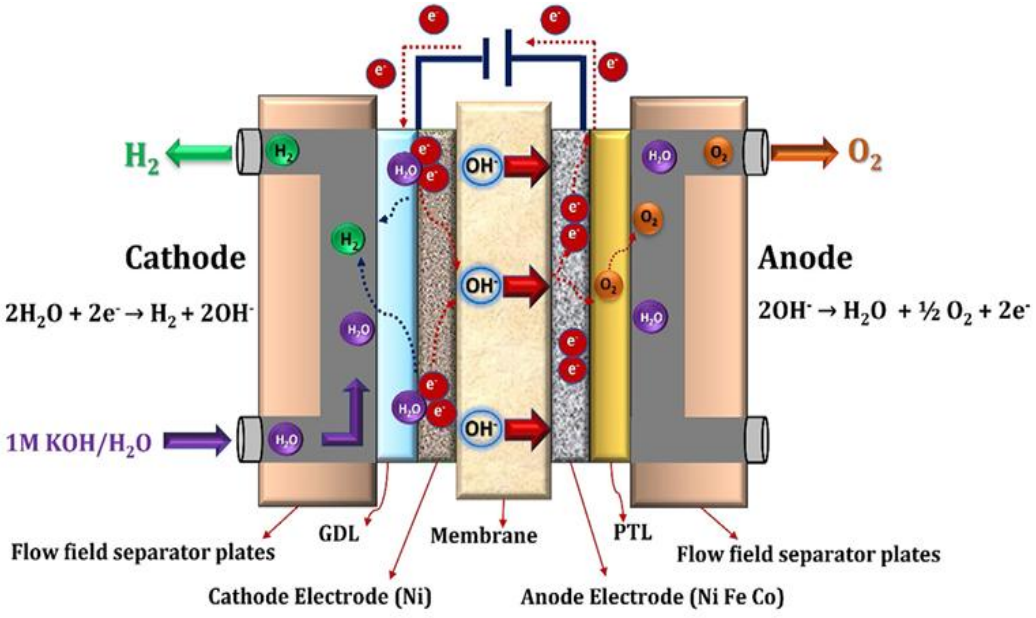

***Figure 1.6**. Working principle of AEM water electrolysis using a membrane and GDL*[49]

AEM water electrolysis offers several advantages, including the cost-effective use of transition-metal catalysts rather than noble-metal catalysts. Additionally, distilled water/low-concentration alkaline solution (1 M KOH) can be used as an electrolyte rather than a high-concentration KOH solution. Despite the significant advantages, anion exchange membrane water electrolysis (AEMWE) still requires further investigation and improvement towards MEA stability and cell efficiency, which are essential for commercial applications.[51,52] Similarly, this technology is still unable to produce hydrogen at high pressures due to the limited mobility of hydroxide ions in the liquid phase.[52] This inability to produce high-pressure hydrogen for storage necessitates the addition of an external compressor, which increases the system's cost.[48,53] Another major challenge of the traditional alkaline water electrolysis is the limited current density (0.1–0.5 A/cm^2) due to moderate OH^- mobility and the use of a corrosive (KOH) electrolyte. Moreover, in water electrolysis, the primary limiting factor for the overall water splitting pathways is the sluggishness of the OER process, and significant effort is needed to overcome this problem. [53] In addition to the slow kinetics for the OER or HER, there are increased overpotentials and stability concerns. Compared to proton exchange membranes (PEM) (see 1.3.5), AEM membranes have lower ionic conductivity, which can limit performance [53]

1.3.4. Solid Oxide Electrolysers

The fundamental mechanisms involved in solid oxide electrolyser operation are shown in Fig. 1.7, where steam is fed to the porous cathode.[54] When required, an electrical potential is applied to the SOE, and water molecules diffuse to the reaction sites. They are dissociated to form hydrogen gas and oxygen ions at the cathode-electrode interface.[54] The hydrogen gas produced diffuses through the cathode and is collected at the outlet. The oxygen ions are transported through the ceramic electrolyte to the anode.[55] On the anode side, the oxygen ions are oxidised to oxygen gas, and the produced oxygen is transported through the pores of the anode to the outlet. The net reaction of SOE can be written as:

$$H_2O \rightarrow H_2 + \tfrac{1}{2}O_2 \qquad [9]$$

The total energy demand (ΔH) for SOEC hydrogen production can be expressed as

$$\Delta H = \Delta G = T\Delta S \qquad [10]$$

ΔG is the Gibbs free energy change (electrical energy demand), and TΔS is the thermal energy demand (J/mol H_2). An increase in operating temperature decreases electrical energy demand and increases thermal energy.[55,56] In Fig.1.7, the oxygen ions pass through the solid ceramic electrolyte and react at the anode to form oxygen gas and generate electrons. Solid oxide electrolysers operate at temperatures high enough (approximately 500-900 °C) for the solid oxide electrolyte to be sufficiently conductive to oxygen ions.[54-58] The solid oxide electrolysers can effectively utilise heat available at these elevated temperatures (from various sources, including nuclear energy) to reduce the amount of electrical energy required to produce hydrogen from water. [58]

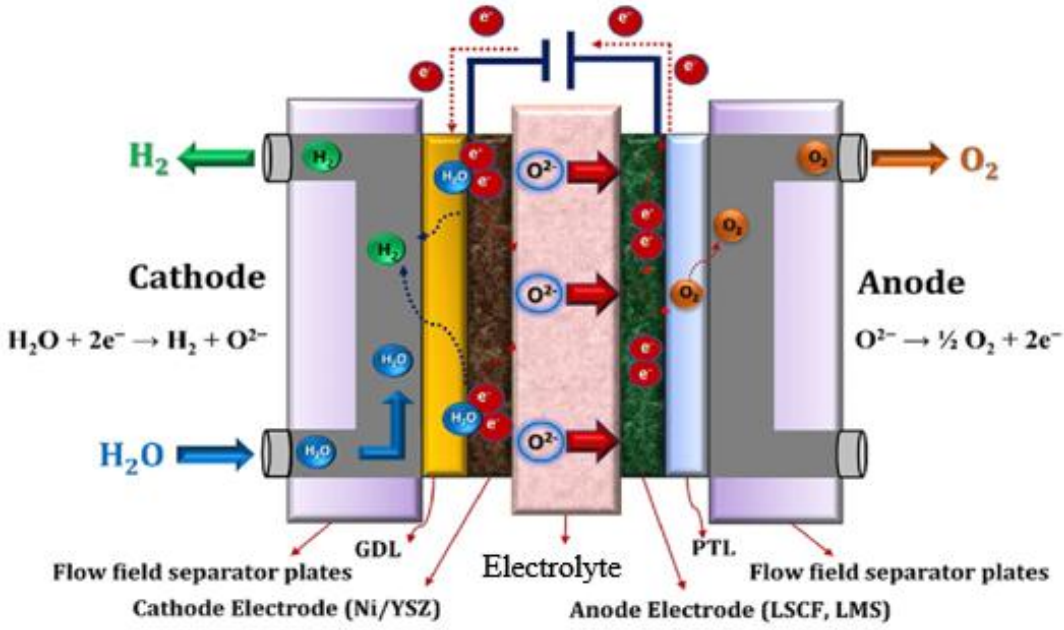

Figure 1.7. *Working principle of a schematic solid oxide water electrolysis cell* [49]

Solid oxide water electrolysis technology offers the advantage of being able to operate with non-noble-metal electrocatalysts. However, this comes at the cost of high operational and maintenance costs.[55,58] Technical issues, such as leakage of gas-tight components and the requirement of rigid materials, hinder their application [58] Other challenges associated with this technology include long-term stability.[56-58]

1.3.5. Proton Exchange Membrane Water Electrolysis

Polymer electrolyte membrane (PEM) water electrolysis technology is frequently presented in the literature as an exciting alternative to the more conventional alkaline water electrolysis.[58] Regarding sustainability and environmental impact, polymer electrolytic membranes, or proton exchange membrane (PEM) water electrolysis systems, offer several advantages over traditional alkaline technology for converting renewable energy to highly pure hydrogen.[58,59] PEM water electrolysis offers several advantages, including a compact design, high current density (above 2 A/cm^2), high efficiency, fast response, a small footprint, operation at lower temperatures (20–80 °C), and the ability to produce ultrapure hydrogen.[59-64] The PEM water electrolysis cell consists primarily of a proton exchange membrane in which the anode and cathode are bonded to the membrane (Fig. 1.8).

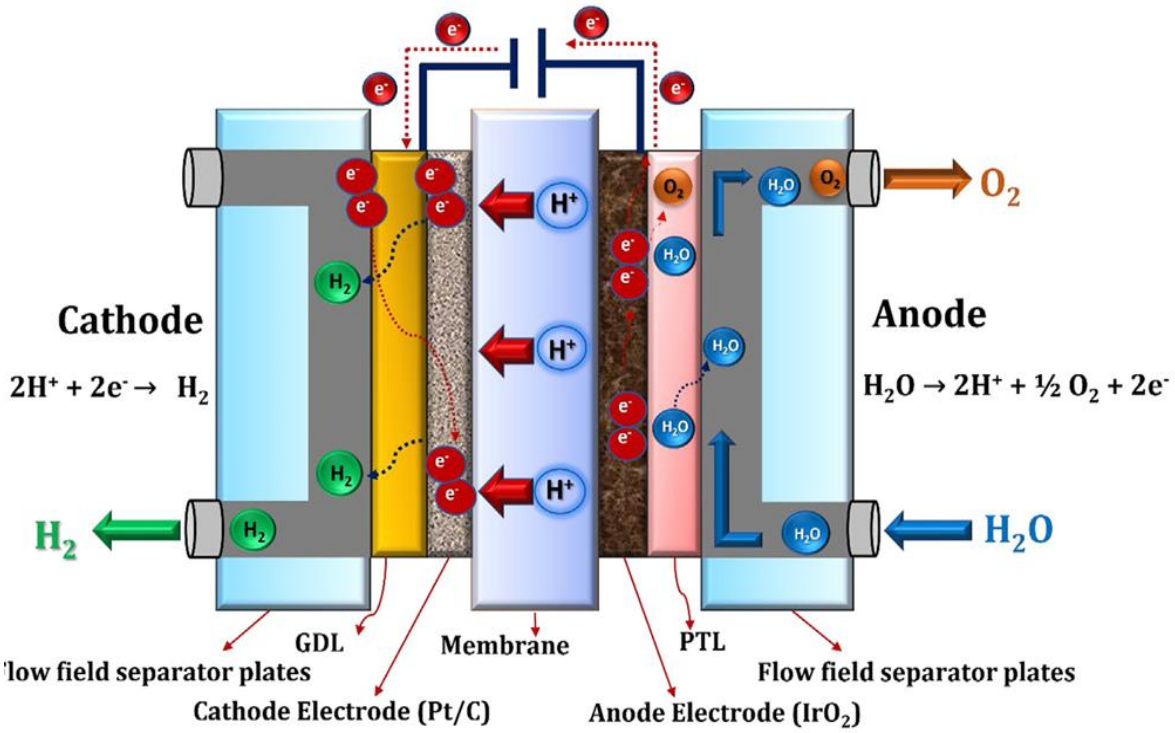

Figure 1.8. *PEM electrolyser cell and the principles of operation* [49]

In a PEMWE cell, the acidic membranes are used as solid electrolytes due to the limited self-ionisation of pure water. A single PEMWE cell comprises a catalyst-coated membrane (CCM), gas diffusion layers (GDLs) and bipolar plates.[59-64] The two half-cells are separated by a solid, acidic Nafion or other PEM membrane, which separates the product gases, transports protons, and supports the cathode and anode catalyst layers.[60] The CCM is placed between two porous

GDLs (usually Ti felt at the anode and carbon paper or cloth at the cathode), which provide mass transport pathways for water and product gases, and conduct electrons and heat between the bipolar plates and the catalyst layers.[61,62] The bipolar plates often serve as flow channels to ensure a uniform flow of water over the GDLs and facilitate the easy removal of gases produced. [59-64] During the operation, liquid water is introduced to the anode and decomposed into molecular oxygen, protons, and electrons.[65-67] Solvated protons formed at the anode can migrate through the membrane to the cathode, where they are reduced to molecular hydrogen. Water is electrochemically split into hydrogen and oxygen at their respective electrodes, hydrogen at the cathode and oxygen at the anode.[64-69]

Liquid water is sometimes released at the cathode due to electro-osmotic drag (movement of water molecules through an ion-conducting membrane, driven by the migration of ions in response to an electric field). As ions (such as H^+ or OH^-) travel across the membrane, they "drag" water molecules along with them through strong electrostatic interactions.[62] Oxygen and hydrogen are generated in a stoichiometric ratio, two volumes of hydrogen for every one volume of oxygen, at a rate proportional to the applied cell current.[62,63] Some advantages of PEM include the electrolyte being immobilised and unable to be leached from the cell.[63-64] The electrolyte membrane can be thin, allowing high conductivity without the risk of gas crossover.[62,64] However, some of this technology's drawbacks include the high cost of the electrolyte and component degradation. Table 1.1 shows these electrolyser technologies and their performance.

Table 1.1. Comparison of different electrolyser technologies' operation temperature, stack voltage efficiency, merits, and demerits

Types	Operating temperature /°C	Stack voltage efficiency (%)	Merits	Demerits
Proton exchange membrane (PEM)	80 − 100 (low temp.) or 200 (high temp.)	60 – 70	Fast start-up, widely used in transport and stationary applications	Expensive catalyst
Alkaline water electrolysis (AWE)	70 − 80	50 − 80	Good current response	Low hydrogen production rate and gas crossover
Solid oxide electrolysis	800 –1000	60 – 80	Solid electrolyte, reusable heat, and lower cost	issues with metal corrosion
Anion exchange water electrolysis	30 – 60	< 80	Excellent gas tightness, prevents gas crossover, leading to hydrogen purity levels of up to 99%	Membranes degrade over time, especially in highly alkaline environments, reducing long-term durability.
Molten carbonate fuel cell (MCFC) electrolysis	> 650	60 – 80	Good conductivity and high current density	Only used in large-scale stationary applications due to slow start-up

1.3.6. Components of a Proton Exchange Membrane Electrolysis Cell

The proton exchange membrane water electrolysis cell consists of several components, including the proton exchange membrane. Typical proton exchange membranes are Nafion®, Fumapem®, Flemion®, Aquivion®, and Aciplex®, respectively. However, the most widely used membranes are Nafion® 115, 117, and 212.[58,59] The Nafion® membrane offers several advantages, such as high proton conductivity, current density, mechanical strength, and chemical stability. The state-of-the-art anode and cathode electrode materials are noble-metal-based electrocatalysts: IrO2 for OER and Pt/C for HER.[63,64] Fig. 1.9 highlights the exploded view of a typical PEM cell component and how these components are assembled.

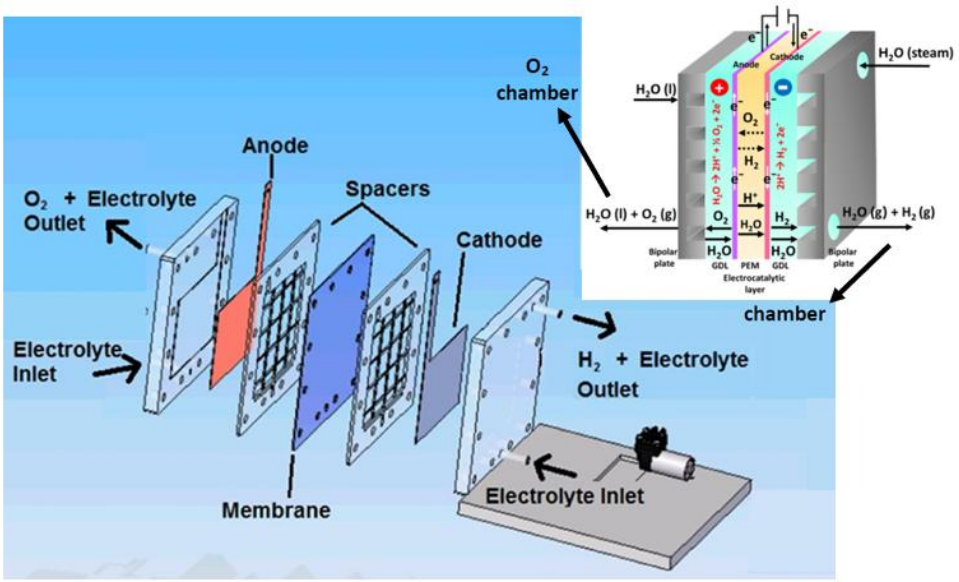

Figure 1.9. *Schematic of the exploded view of a typical PEM cell* [63]

These noble metals are more expensive, and iridium is scarcer than platinum. For example, a 10 MW PEM water electrolyser operating at 1 A/cm^2 requires approximately 1 kg of Iridium with an assumed catalyst loading of 1.5–2.5 mg/cm^2. Porous titanium/titanium mesh, Ti felt, and carbon cloth are often employed as anode and cathode gas diffusion layers. Different flow field-designed bipolar plates made of titanium material are used as separators and end plates, respectively.[62,64] The straight parallel flow field-designed separator plates have shown better performance among different flow field designs, especially in the PEM water electrolyser.[63,64] However, these separator plates are expensive and are responsible for 50% of the overall cell cost.[58,62,64] Consequently, the cost of cell components, i.e., electrode materials and separator

plates, remains a serious challenge for PEM technology. The components of the electrochemical cell are explained and illustrated in Fig. 1.9, which shows an assembled PEM cell in the top-right corner. In contrast, the rest of the figure shows an expanded view of the cell, containing seven major parts that connect in sequence: the cathode's end plate, placed on a PTFE insulating plate, which connects to the flow field and a hydrogen spacer. A membrane (usually Nafion) is placed between the hydrogen-spacer and the oxygen-spacer. Thereafter, the anode is connected to the anode-endplate, which is placed on the PTFE insulating plate, the gas diffusion layer, and the oxygen spacer. Finally, all the parts are bolted together with stainless steel bolts.[54-63] Despite the distinct performance of commercialised proton exchange membrane water technology, the price of green hydrogen remains high due to the high cost of cell components. It is not yet competitive with that generated by SMR. The PEM electrolysis, although promising for future energy integration, remains costly when coupled with renewable energy sources.[63]

1.4. Introduction to Decoupled Water Electrolysis

Decoupled electrolysis is an innovative and promising field introduced by Symes and Cronin in 2013.[64] Since then, researchers worldwide have explored its potential using soluble and solid-state mediators.[65-74] This approach offers remarkable flexibility and unique opportunities for hydrogen production that conventional electrolysers cannot achieve.[65-70] The main principle of decoupled water electrolysis is straightforward yet profound: by employing a redox mediator at sufficiently high concentration, the anodic and cathodic products of an electrochemical reaction can be generated independently of one another at separate rates and times, and even in separate electrochemical cells.[67,70] This groundbreaking concept is exemplified by comparing a traditional water electrolysis system with a decoupled version (Fig. 1.10a). In the latter, water oxidation at the anode is linked to a redox mediator's reversible reduction and protonation rather than the direct proton reduction to form hydrogen (Fig.1.10b). Subsequently, the mediator's re-oxidation releases protons and electrons that combine at the cathode to produce hydrogen (Fig.1.10c). As long as the mediator remains stable in its reduced form, this approach enables the non-simultaneous production of hydrogen and oxygen gases at different times and rates in separate cell systems.

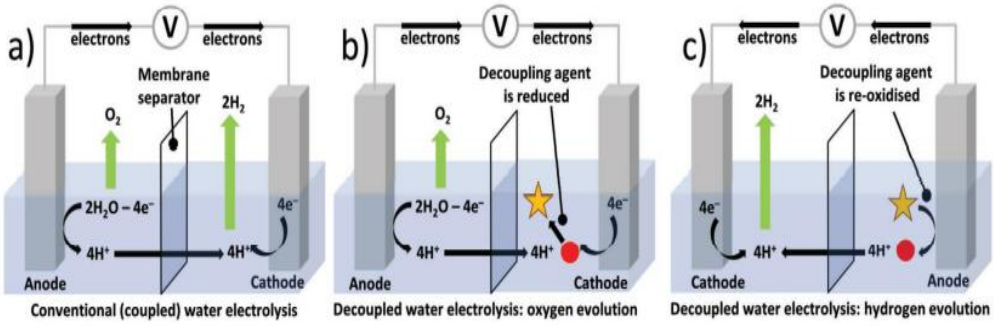

Figure 1.10. *Comparison of conventional water electrolysis (a) and decoupled electrolysis (b, c)* [71]

Existing electrolysers face two significant challenges that hinder their use in green hydrogen production powered by renewable energy.[72] Firstly, they cannot efficiently handle intermittent power inputs, a common characteristic of renewable sources like solar power, which fluctuate with weather and time of day. For instance, a conventional electrolyser directly connected to a solar panel would frequently stop and start, leading to the faster degradation of costly components and the production of hazardous hydrogen-oxygen mixtures.[72/73] To operate safely,

these systems require extensive power management systems, without which they pose significant safety risks and have limited compatibility with renewable energy sources.[73,74]

Secondly, conventional electrolysers incur high operational and maintenance costs. They rely on expensive membranes to separate hydrogen and oxygen, but these degrade quickly during use, necessitating frequent replacements.[65-73] This not only increases costs but also complicates the long-term operation of such systems. A decoupled electrolysis system utilising a redox mediator as a decoupling agent has the potential to address both key challenges, in turn potentially making hydrogen production more sustainable, cost-effective, and hazard-free. In particular, there is the prospect that decoupled systems could be more compatible with intermittent renewable energy sources, paving the way for broader adoption of green hydrogen production. Decoupled systems also show promise for more ready compliance with regulatory safety standards for mixed gas content,[72,74] and significantly reduced membrane degradation compared to traditional water electrolysis systems. As a result, they could require less maintenance and downtime, offering economic and operational advantages.

Symes and Cronin established key criteria for selecting redox mediators for decoupled water electrolysis. Building on their framework, the following properties are suggested for identifying suitable solution-phase mediators to serve as decoupling agents for water splitting:

(i) *Stability*: The redox mediator must be chemically stable in an aqueous electrolyte under the operating conditions of the electrolytic cell.

(ii) *Reversibility*: The redox mediator should have a reversible redox reaction that exchanges electrons and ions with the auxiliary electrode and/or the electrolyte.

(iii) *Cyclability:* The redox mediator should withstand many redox cycles without performance deterioration during the system's lifetime.

(iv) *pH buffering:* The mediator's redox reactions should not affect the pH of the electrolyte to avoid substantial pH gradients during operation.

(v) *Redox potential:* should be within the water's electrochemical window on the electrodes used, i.e., above the HER onset potential and below the OER onset potential for the cathode and anode, respectively. Otherwise, oxygen and hydrogen may evolve during the redox reactions, leading to H_2/O_2 mixing.

(vi) *Low overpotential:* The redox mediator's oxidation and reduction overpotentials should be low to minimise the applied voltage and the resulting power losses incurred by the decoupling process.

(vii) *Compatibility:* To prevent their degradation, the redox mediator should be compatible with the other cell components (electrodes, membrane, etc.). Specifically, it should not release any substance that may poison the primary electrodes or foul the membrane.

(viii) *Capacity:* The redox mediator should have a high charge capacity per unit volume and/or weight.

(ix) *Faradaic efficiency:* The Faradaic efficiency of the redox mediator's oxidation and reduction reactions should be 100%, i.e., no reactions other than oxidation/reduction of the mediator should take place, and no side-products should be produced.

(x) *Cost and availability:* For industrial systems, the redox mediator should comprise earth-abundant elements, be non-toxic and environmentally benign, and be cheap.

Soluble redox mediators require high molecular charge capacity and water solubility under the electrolytic cell's operating conditions.

Although decoupled water electrolysis offers exciting advantages like safer operation and compatibility with intermittent renewable energy, it also comes with several technical and economic challenges:

(i) *Complexity of Redox Mediators:* the system relies on redox mediators (e.g., phosphomolybdic acid, silicotungstic acid, nickel hydroxide) to separate the hydrogen and oxygen evolution reactions. These mediators must be stable, highly reversible, and non-toxic. These requirements are demanding to meet simultaneously.

(ii) *Efficiency Losses:* Though decoupled water electrolysis can reduce gas crossover, it often introduces additional energy losses due to multi-step reactions and mediator regeneration. This can reduce the efficiency of the electrochemical system compared to conventional electrolysis.

(iii) *Scaling up is still a significant hurdle.* The architecture, often involving separate cells or stages, adds complexity and cost, making it challenging to commercialise at scale.

(iv) Purity and Contamination Risks: Mediators can be sensitive to impurities in the water and (when reduced) to oxygen in the air, which may lead to reduced performance. This

could limit the use of low-purity water and could increase some aspects of the maintenance burden.

1.4.1. Solid-State Redox-Mediated Decoupled Water Electrolysis.

A water electrolysis system employing a solid redox mediator (SRM) offers the potential to decouple hydrogen and oxygen production, making it an ideal solution for hydrogen generation.[65-74] As illustrated in Fig. 1. 11a, transferring electrons and ions between two electrodes is essential for sustaining hydrogen and oxygen production in an electrolytic cell. By utilising a buffer electrode capable of reversibly storing and releasing electrons and ions, the hydrogen evolution reaction (HER) and oxygen evolution reaction (OER) can be spatially and temporally separated. [76]

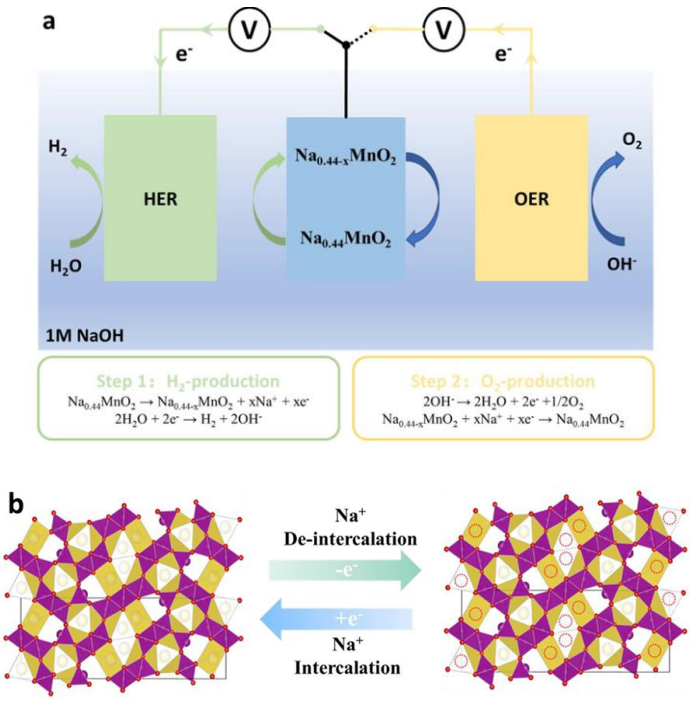

Figure 1.11. *Schematic illustration of (a) decoupled alkaline water electrolysis and (b) solid redox mediator (SRM) ($Na_{0.44}MnO_2$) reaction mechanism.* [74]

During the charging process (i.e., the electrochemical oxidation), the electrodes release electrons and de-intercalate positive ions (such as Li^+, Na^+, and H^+) to maintain electrical neutrality.[71,76] When discharging, the electrodes store electrons and intercalate positive ions. Over the past half-century, these materials have been primarily used in rechargeable batteries,

such as lithium-ion and Ni-MH batteries.[71,76] Using such a battery electrode as a redox mediator is expected to decouple the H_2 and O_2 produced during water electrolysis.[77]

The electrochemical principles at work with solid-state decoupling agents include intercalation and redox chemistry as follows:

Mediator oxidation: The mediator electrode undergoes oxidation, releasing electrons to the external circuit. Simultaneously, positive ions (Li^+, Na^+, H^+) are de-intercalated (released) from the electrode into the electrolyte to maintain charge balance [74]

Mediator reduction: The mediator electrode is reduced by accepting electrons and intercalating positive ions from the electrolyte back into its structure.

This reversible ion-electron exchange is the foundation of rechargeable batteries, such as Li-ion and Ni-MH, in which materials like $LiCoO_2$, graphite, or NiOOH serve as active electrodes.[74] By introducing a redox mediator (a material that can reversibly store and release electrons and ions) in solid-state decoupled electrolysis, the HER and OER can be separated: as the mediator is oxidised, it releases electrons and de-intercalates ions. These electrons drive hydrogen evolution at a separate cathode. When the mediator is reduced, it accepts electrons and re-intercalates ions. These electrons come from the oxygen evolution reaction at a separate anode. This system offers improved safety by avoiding H_2/O_2 mixing and allowing flexible operation under intermittent renewable energy input.[76,77]

1.4.2. Liquid-Phase Redox-Mediated Decoupled Water Electrolysis

Liquid-phase mediators are species such as molecules, ions, or compounds that undergo reversible oxidation and reduction during electrochemical processes in solution.[74,78] Fig. 1.12 shows how these mediators (solid and liquid) function as electron carriers, enabling the decoupling of a single electrochemical reaction into a series of electrochemical or chemical steps.[73,74] Introducing a redox mediator provides various opportunities to construct novel cell configurations for effective electrochemical hydrogen production. Then, redox mediators must possess high reversibility, fast kinetics, and negligible side reactions.[75,81] Based on these requirements, some redox mediators used as active molecules in redox flow systems, such as quinones, multivalent metal ions, and heteropolyacids, show impressive prospects for enhancing water electrolysis [75]

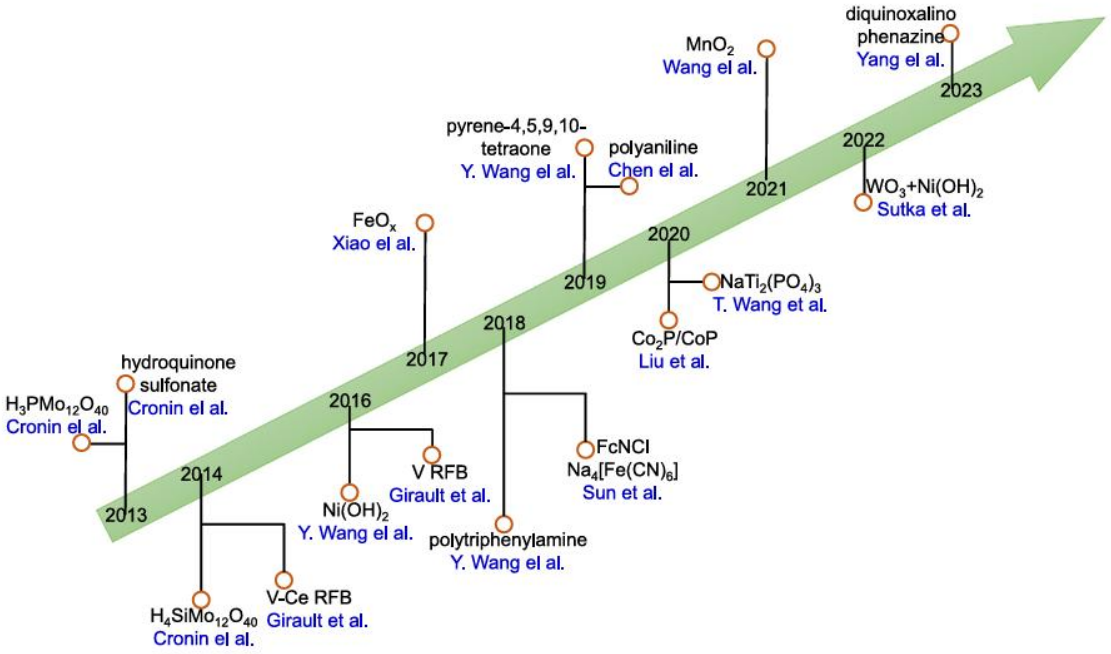

Figure 1.12. *Shows various redox mediators for decoupled water splitting since 2013 (FcNCl and RFB represent trimethylammonium chloride (ferrocenyl methyl) and redox flow battery, respectively)* [79]

Numerous reviews have highlighted the role of redox mediators in advancing electrocatalysis and electrochemical synthesis. Zhang *et al.* demonstrated that these mediators have recently enabled the decoupling of the hydrogen evolution reaction (HER) and oxygen evolution reaction (OER) across both temporal and spatial domains. By introducing redox mediators, Zhang addressed key limitations of conventional water electrolysis and underscored their potential to enhance the possibility of practical applications [75]

Shao *et al.* offered a comprehensive overview of recent progress in electrocatalysis and electrosynthesis, focusing on the underlying principles and structural design of systems incorporating redox mediators.[76] He demonstrated that the addition of redox mediators, which serve as the intermediate electron carriers or reservoirs without changing the final products, provides a unique approach to accelerate the electrochemical performance of these energy conversion systems. Similarly, Ifkovits *et al.* emphasised the performance-enhancing capabilities of redox mediators, noting their ability to reduce the need for instantaneous energy input. This advantage aligns well with the integration of renewable energy for safe and cost-effective water splitting [77]

Robert *et al.* further explored the application of redox mediators in electrochemical synthesis, demonstrating improvements in both safety and affordability. Their findings also revealed that specific reactions previously inaccessible by direct synthesis could be achieved using mediator-assisted pathways. The same study shows that using a redox mediator significantly improves safety and reduces costs. Table 1.2 provides a detailed summary of various redox mediators employed in decoupled water electrolysis systems.

Table 1.2. Properties of some liquid phase mediators used in a decoupled water electrolysis system for hydrogen production (Full names of the mediators are contained in the main text).

Mediators	E° (V vs RHE)	pH	Proton balance	Cycles/capacity (Stability)	Ref
AQDS	0.21	0	Yes	100 (94.25%)	64
HQMS	0.69	0.7	Yes	20 (80%)	64
TMQ	0.61	0	Yes	9 (>98.5%)	72
STA	-0.2,0.04	0.5	Yes	9 (100%)	68
PMA	0.57,0.68	0.3	Yes	4 (98%)	64
LiPWO	-0.38, 0.1, 0.15, -0.27	0	Yes	100 (97.4%)	87
$V^{2+/3+}$	-0.26	0	No	120 hrs @110 mA/cm^2	88
$[Fe(CN)_6]^{3/4-}$	1.19-1.37	7-14	No	–	75

Cronin *et al. 2013* employed the soluble electron-coupled proton buffer (ECPB), phosphomolybdic acid ($H_3PMo_{12}O_{40}$), as a redox mediator to decouple the hydrogen evolution reaction (HER) from the oxygen evolution reaction (OER) under acidic conditions.[64] The system was configured with a two-compartment setup, similar to conventional water electrolysers, but featured an additional switched power supply design Fig. 1.13a.

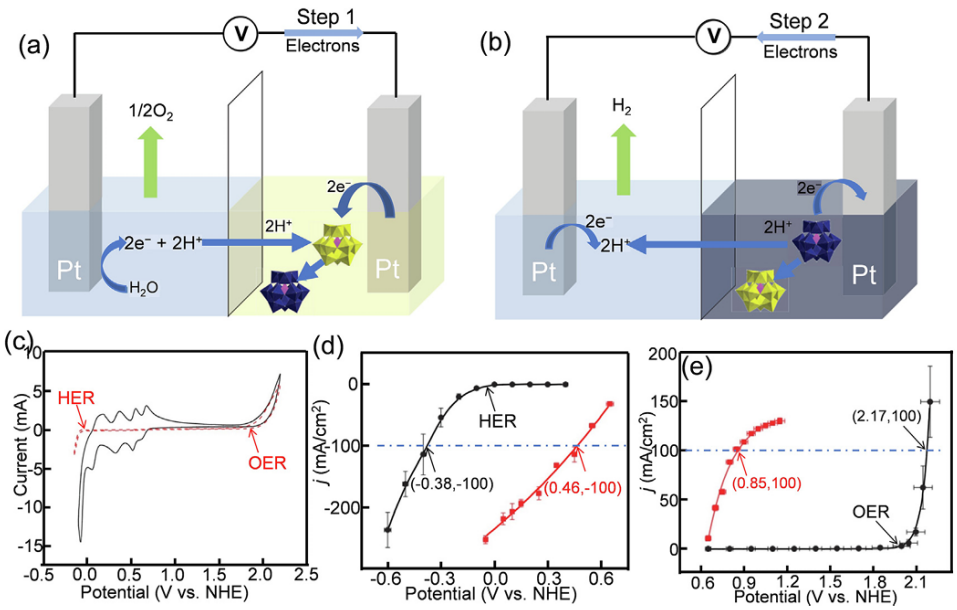

Figure 1.13. *(a and b) Schematic of the ECPB-based approach to decoupled water splitting. (c) CVs of 0.5 M phosphomolybdic acid (solid black) and 1.0 M H_3PO_4 (dashed red). (d and e) Current-voltage curves for the reduction (d) and oxidation (e) of 1.0 M H_3PO_4 solution with (red) and without (black)ECPB/ECPB* mixture.* [64]

During operation, oxygen and protons were first generated at the anode, while the ECPB in the cathodic compartment underwent reduction and protonation. When the electrical bias was reversed, the electrons and protons stored in the ECPB were released at the anode, and equivalent amounts of hydrogen were generated at the HER cathode. Electrochemical tests indicate that the redox peaks of ECPB fall within the ranges of the HER and OER onset potentials (Fig. 1.13c). ECPB reduction occurred preferentially over HER (Fig. 1.13d), and ECPB* was considerably easier to oxidise than water (Fig. 1.13e). The pH of the electrolyte remained unchanged, which was attributed to the ECPB's good buffering ability.

Cronin's group further explored hydroquinone sulfonate (HQMS) as a redox mediator, owing to its high water solubility (0.5 M), appropriate redox potential (0.7 V vs NHE), and pH-buffering capacity. At a current density of 50 mA/cm^2, the decoupled HER and OER reactions achieved an impressive 99% efficiency compared to one-step water splitting. The pH remained relatively stable, indicating that HQMS could effectively carry protons and electrons. However, the system's stability was limited, showing a capacity drop of approximately 1% per cycle.[64] To enhance stability, Cronin's group utilised anthraquinone-2,7-sulfonic acid (AQDS) as a

redox mediator to separate HER and OER spatially. In 1 M H_2SO_4, 25 mM AQDS exhibited a redox potential of only 0.214 V (vs SHE), which is positioned between the HER and OER. This suggests that Anthraquinone 2,7-Sulfonate Acid (AQDS) can act as a redox mediator, decoupling water into two electrochemical reactions. The system demonstrates high stability, with its capacity decreasing by only 5.75% after 100 hours, approximately 17 times greater than HQMS. By analysing the H_2/O_2 volumes, the coulombic and Faradaic efficiency was shown to be nearly 100%. Gas chromatography headspace analysis (GCHA) further confirmed the complete separation of H_2 and O_2. During charging, the AQDS oxidation current directly correlates with the rate of H_2 production. The polarisation curve shows a significant tolerance to high current densities, reaching 3.71 A/cm2 at 2 V. Despite its excellent performance, AQDS is susceptible to disproportionation reactions during its transition from reduced to oxidised states, which affects its overall stability.

In 2014, Rausch *et al.* explored silicotungstic acid ($H_4SiW_{12}O_{40}$) as an alternative polyoxometalate-based decoupling agent.[68] Compared to phosphomolybdic acid, the first two redox waves of silicotungstic acid are significantly more cathodic, with E½ (half-wave redox potential) values of +0.01 and –0.22 V (*vs* NHE) at pH 0.5 (Fig.1.14a), indicating a fast electron transfer process characterised by two pairs of redox peaks, corresponding to the following reactions:

Peak 1: $H_4SiW_{12}O_{40} + H^+ + e^- \leftrightarrow H_5SiW_{12}O_{40}$ [11]

Peak ll: $H_5SiW_{12}O_{40} + H^+ + e^- \leftrightarrow H_6SiW_{12}O_{40}$ [12]

A carbon electrode is used to conduct the 2-electron reduction from $H_4SiW_{12}O_{40}$ to $H_6SiW_{12}O_{40}$. When the reduced mediator comes in contact with the Pt catalyst (Fig. 1 .14 b), H_2 is produced spontaneously because of the relatively high redox potential of the HER on the Pt catalyst, in which $H_6SiW_{12}O_{40}$ completely transfers back to $H_5SiW_{12}O_{40}$, and $H_5SiW_{12}O_{40}$ partially transfers back to $H_4SiW_{12}O_{40}$, respectively. This process can be reversed by electro-reducing $H_5[SiW_{12}O_{40}]$ at the cathode electrode. On the other hand, starting from the fully oxidised species $H_4[SiW_{12}O_{40}]$, the one-electron reduced species can be accessed either by electrochemical reduction or by reaction with hydrogen in the presence of a suitable catalyst such as Pt/C.[68]

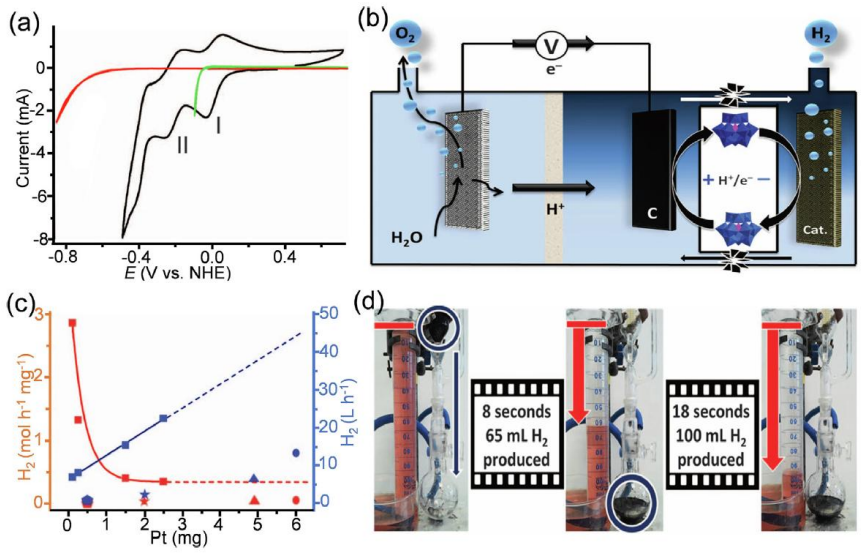

Figure. 1.14. *(a) Reductive CVs of 0.5 M $H_4SiW_{12}O_{40}$ at pH 0.5 (black) on a glassy Carbon electrode, 1.0 M H_3PO_4 at pH 1.0 on a glassy Carbon electrode (red), and on a Pt (green) electrode. (b) A schematic of silicotungstic acid-mediated H_2 evolution from water. (c) Comparison of the rate of H_2 production using electrolysis mediated by silicotungstic acid (square) and some recent state-of-the-art electrolysers (pentagons, stars, triangles, and dots). (d) Typical apparatus configuration for determining volumes of H_2 evolved when $H_6SiW_{12}O_{40}$ was exposed to powdered catalysts.* [64]

The same work shows that a sample of silicotungstic acid subjected to 20 consecutive two-electron reduction and reoxidation cycles has an ultraviolet-visible spectrum indistinguishable from that of a fresh sample of silicotungstic acid, suggesting that the mediator is stable to redox cycling under these conditions and that $H_4[SiW_{12}O_{40}]$ might thus be suitable as a mediator in a continuous-flow system.[68]

Chisholm *et al.* subsequently demonstrated that using a polyoxometalate electrolyte as a decoupling agent enables the effective and safe utilisation of the low-power inputs typical of renewable energy sources.[69,73] This work thus highlights the potential advantages of using silicotungstic acid as a redox mediator for water electrolysis over a wide range of current densities, with implications for harnessing renewable power for hydrogen production. This contrasts with conventional electrolysers, which risk producing hazardous hydrogen-oxygen mixtures under such conditions. Chisholm *et al.*[69] demonstrated that decoupled electrolysis shows substantial promise for minimising gas crossover across a current density range of 25-

500 mA/cm^2 (and therefore has some in-built flexibility for low-power inputs). Still, several avenues for optimisation and open research questions remain. For example, the flow cell in Chisholm's study used expensive catalyst-coated membranes and was tested only at current densities up to 500 mA/cm^2. However, conventional proton exchange membrane cells operate at around 2 A/cm^2 (or higher) today. [69]

Wang *et al.* synthesised tetra-substituted hydroquinone, tetra-mercapto propane-sulfonate hydroquinone (TMSQ), to function as a redox mediator. TMQ showed exceptional stability with minimal decomposition during cycling in its reduced form. Even at 50 °C, the cell capacity remained almost unchanged at a current density of 50 mA/cm^2.[72] Remarkably, even with complete TMQ degradation, 80% of the capacity was retained, as the primary degradation product was TMHQ. Compared to direct water electrolysis, which requires 1.5 V, the hydrogen evolution reaction (HER) and oxygen evolution reaction (OER) require only 0.60 V and 0.85 V, respectively. Under conditions of 50 °C, 1 M H_2SO_4, and a current density of 250 mA/cm^2, the system achieved an energy efficiency of 62.4%, comparable to the best AQDS, a notably high value.[72] A stability comparison of these hydroquinone/quinone redox mediators is shown in Table 2.

Chen *et al.* designed a polyoxometalate cluster redox mediator, $H_{18}Li_6[P_2W_{18}O_{62}]$ (LiPWO), that can store 18 electrons and 18 protons,[87] to improve electron-proton coupling and release capabilities while maintaining a low *pH*. When the concentration of the mediator is 2 mM, only 4 electrons can be recovered; at 50 mM, 16; and at 100 mM, 17.2, indicating that this mediator has strong electron-proton coupling capabilities.[87]

Amstutz *et al*. utilised two pairs of redox mediators, V(III)/V(II) and Ce(IV)/Ce(III), to separate HER and OER,[88] employing a flow system that merges two technologies for renewable electrochemical energy storage and renewable power-to-gas. This dual-element system has the potential to circumvent the low energy density of the redox flow system, thereby storing excess energy as hydrogen. The potentials of V(III)/V(II) (–0.26 V vs SHE) and Ce(IV)/Ce(III) (1.44 V vs SHE) in sulfuric acid are beyond the thermodynamic limit of HER and OER reactions, respectively.[88,89] V(III) and Ce(III) are electrochemically charged in the conventional redox flow battery and then chemically discharged as they flow through the HER and OER catalyst tanks for successive hydrogen and oxygen production, respectively.

Similarly, Reynard *et al.* also changed the anode mediator from Ce(IV)/Ce(III) to VO2+/VO2+, whilst the catholyte remained V(III)/V(II) to complete the flow system. [89] The

technique allows surplus electricity to be stored as hydrogen beyond the limited energy density of the redox flow battery electrolytes. The rapid discharge of electrolytes also provides an immediate sink for excess electricity.

Zhang *et al.* utilised 7,8-dihydroxy-2-phenazine sulfonic acid (DHPS/DHPS-2H) and $[Fe(CN)_6]^{3-/4-}$ as two pairs of redox mediators to form a complete redox flow battery for the decoupling of water electrolysis (Fig. 1.15).[75] In a 4 M NaOH solution, the redox potential of DHPS is 0.05 V (vs RHE). At this alkaline concentration, DHPS exhibits a less negative potential than HER, thereby reducing the overpotential at the electrode and allowing DHPS reduction to occur before HER, thereby avoiding hydrogen gas production at the electrode.[75] $Pt/Ni(OH)_2$ and $NiFe(OH)_2$ were used as catalysts in the two tanks to accelerate HER and OER reactions. Because the catalyst is detached from the electrode, its quantity is not limited by its small surface area, allowing a higher catalyst load to boost the generation rate.

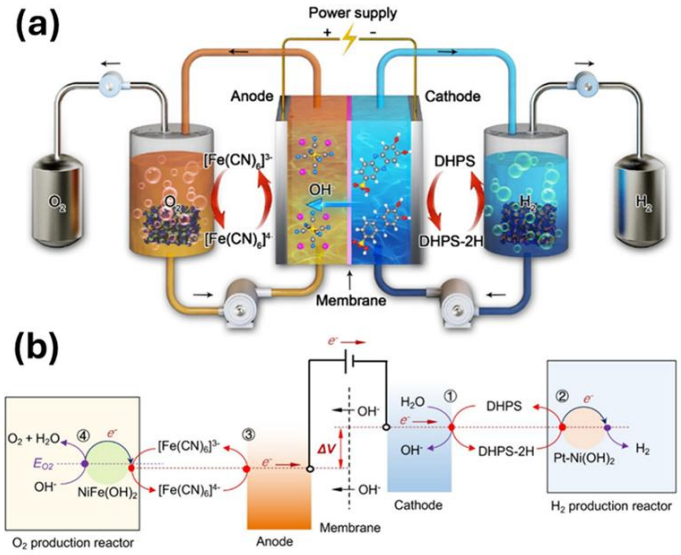

***Figure 1.15**. A redox flow electrolytic cell in alkaline medium for decoupled electrochemical water splitting employing two different Redox mediators (a) Schematic illustration of the device. (b) Energy diagram showing the mechanistic pathway of the reactions taking place in the electrolyser* [75]

During operation, the reduced DHPS-2H functions as a proton and electron carrier, bypassing the slow water dissociation step in the hydrogen evolution reaction (HER) during alkaline water electrolysis. Moreover, the dehydrogenation of DHPS-2H occurs spontaneously under the catalyst's influence, eliminating the need for additional energy input. For the OER side, $[Fe(CN)_6]^{3-}$ works as a charge carrier, activating O_2 generation when it flows through a

$NiFe(OH)_2$ catalyst bed in a separate reactor tank.[75,89,90] With such a pair of anodic and cathodic redox mediators, these systems can store electrical energy in the form of charged redox species, either as a conventional redox flow battery or for on-demand hydrogen production. Generally, adding a mediator reduces the reaction's overpotential, improving efficiency and lowering the required voltage.[85,90] Some systems have shown a voltage of 1.5 V at 100 mA/cm^2, depending on the mediator and reaction conditions. By optimising the mediator and electrode materials, energy input can be minimised while maintaining high conversion rates.[90]

1.5. Conclusion

Producing low-cost hydrogen from renewable electricity such as wind and solar can significantly decarbonise hard-to-abate industries and drive the global energy transition toward a carbon-neutral economy. Water electrolysis has attracted significant attention for this purpose.

Compared to other hydrogen production methods, water electrolysis has the advantage of producing extremely pure, zero-carbon hydrogen. The proton exchange membrane (PEM) technology is a promising option for the commercialisation of green hydrogen compared to other technologies. However, PEM technology remains costly when coupled with renewable energy sources and often faces drawbacks such as gas crossover, high production costs, and electrolyser/component degradation.

Decoupled water electrolysis using a redox mediator is a promising technique that has attracted growing interest for overcoming the limitations of traditional electrochemical reactions, such as enhancing flexibility and safety. In this chapter, we have introduced the core concepts underlying this technique and the key factors contributing to its effectiveness, including electrode materials, cell design, and the choice of electrolyte mediators. Redox mediators have been shown to undergo multiple reversible redox reactions, which are of great scientific interest in the present thesis. We have also provided an overview of the use of polyoxometalates (e.g., Silicotungstic acid) as a redox mediator in decoupled electrochemical water splitting, which constitutes the primary research topic of this thesis. Moreover, by presenting examples from recent literature, we have also discussed the effectiveness of this technique for hydrogen production with potentially reduced gas crossover and component degradation in water electrolysis technology.

1.6. Research Aims/Objectives

The objective of the research reported in this thesis was to answer a number of outstanding questions related to practical decoupled electrolysis using liquid-phase mediators. We chose to focus on silicotungstic acid as the mediator, as it has proven stability and has been well-defined as a mediator for decoupled electrolysis. The specific objectives were:

Objective 1: To adapt Chisholm's silicotungstic acid decoupled flow cell set-up from the literature[15] in a manner that would allow components to be easily swapped in and out (and allowing the effects of doing so to be compared).

Objective 2: To explore the effect of the current density applied across the oxygen-generating cell on the extent of parasitic hydrogen production and hydrogen crossover into the anode stream. Is it possible to drive oxygen evolution with concomitant silicotungstic acid reduction at current densities >500 mA cm^{-2} without significant hydrogen production in the cell?

Objective 3: To explore the effect on the electrochemical process of applying the anode catalyst onto the GDL of the oxygen-generating cell, as opposed to a more conventional catalyst-coated membrane arrangement. A catalyst-on-GDL arrangement could offer improved options for using alternative catalysts, but does this come at the cost of energy efficiency?
Objective 4: To compare the effects of using a dialysis membrane as the separator in the oxygen-generating cell, as opposed to the perfluorinated membranes mostly studied to date. Dialysis membranes should be cheaper to buy and easier to recycle (or dispose of) than perfluorinated compounds, which are considered "forever chemicals".

References

1. B.S. Zainal, P.J. Ker, H. Mohamed, H.C. Ong, I.M.R. Fattah, S.M.A. Rahman, L.D. Nghiem, T.M.I. Mahlia. *Renew. And Sust. Energy Reviews***,** 2024, 189, 113941.
2. J. Li, Y. Ma, X. Mu, X Wang, Y. Li, H. Ma, Z. Guo. *Adv. Sci.* 2024, 2411964–2411999.
3. H. Kojima, K. Nagasawa, N. Todoroki, Y. Ito, T. Matsui, R. Nakajima. *Int. J. Hydrogen Energy,* 2023, 48, 4572–4593.
4. E.B. Agyekum, C. Nutakor, A.M. Agwa, S. Kamel. *Membranes,* 2022, 12, 173.
5. Glenk G, Reichelstein S. *Nat. Energy,* 2019, 4, 216–228.
6. International Energy Agency. Hydrogen. https://www.iea.org/reports/hydrogen. [Accessed 12 April 2025].
7. International Energy Agency. Net zero by 2050: A roadmap for the global energy sector 2021. [Accessed 12 April 2025].
8. M. Carmo, D.L. Fritz, J. Mergel, D. Stolten. *Int. J. H. Energy,* 2013, 38, 4901–4934.
9. J.O. Abe, A.P.I. Popoola, E. Ajenifuja, O.M. Popoola. *Int. J. Hydrogen Energy*, 2019, 44, 15072–15086.
10. K. Christopher and R. Dimitios. *Energy Environ. Sci.* 2012, 5, 6640.
11. Y. Shi, Z. Qiu, S.W. Snyder, and Y.Wang. *Energy Strategy Rev*, 2024, 56, 101565.
12. E.A. Hamedani, S.A. Alenabi, S. Talebi. *Energy Reports*, 2024, 12, 3778-3794.
13. S. Shashi, Agarwal, S. A. Jain. *Energies,* 2021, 14, 7389.
14. Hydrogen Council. Path to Hydrogen Competitiveness: A Cost Perspective; Hydrogen Council: Brussels, Belgium, 2020, 1–88.
15. M. Newborough, G. Cooley. *Fuel Cells Bull*. 2020, 16–22.
16. J. B. Kabeyi and O. A. Olanrewaju. *Frontiers in Energy Research*, 2022, 9, 743114.
17. M. Younas, S. Shafique, A. Hafeez, F. Javed, F. Rehman. *Fuel,* 2022, 316, 12331–12354.
18. Q. Hassan, P. Viktor, T.J. Al-Musawi, B.M. Ali. *Renew. Energy Focus,* 2024, 48, 100545–100561.
19. D. Astiaso García. *Int. J. Hydrogen Energy,*2017*,* 42, 6435–6447.
20. K. Shu, B. Guan, Z. Zhuang, J. Chen, L. Zhu, Z. Ma, X. Hu, C. Zhu, S. Zhao, H. Dang, T. Zhu. *Int. J. Hydrogen Energy,* 2025, 97, 160-213.
21. A special report by the International Energy Agency (IEA). Net zero by 2050: A roadmap for the global energy sector. Available on: https://www.iea.org/reports/net-zero-by-2050.

22. Hydrogen for net zero: A critical cost-competitive energy vector. By Hydrogen Council 2021. [Accessed 20 May 2025].
23. Taibi E, Miranda R, Carmo M, Blanco H. Green hydrogen cost reduction. By the International Renewable Energy Agency (IRENA). https://www.irena.org/publications/2020/Dec/ Green-hydrogen-cost-reduction; 2020
24. A.M. Sadeq, R.Z. Homod, A.K. Hussein, H. Togun, A. Mahmoodi, H.F. Isleem, A.R. Patil. *Sci. of the Total Env.* 2024, 939, 173622.
25. M.M.H. Bhuiyan and Z. Siddique. *Int. J. Hydrogen Energy,* 2025, 102, 1026-1044.
26. S.O. Amrouche, D. Rekioua, T. Rekioua. Int. J. Hydrogen Energy, 2016, 20914-20927.
27. E.T. Sayed, A.G. Olabi, A.H. Alami, A. Radwan, A. Mdallal. *Energies,* 2023, *16*, 1415.
28. T. Egeland-Eriksen, A. Hajizadeh, S. Sartori. *Int. J. Hydrogen Energy,* 2021, 46, 31963–31983.
29. Balat. M. *Energy Sources, Part A:* 2008, 31, 39–50.
30. K. Mazloomi and C. Gomes. *Renew. And Sust. Energy Rev.,* 2012, 16, 3024–3033.
31. A.R. Limongi, E. Viviano, M. De Luca, R.P. Radice, G. Bianco, G. Martelli. *Appl. Sci.* 2021, *11*, 1616.
32. Stucki S, Scherer G.G. *J. Appl. Electrochem*. 1998, 28,1041–1049.
33. G. Ruan, Todman, F. Yogev, G. *et al. Nat. Rev. Clean Technol.* 2025, 1, 380–395.
34. S.A. Grigoriev, V.I. Porembskiy, S.V. Korobtsev, V.N. Fateev, F. Auprêtre, P. Millet *Int. J. Hydrogen Energy*, 2011, 36, 2721–2728.
35. W. Li, H. Tian, L. Ma, Y. Wang, X. Liu, X. Gao. *Mater. Adv.,* 2022, 3, 5598–5644.
36. S. Garbe, J. Futter, T.J. Schmidt, L. Gubler. *Electrochimica Acta*, 2021, 377,138046.
37. F.Y. Tuhi, M. Bucelli, Y. Liu. *Int. J. Hydrogen Energy,* 2024, 94, 608–625.
38. B. Choi, D. Panthi, M. Nakoji, T. Kabutomori, K.Tsutsumi, A. Tsutsumi. *Chem. Eng. Sci.,* 2017, 157, 200–208.
39. A. Raveendran, M. Chandran, R. Dhanusuraman. *RSC Adv.,* 2023, 13,3843–3876.
40. S. Kharel, B. Shabani. - *Energies,* 2018,11, 2825–2842.
41. L. Chen, X. Dong, Y. Wang, Y. Xia. *Nat. Commun.* 2016, *7*, 11741–11749.
42. R.N. Mutlu, I. Kucukkara, A.M. Gizir. 2020, *Int. J. Hydrogen Energy,*2020*,* 12641–12652.

43. P. A. Lessing. *J. Mat. Sci*, 2007, 42, 3477–3487.

44. K.G. dos Santos, C.T. Eckert, E. De Rossi, R.A. Bariccatti, E.P. Frigo, C.A. Lindino, H.J. Alves. *Renew. And Sust. Ener. Rev*, 2017, 563–571.

45. A. Khataee, A. Shirole, P. Jannasch, A. Kruger, and A. Cornell. *J. Mater. Chem. A*, 2022, 10, 16061–16070.

46. M. David, C. Ocampo-Martínez, R. Sánchez-Peña. *J. Energy Storage*, 2019, 23, 392–403.

47. Y. Leng, G. Chen, A. J. Mendoza, T. B. Tighe, M. A. Hickner and C.-Y. Wang, *J. Am. Chem. Soc.,* 2012, 134, 9054–9057.

48. U.K. Ghorui, G. Sivaguru, U.B. Teja, S. Ramakrishna, S. Ghosh, G.K. Dalapati, S. Chakrabortty. *ACS Appl. Energy Mater.*, 2024, 7, 7649−7676.

49. S.S. Kumar and H. Lim. *Energy Reports*, 2022, 8, 13793–13813.

50. M. Ni, Michael K.H. Leung, Dennis Y.C. Leung. *Int. J. Hydrogen Energy,* 2008, 33, 2337–2354.

51. Zheng, Y., Chen, Z. and Zhang. *J. Electrochem. Energy. Rev*. 2021, 4, 508–517.

52. A. Khataee, A. Shirole, P. Jannasch, A. Kruger, and A. Cornell. *J. Mater. Chem. A*, 2022, 10, 16061–16070.

53. Weiquan Li *et al,* 2020 IOP Conf. Ser: *Earth Environ. Sci.* 619 012012.

54. S. Aslam, S. Rani, K. Lal, M. Fatima, T. Hardwick, B. Shirinfar, N. Ahmed *Green Chem.,* 2023, 25, 9543–9573.

55. S.G. Nnabuife, J. Ugbeh-Johnson, N.E. Okeke, C. Ogbonnaya. *Carbon Capture Sci. & Tech.,* 2022, 3, 100042–100061.

56. S. Krishnan, V. Koning, M.T. de Groot, A. de Groot. *Int. J. Hydrogen Energy*, 2023, 48, 32313–32330.

57. S. Krishnan, B. Corona, G.J. Kramer, M. Junginger. *Int. J. Hydrogen Energy*, 2024, 55, 26–41.

58. T. Wang, X. Cao, L. Jiao. *Carbon Neutrality*, 2022, 1–21.

59. A. Z. Arsad, M.A. Hannan, A.Q. Al-Shetwi, R.A. Begum. *Int. J. Hydrogen Energy*, 2023, 48, 27841–27871.

60. X. Guo, H. Zhu, S. Zhang. *Intl. J. Hydrogen Energy,* 2024, 49, 1048–1059.

61. M. Möckl, M. Bernt, J. Schröter. *Int. J. Hydrogen Energy*, 2020, 45, 1417–1428.

62. P. Molina, C. Rios, C. Martinez de Leon, J.J. Brey. *Int. J. Hydrogen Energy*, 2025, 107, 656–665.
63. M.N.I. Salehmin, T. Husaini, J. Goh, A.B. Sulong. *Energy Con. and Mgt.,* 2022, 268, 115985.
64. M.D. Symes, L. Cronin, *Nat. Chem.* 2013, 5, 403–409.
65. Z.P. Ifkovits, J.M. Evans, M.C. Meier, K.M. Papadantonakis, N.S. Lewis. *Energy Environ. Sci*., 2021, 14, 4740–4759.
66. Dotan *et al*. *Nat. Energy.* 2019, 4, 786-795.
67. J. Wang, L. Ji, X. Teng, Y. Liu, L. Guo, Z. Chen, *J. Mater. Chem. A,* 2019, *7*, 13149–13153.
68. B. Rausch, M.D. Symes, G. Chisholm, L. Cronin. *Science,* 2014, 345, 1326–1333.
69. G. Chisholm, Leroy Cronin, and Mark D. Symes. *Electrochimica Acta*, 2020, 331, 135255.
70. A. Paul and Mark D. Symes, *Green and Sust. Chemistry 2021, 29,100453*2021.
71. P. J. McHugh, Athanasios D. Stergiou, and Mark D. Symes. *Adv. Energy Mater.* 2020, 10, 2002453.
72. J. Huang, and Y. Wang. *Cell Reports Phys. Sci*. 2020, 1, 100138.
73. G. Chisholm, L. Cronin. *Renew. Energy Sources*. 2016, 315–343.
74. T. Wu, Y. Hu, M. Li, B. Han, Z. Liang, D. Geng. *Int. J. Hydrogen Energy,* 2023, 48, 35552–35560.
75. F. Zhang, Q. Wang. *ACS Materials Lett.* 2021, 3, 641–651.
76. W. Shao, B. Lu, J Cao, J. Zhang, H. Cao. *Chem. Asian J.* 2023, *18*, 1–15.
77. Z. P. Ifkovits, J. M. Evans, M. C. Meier, K. M. Papadantonakis, N. S. Lewis, *Energy Environ. Sci.* 2021, *14*, 4740–4759.
78. R. Francke, R. D. Little. *Chem. Soc. Rev.* 2014, *43*, 2492–2521.
79. K. Zhou, J. Huang, D. Xiang, A. Deng, J. Du. *J. Energy Chemistry,* 2024, 94,340–356.
80. C.W. Anson, and S.S. Stahl. *Chem. Rev.* 2020, 120, 3749−3786.
81. L.G. Bloor, R. Solarska, K. Bienkowski, P.J. Kulesza, J. Augustynski, M.D. Symes, L. Cronin. *J. Am. Chem. Soc*., 2016, 138, 6707–6710.
82. F. Li, F. Yu, J. Du, Y. Wang, Y. Zhu, X. Li, L. Sun, *Chem. Asian J.* 2017,12, 2666–2669.
83. L. MacDonald, J.C. McGlynn, N. Irvine, I. Alshibane, L.G. Bloor, B. Rausch, J.S.J. Hargreaves, L. Cronin, *Sustain. Energy Fuels*, 2017, 1, 782–1787.

84. Lei, J.-J. Yang, T. Liu, R.-M. Yuan, D.-R. Deng, M.-S. Zheng, J.-J. Chen, L. Cronin, Q.-F. Dong, *Chem. Eur. J., 2019,* 25, 11432–11436.
85. X. K. Wan, H. B. Wu, B. Y. Guan, D. Luan, X. W. D. Lou, *Adv. Mater.* 2020, 32, 1901349.
86. F. Wang, H. Sheng, W. Li, J. B. Gerken, S. Jin, S. S. Stahl, *ACS Energy Lett.* 2021, 1533–1539.
87. J. J. Chen, M. D. Symes, L. Cronin. *Nat. Chem.* 2018, *10*, 1042–1047.
88. V. Amstutz, K. E. Toghill, F. Powlesland, H. Vrubel, C. Comninellis, X. Hu, H. Girault, *Energy Environ. Sci.* 2014, *7*, 2350–2358.
89. D. Reynard, G. Bolik-Coulon, S. Maye, H. H. Girault, *Chem. Eng. J.* 2021, 407.
90. P. Peljo, H. Vrubel, V. Amstutz, J. Pandard, J. Morgado, A. Santasalo-Aarnio, D. Lloyd, F. Gumy, C. R. Dennison, K. E. Toghill, H. H. Girault, *Green Chem.* 2016, *18*, 1785–1797.

CHAPTER TWO

EXPERIMENTAL/METHODOLOGY

2.1. Electrochemical Techniques

Different electrochemical and physicochemical techniques were employed to monitor changes in potential, current, charge passed, and electrode surface during the reduction of the redox mediator for the hydrogen evolution reaction. This enables us to gain insight into vital information about both the target reactions and the materials within the electrochemical system. The following section will cover the basics of electrochemistry, and several other analytical methods used throughout the rest of the thesis.

2.1.1. Cyclic voltammetry

Cyclic voltammetry (CV) is an electrochemical technique that measures the current flow resulting from the application of a potential to the working electrode. For the cyclic voltammogram test, a conventional three-electrode system immersed in the mediator (silicotungstic acid) at a scan rate of 10 mV/s was used to complete the electric circuit, consisting of a glassy carbon as the working electrode (WE), Platinum (Pt) Flag as counter electrode (CE) and silver, silver chloride (Ag/Agcl) as the reference electrode (RE) Fig 2.1b. The potential is measured between the working electrode (WE) and the reference electrode (RE), whereas the current is measured between the working electrode and the counter electrode (CE).[1] The electrochemical current is plotted on the x-axis and the WE potential on the y-axis (Fig.2.1a). During measurements, the WE potential reaches a set potential before reversing to its initial potential. This is the reason we called it CV. We may repeat this cyclic experiment as many times as we desire. Thus, CV is performed by cycling the WE potential and measuring the resulting electrochemical current during oxidation and reduction of the redox-active species. During the redox reaction, electrons are transferred from the analyte to the WE or from the WE to the analyte. CV is used to study the electrochemical properties of an analyte in solution or a material coated onto the electrode surface.

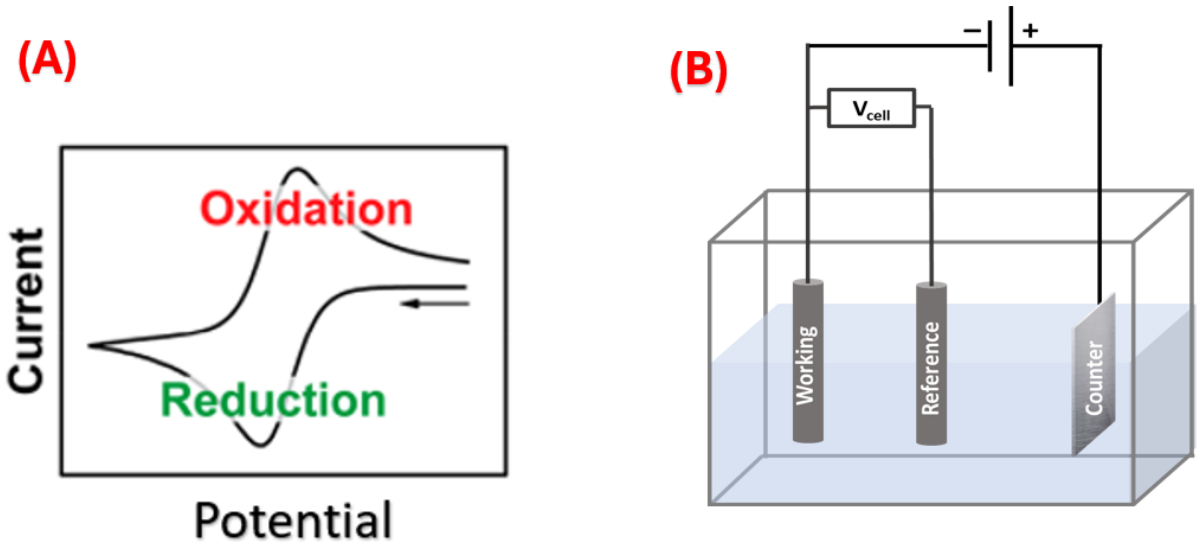

Figure 2.1. (A) *Schematic of a cyclic voltammogram*[1] *(B) Typical experimental set-up used in this project to collect CVs.*

Ag/AgCl and the standard hydrogen electrode (SHE) reference electrodes can be used in aqueous solutions, whereas an $Ag/AgNO_3$ reference electrode is often used in reactions involving organic solvents. However, in the case of reference electrodes in organic solvents, these can be described as part of a larger class of pseudo-references, i.e., references in which the potential is not constant but varies predictably.[2] A potentiostat is used to control the applied potential of the working electrode relative to the reference electrode potential. The most important aspect of the working electrode for probing the redox activity of dissolved analytes is that it is composed of redox-inert material in a given potential range.[3] The type of working electrode can be varied from experiment to experiment to provide different potential windows or to reduce/promote the surface adsorption of the species of interest.[1-3] In Chapter 3 of this thesis, cyclic voltammetry was employed to measure the redox behaviour of the mediator.

2.1.2. Principles of bulk electrolysis

The bulk electrolysis method involves applying a constant potential (chronopotentiometry/galvanostatic mode) or a constant current (chronoamperometry/potentiostatic mode). In a controlled potential electrolysis (CPE) experiment, the working electrode is held at a constant potential. The electrolysis potential is usually chosen, for example, to be slightly more positive than the $E_{1/2}$ (half-wave redox potential) value of a species being oxidised or somewhat more negative than the $E_{1/2}$ value of

a species being reduced, and hence just into the limiting current region of a steady state condition (a situation where the concentration of the electroactive material reaching the surface of the electrode is unchanging with time and potential). In a constant current or galvanostatic experiment, as the name implies, the current is maintained at a constant value for the desired period.[4] In a coulometry experiment commonly undertaken during bulk electrolysis, the current passed as a function of time is integrated by an electronic integrator or coulometer to give the charge. Faraday's law of electrolysis requires that the quantity of electricity (coulombs) passed is directly proportional to the amount of chemical reaction (moles) that has taken place at an electrode. Faraday's law of electrolysis can then be used to determine the theoretical yield according to the equation below

$$Q = It \qquad (2.1)$$

$$Q = mnF \qquad (2.2)$$

where I is the current, *t is time, and* Q is the charge or number of coulombs passed during the electrolysis experiment, m is the theoretical number of moles of product formed in the reaction, n is the number of electrons transferred in the experiment per mole, and F is Faraday's constant (96485 C mol^{-1}). From equations 2.1 and 2.2, it is possible to determine the theoretical yield from an electrochemical reaction.[5] However, one cannot control the reaction rate. The opposite is true in galvanostatic electrolysis, where the reaction rate can be set and maintained.[5,6] The complete process occurs in an electrochemical cell in which oxidation and reduction processes can be separated into two chambers. A proton exchange membrane (e.g., Nafion) can separate these chambers. Externally, a potentiostat connects the anode and cathode to the power supply. While the power supply drives electrons from the anode to the cathode, an equal number of protons pass through the membrane. At the cathode, protons and electrons recombine to form hydrogen gas. Bulk electrolysis is widely used in Chapters 3-4 of this work, where a constant current is applied to determine the cell potential.

2.1.3. Electrochemical Impedance Spectroscopy

EIS was used to gain deeper insight into the resistances in the decoupled electrolysis set-up. EIS analysis measures resistance (R), capacitance (C), and inductance (L) by monitoring the current response to an applied AC voltage in an electrochemical cell. When a DC voltage is applied, the relation between R, V, and I satisfy Ohm's law, as shown in Eq. 2.3. Similarly, when an AC voltage is applied to an electrochemical cell, the impedance can be expressed as V(ω) / I(ω), the equation for Ohm's law in an AC circuit. Therefore, the impedance is the resistance that obstructs the flow of alternating current when an AC voltage is applied to the circuit. These obstructions are represented by various circuit elements, such as resistors, inductors, and capacitors, which constitute the overall impedance in a circuit.[7] It is well established that all conductors will show some resistance to an electrical current; this value is often expressed using Ohm's law for resistance (Eqn. 2.3)

$$R = \frac{V}{I} \qquad (2.3)$$

Where R is resistance, V is the applied voltage and I is current. However, this law holds only for an ideal resistor, which, among other things, assumes that alternating potentials and their resulting currents are in phase when passing through a resistor. In practice, a phase shift exists between the applied AC potential and the current response (Fig. 2.2). This phase shift is measured at different frequencies to provide a more accurate insight into the resistance or impedance within an electrochemical system.

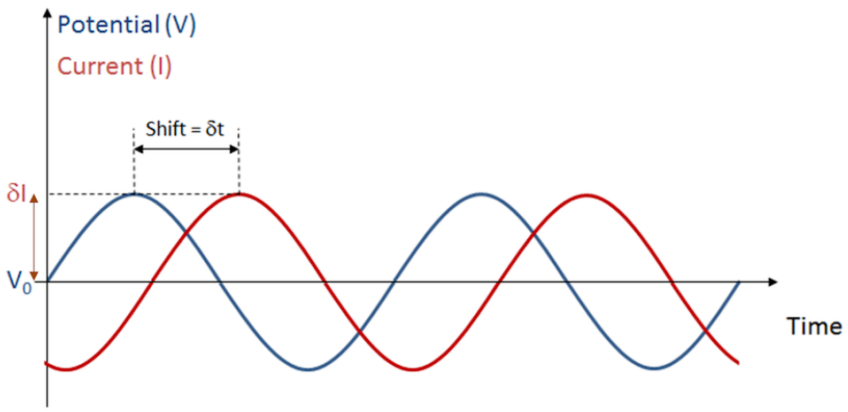

Figure 2.2. *Diagram of AC excitation signal (blue line) and current response (red line) through a resistor, where a phase shift separates the two signals.* [8]

EIS measurements typically vary the frequency of the applied perturbation across the range from mHz to kHz. The relative amplitude of the response and phase shift between the input and output signals change with the applied frequency. Different frequencies can separate processes with different timescales. For example, at lower frequencies, slow electrochemical reactions proceed in response to the cell's alternating polarisation. At higher frequencies, the applied field changes direction faster than the chemistry responds, so the response is dominated by capacitance from the charge and discharge of the cell. EIS data from electrochemical experiments are often fitted to an equivalent circuit to more easily represent the individual resistances associated with the processes in the system; these can be represented as standard circuit components (e.g., resistors, capacitors, inductors, etc.).[8] The Randles circuit is a well-known equivalent circuit model used in electrochemical impedance spectroscopy (EIS) to represent the behaviour of electrochemical systems. The Radles circuit used in this work was obtained using a potentiostat (Biologic SP-150, paired with a Biologic VMP 3B 20 A/20 V booster), as shown in Fig. 2.3. It typically consists of a resistor in series with a parallel combination of another resistor and a capacitor. In this circuit, R1 represents the ohmic resistance of the flow cell components, and R2 and R3 represent the cathodic and anodic charge-transfer resistances, respectively. Meanwhile, C2 and C3 correspond to the constant phase elements associated with the cathodic and anodic processes, and W is the Warburg element.[7]

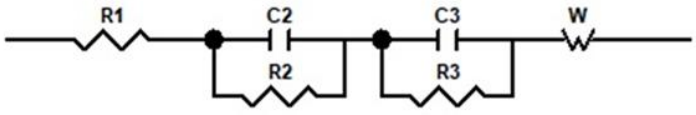

Figure 2.3. *(a) Diagram of a Randles circuit commonly used as an equivalent circuit in this work. The obtained electrochemical impedance spectroscopy data were fitted to an equivalent electrical circuit using BioLogic EC-Lab software, selecting the model that yielded the lowest chi-squared (χ^2) value that was consistent with literature reports.*[7]

Figure 2.4 shows a typical Nyquist plot. The impedance at high frequency, where it intercepts the x-axis, is the ohmic resistance. The difference between the higher- and lower-frequency intercepts is the polarisation resistance, which can be determined from the semicircle's diameter.[7,8] The Nyquist plot, shown in Fig. 2.4, provides insight into the possible mechanism of an equivalent circuit model system.

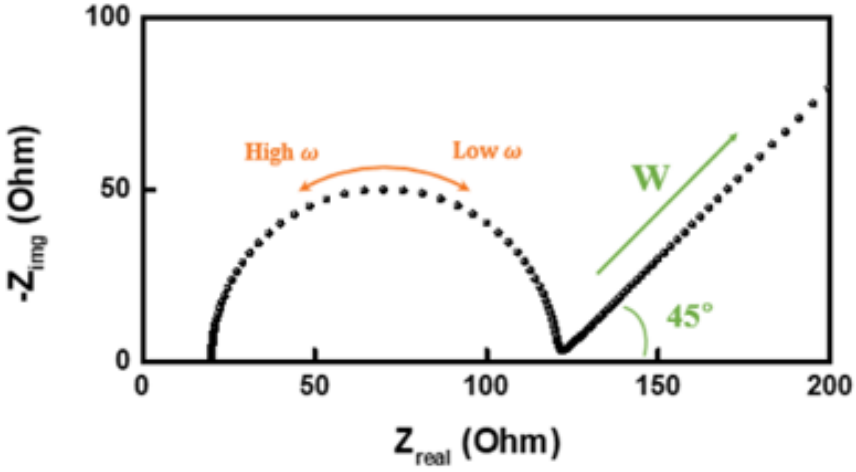

Figure 2.4. *Typical Nyquist plot observed for an electrolyser* [8]

Due to its convenience for analysing the active reaction mechanism, the Nyquist plot is more commonly used to characterise lithium-ion batteries.[7,8] The EIS technique has been employed to measure flow cell resistance in Chapter 4 of this thesis.

2.2. Physicochemical Techniques

2.2.1. Scanning Electron Microscope (SEM)

Electron microscopy allows imaging the surface of a specimen. This technique utilises electron-specimen interactions to generate topological images. With magnifications higher than those of the light microscope, electron microscopy has enabled researchers to observe matter in greater detail, well beyond the capabilities of the naked human eye.[9] Generally, two types of interactions can occur: elastic and inelastic. In the inelastic interaction, low-energy secondary electrons (SEs) are emitted from the samples after the primary beam electrons have bombarded them. On the other hand, elastic interaction is due to the deflection of a primary electron upon contact with an atomic nucleus or electrons of comparable energy in the sample. The deflection of scattered electrons at angles greater than 90 degrees results in backscattered

electrons (BSE), which can be utilised for sample imaging. The generation of SEs and BSEs is illustrated in Fig. 2.5.

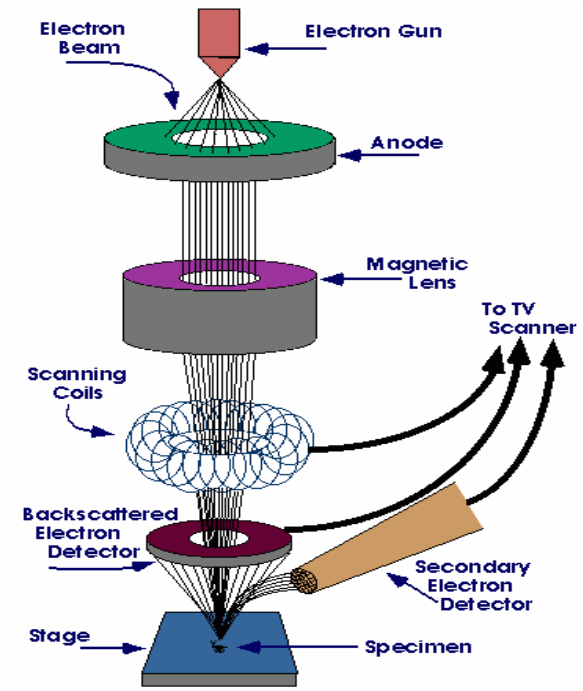

Figure 2.5. *Schematic of a scanning electron microscope.* [9]

The electron source is usually either a tungsten filament or a solid-state crystal. The tungsten electron filament is the most common type of electron source, mainly due to its low price point, high reliability, and suitability for low-magnification imaging and X-ray microanalysis.[10] It is shaped like an inverted "V" and heated resistively to radiate electrons. The SEM/EDX technique was used to characterise changes in the surface morphology of the anode electrode (Ti fibre felt coated with IrO_2) used in Chapter 3 and the membrane surface in Chapter 4.

2.2.2. X-ray photoelectron spectroscopy (XPS)

X-ray photoelectron spectroscopy measurements were employed to analyse the elemental composition and oxidation state of the catalyst surface, which is crucial for probing changes before and after water electrolysis. XPS can reveal how the catalyst evolves over time, providing insights into surface enrichment, oxide or hydroxide formation, and potential degradation pathways that affect electrode performance.[11]

An electron can be ejected when an atom or molecule absorbs an X-ray photon. The kinetic energy (KE) of the electron depends upon the photon energy (hv) and the binding energy (BE) of the electron (i.e., the energy required to remove the electron from the surface). Photoelectron spectroscopy is based upon a single-photon in-electron out process.[11] From many viewpoints, this underlying process is a much simpler phenomenon than the Auger process (a spontaneous process in which an atom with an electron vacancy in the innermost (K) shell readjusts itself to a more stable state by ejecting one or more electrons instead of radiating a single X-ray photon). The Einstein relation gives the energy of a photon of all types of electromagnetic radiation:

$$E = hv \qquad (2.4)$$

Where h is Planck's constant (6.62×10^{-34} J s) and v is the frequency (Hz) of the radiation. Photoelectron spectroscopy uses monochromatic radiation sources (i.e., photons of fixed energy).[12] The KE distribution of the emitted photoelectrons (i.e., the number of emitted photoelectrons as a function of their KE) can be measured using any appropriate electron energy analyser, and a photoelectron spectrum can thus be recorded. Fig. 2.6 shows the emission process in X-ray photoelectron spectroscopy analysis.

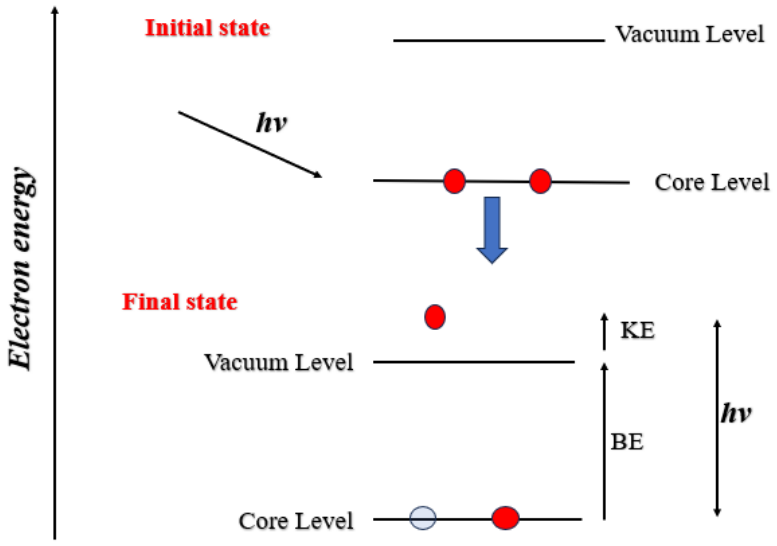

Figure 2.6. *The emission process in X-ray photoelectron spectroscopy analysis. The solid circles represent electrons, and the horizontal lines represent energy levels within the analysed material.*

The XPS technique is highly surface-specific because the excited photoelectrons emitted from a solid have a short range. The energies of the photoelectrons leaving the sample are determined using a concentric hemispherical analyser, which gives a spectrum with a series of photoelectron peaks.[12] The peaks' binding energy (BE) is characteristic of each element. The peak areas can be used to determine the composition of the material's surface. The chemical state of the emitting atom can slightly alter the shape of each peak and the BE. Hence, XPS can also provide information on chemical bonding. XPS is not sensitive to hydrogen or helium but can detect all other elements.[13] XPS is a surface-sensitive technique because only those electrons generated near the surface escape and are detected. Due to inelastic collisions within the sample's atomic structure, photoelectrons originating more than 20 -50 Å below the surface cannot escape with sufficient energy to be detected.[12,13] The XPS technique was used to characterise changes in the surface of the anode electrode (Ti felt coated with IrO_2) used in Chapter 3 of this thesis.

2.2.3. X-Ray Diffraction

X-ray diffraction (XRD) is used to determine the structural properties of the anode electrode (Ti felt) and to obtain information on crystal structure/phase, lattice parameters, crystallite size, single-crystal orientation, preferred orientation of polycrystals, defects, strains, and more.[15] This technique is suitable for thin films and nanomaterials. In the case of nanostructures, the change in lattice parameter relative to the bulk provides an indication of the nature of strain in the film. In XRD, a collimated, monochromatic X-ray beam is incident on the sample for diffraction to occur. Constructive interference occurs only for specific values of correlation to those planes, where the path difference is an integral multiple (n) of the wavelength. Based on this, Bragg's condition is given by Equation 2.5.

$$2dsin\theta = n\lambda \qquad (2.5)$$

Where λ is the wavelength of the incident X-ray, d is the inter-planar distance, θ is the scattering angle, and n is an integer called the order of diffraction. Fig.2.7 below helps in explaining Bragg's law.

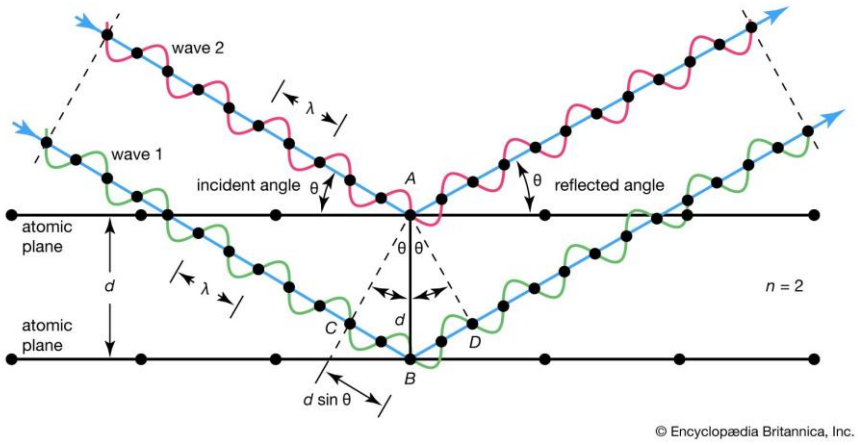

Figure 2.7. *Schematic representation of Bragg diffraction (https://www.britannica.com/science/Bragg-law#/media/1/76973/17859 Access Date January 30, 2025).*

When a crystal is irradiated with a beam of X-ray photons with a wavelength similar to the inter-atomic separation, it emits an X-ray beam with a wavelength equal to that of the incident beam, which then scatters. The scattered waves interfere to generate diffracted waves with higher intensities. Analysis of the spatial distribution of diffracted intensity allows characterisation of the material's structure.[16] In nanostructures, X-rays are diffracted by the oriented crystallites at a particular angle to satisfy Bragg's condition.

A typical X-ray diffraction experiment involves an X-ray source, the sample to be examined, and a detector to detect and record the diffracted X-rays.[16] Within this broad configuration, several variables control the different X-ray techniques.[16] The principle of the powder technique is as follows. Characteristically, a monochromatic beam of X-rays strikes a finely powdered sample with various lattice planes arranged in random orientations to facilitate diffraction in all directions. However, only the diffracted waves that satisfy Bragg's law give rise to pattern formation (Fig. 2.7). The diffracted beams can be detected either by surrounding the sample with a strip of photographic film (Debye-Scherrer and Guinier focusing methods) or through a movable detector, such as a Geiger counter, connected to a chart diffractometer recorder. The X-ray diffraction technique was used to characterise the anode electrode in Chapter 3 of this thesis.

2.2.4. Fourier Transform Infrared (FTIR) Spectroscopy

A Fourier transform spectrophotometer provides IR spectra much more rapidly than a traditional spectrophotometer. Fig. 2.8 schematically illustrates the main component of a simple FTIR spectrophotometer. The instrument produces a beam of IR irradiation from a glowing black-body source.[17]

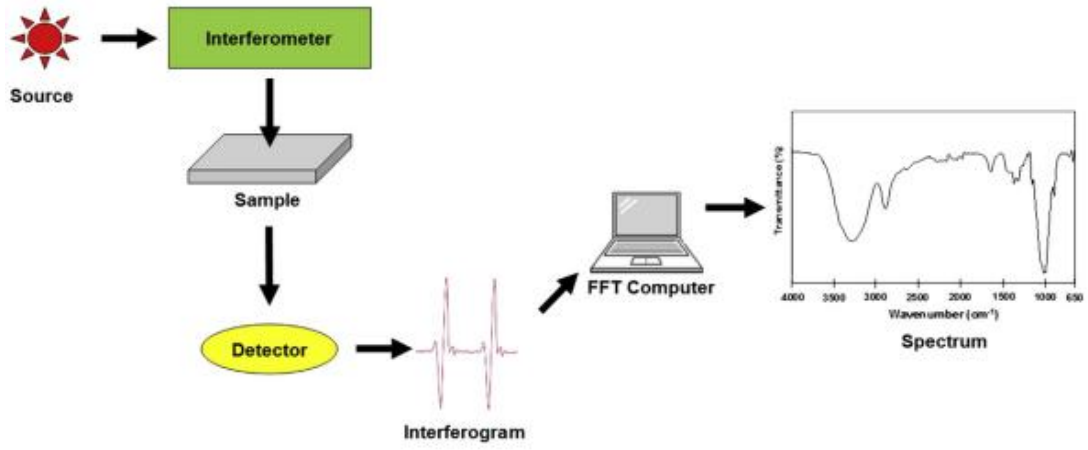

Figure 2.8. *A fundamental component of a Fourier transform infrared spectrometer.* [19]

Subsequently, the beam passes through the interferometer, where the spectral encoding occurs. The recombination of beams with different path lengths in the interferometer creates constructive and destructive interference, known as an interferogram.[19] The beam now enters the sample compartment, where the sample absorbs specific frequencies of energy that are uniquely characteristic of the sample, as determined from the interferogram. Then, the detector simultaneously measures the special interferogram signal in energy versus time for all frequencies. In the meantime, a beam is superimposed to provide a reference (background) for the instrument operation. Finally, the desired spectrum is obtained after the interferogram automatically subtracts the background spectrum from the sample spectrum using Fourier transformation computer software.[20]

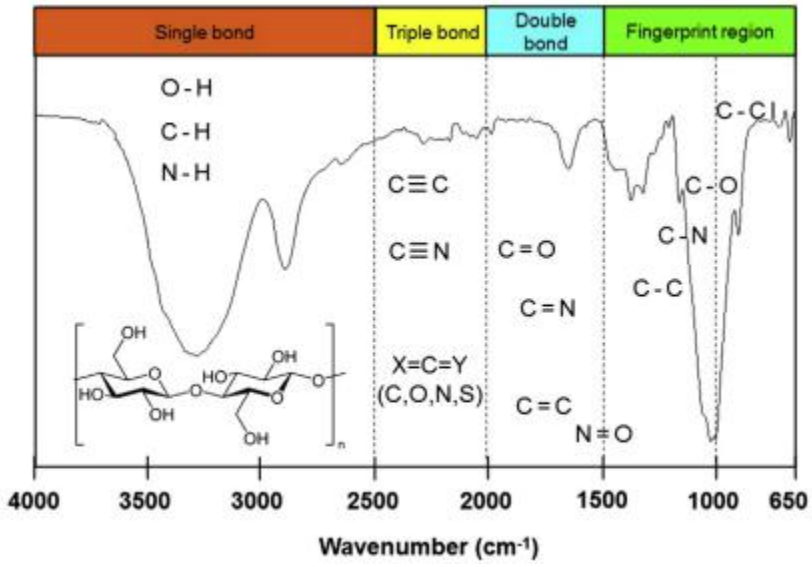

Figure 2.9. *Typical Fourier transform infrared spectra of a regenerated cellulose membrane with the various common types of bonds absorbing in the approximate regions indicated.* [20]

The IR spectrum obtained from the FTIR spectrometer lies in the mid-IR region between 4000 and 666 cm^{-1}. Transition energies corresponding to changes in vibrational energy state for many functional groups are in the mid-IR region (4000-400 cm^{-1}). Hence, the appearance of an absorption band in this region can be used to determine whether specific functional groups exist within the molecule. Typically, four regions indicative of different types of bonds can be analysed from the FTIR spectra. As shown in Fig. 2.9, a single bond (O-H, C-H, and N-H) is detectable at higher wavenumbers (2500-4000 cm^{-1}).[20] Also, the triple and double bonds are detectable in the middle wavenumber region 2000-2500 cm^{-1} and 1500-2000 cm^{-1}, respectively.[20,21] Additionally, the molecule's vibration as a whole gives rise to a complex pattern of vibrations in the low wavenumber region 650-1500 cm^{-1} that is characteristic of the molecule as a whole and hence can be used for identification. This technique was employed in Chapter 4 of this thesis to determine changes in the membrane's vibrational energy state.

2.2.5. Thermogravimetric Analysis (TGA)

Thermogravimetric analysis, also known as thermal gravimetric analysis (TGA), is an analytical method of thermal analysis in which the mass of a sample is measured over time as the temperature changes. This measurement provides information about physical phase transitions, absorption, desorption, and chemical phenomena, including chemisorption, thermal decomposition, and solid-gas reactions (e.g., oxidation or reduction).[22] The sample can undergo heating, cooling, or isothermal steps. The instrument used for thermogravimetry is a programmed precision balance for temperature rise, known as a thermobalance. The results are displayed by a plot of mass change (%) versus temperature or time. They are known as thermogravimetric (TG) curves (Fig. 2.10).

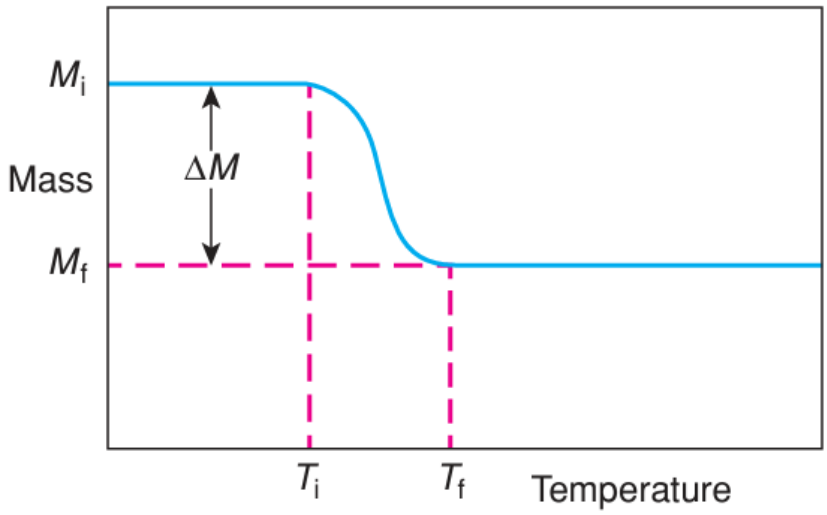

Figure 2.10. *Typical thermogravimetric measurement (relative weight change vs. temperature).*[22]

In thermogravimetric analysis, the sample is heated in a controlled environment (such as air, N_2, CO_2, He, or Ar) at a specified rate. The change in the material's mass is recorded as a function of temperature or time.[22,23] The temperature is increased at a constant rate for a known initial mass of the substance. The mass change is recorded as a function of temperature at different time intervals. This plot of mass change versus temperature is called a thermogravimetric curve or thermogram.[24] For classic thermogravimetry, a sample is usually put into a crucible made of inert material (e.g. platinum, alumina, gold, etc.) and placed on a

sensor within a furnace that can apply controlled atmospheres and temperatures. The thermogravimetric analysis technique was used to determine the mass loss in the dialysis membrane used in Chapter 4 of this thesis.

2.2.6. Atomic Force Microscopy

Atomic force microscopy (AFM) measures the repulsive or attractive force between a scanning probe and the sample surface. It can image the topography of any surface, whether it is an insulator, a conductor, or an organic material.[24] AFM instruments can be operated in several modes.[24] The most common are contact mode and tapping mode. In contact mode, a cantilever with a tip is placed in intimate contact with the sample surface.

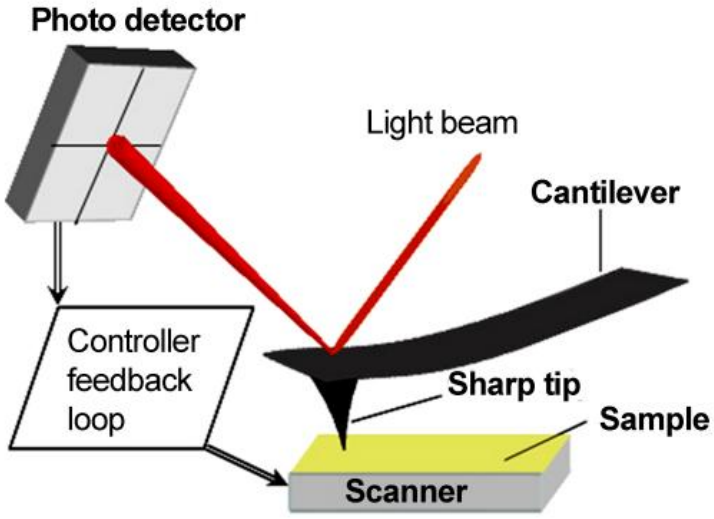

Figure 2.11. *Schematic of the basic principle of atomic force microscopy*[25]

As it is dragged across the surface, the contours of the surface are measured. However, measuring a static signal is prone to noise and drift. Therefore, tapping mode has been widely used during this work. In tapping mode, a stiff cantilever with a sharp tip is brought near the sample surface, as shown schematically in Fig. 2.11. During the scan, the force between the tip and the sample causes changes in the frequency and amplitude of the cantilever oscillation. The amplitude and frequency changes concerning the reference amplitude and frequency are used as feedback signals to obtain the topography of the sample's surface.[25] A feedback mechanism

is employed to maintain a constant tip-sample distance to avoid damaging the tip due to collisions with the surface.

Typically, cantilever deflection is measured by reflecting a laser beam from the cantilever's top surface onto a photodiode array. In chapter four of this thesis, the AFM is primarily used to measure the surface roughness of the dialysis membrane's surface morphology. The resolution of the AFM depends significantly on the tip shape. Monolithic silicon probes with cantilever resonant frequencies between 200 and 400 kHz and tip radii of less than 10 nm were typically used.[24,25] These probes were found to be adequate for imaging the catalyst layer on the membrane. The AFM technique was employed to determine the roughness of the dialysis membrane in Chapter 4 of this thesis.

2.2.7. Four-Point Probe System

The four-point probe method utilises a simple apparatus in which the four probes are placed equidistant in a straight line and pressed onto the film. The four-point probe is typically connected to a source meter, which can provide a particular current. The current (I) from a source meter passes through the two outer probes, and the voltage (V) across the two inner probes can be measured using a voltmeter (Fig. 2.12).[27] The four-point probe method is simple, low-cost, and reliable. Accurate resistivity measurements are critical for characterising materials, but it is not always easy to make such measurements across different material types, as they require different instrumentation and techniques. Electrical resistivity is a fundamental property that defines how well a material conducts current.[28] It is determined by measuring the resistance of a material sample and then factoring in its geometry. The three basic types of bulk materials, metal, insulator, and semiconductor, can be defined by their resistivity.

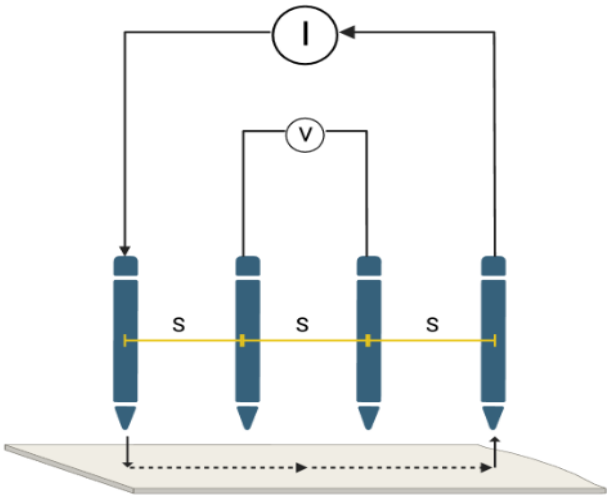

Figure 2.12. *Schematic diagram of a four-point probe measurement method* [28]

The system can measure sheet resistances from 100 MΩ/sq to 10 MΩ/sq, enabling the characterisation of a wide range of materials. If the sample thickness is provided, the average resistivity in ohms per meter (Ω·m) and conductivity in siemens per meter (S/m) will also be displayed. The four-point probe head utilises gold-plated, gentle, spring-loaded contacts with rounded tips. This results in a constant contact force of 60 grams, preventing the probes from piercing fragile thin films whilst still providing good electrical contact, [28]

In this study, the Lucas Pro4 4000 sheet and bulk resistivity measurement system, equipped with a Keithley 2450 source meter, was used to perform the 4-point probe measurement. It consisted of four equally spaced metal tips with a finite radius. A four-point probe measures the resistivity of semiconductor materials and thin films. Measuring with the Four-Point Probe System is simple, as it features a built-in source-measure unit. The membrane is placed on the sample stage centred under the four-point probe head, and the measure button is clicked. During measurement, the sample (membrane) is adjusted to allow readings from the four membrane sections to be taken. This is achieved by inserting the membrane's thickness into the system and applying a specified current. The voltage between the inner two probes will be measured, and the sheet resistance will be calculated from these values. A high-impedance current source supplies current through the outer two probes; a voltmeter measures the voltage across the inner two probes to determine the sample resistivity by carefully adjusting the tips to minimise sample damage during probing (see Figure 2.12). Knowing the membrane thickness allows us to calculate the conductivity. The four-point probe measurement technique

was primarily used in Chapter 4 of this work to measure the conductivity of the dialysis membrane. The dialysis membrane showed no electronic conductivity.

2.3. Gas Chromatography (GC)

Gas chromatography is a widely used analytical technique for separating and analysing gaseous and volatile compounds. In 1952, modern gas chromatography was invented by James and Martin.[31] Since the early 1950s, this technique has been used to separate amino acids. GC has many applications today because it is rapid and susceptible. Both qualitative and quantitative analyses can be done through GC. Even minute-quantity samples can be analysed by GC.[26] During the chromatography step, the sample is distributed between two phases: a stationary phase and a mobile phase. The mobile phase is a chemically inert gas, such as helium (He) or nitrogen (N_2). Gas chromatography is a unique form of chromatography that does not require a mobile phase to interact with the analyte. The stationary phase is either a solid adsorbent (gas-solid chromatography) or a liquid on an inert support (gas-liquid chromatography). The criteria required for the compounds to be analysed by GC are volatility and thermostability. [27] Generally, all the chromatographs consist of six basic components:

Sample injection: A sample port is necessary to introduce the sample at the head of the column. A calibrated micro syringe transfers a sample volume through a rubber septum and thus into the vaporisation chamber. Most separations require only a small fraction of the initial sample volume, and a sample splitter directs excess sample to waste. Commercial gas chromatographs use split and splitless injection modes when alternating between packed and capillary columns.[27] The vaporisation chamber is typically heated 50 °C above the lowest boiling point of the sample and subsequently mixed with the carrier gas to transport the sample into the column.

Carrier Gas: A carrier gas plays a vital role in GC. It should be inert, dry, and free of oxygen. Helium, Nitrogen, argon, and hydrogen are used as carrier gases depending on the desired performance and the detector being used. The carrier gas is supplied at high pressure and passed to the instrument rapidly and reproducibly.

Separation column: Open-tubular, capillary, and packed columns are used in GC. The first type of capillary column is a wall-coated open tubular (WCOT) column, and the second type

is a support-coated open tubular (SCOT) column. WCOT columns have a thin layer of stationary phase coating the column walls. In SCOT columns, the walls are first coated with a thin layer of adsorbent solid, such as diatomaceous earth, which consists of single-celled sea-plant skeletons.[27,28] The adsorbent solid is then treated with the liquid stationary phase. While SCOT columns can hold a greater volume of stationary phase than a WCOT column due to their greater sample capacity, WCOT columns still have greater column efficiencies. One of the most popular capillary column types is the coated fused-silica open-tubular column.

Column Ovens or Thermostat Chambers: The thermostat oven controls the column's temperature for precise work. It can be operated using isothermal programming or temperature programming. In isothermal programming, the column temperature is maintained constant throughout the separation. In the temperature programming method, the column temperature increases continuously or in steps as the separation progresses.

Detectors: The most common types of detectors used in GC are mass spectrometers, flame ionisation detectors (FID), electron capture detectors (ECD), thermal conductivity detectors (TCD), atomic emission detectors (AED), photoionisation detectors (PID), and chemiluminescence detectors. The detector at the end of the column gives a quantitative measurement of the mixture’s components as they elute in combination with the carrier gas.

Recorder system: The recorder system is a crucial component of GC instrumentation. It is responsible for recording signals from the detector, which provide information about the components of the sample as they elute from the column. These signals are processed and amplified by special electronic circuits to display in an understandable graphical format, representing several peaks of the sample’s constituents under analysis. Flow regulators and flow meters are also integral to the GC system, ensuring that the carrier gas is delivered with uniform pressure and flow rate, which is essential for obtaining accurate and reproducible results.

In GC, the vaporised sample is first injected into the chromatographic column. Then, the sample moves through the column under the flow of an inert gas, resulting in the separation of its components, which are recorded as a sequence of peaks as they exit the column (Fig. 2.13). The different elements of the sample are separated and eluted at characteristic times, known as retention times.[28]

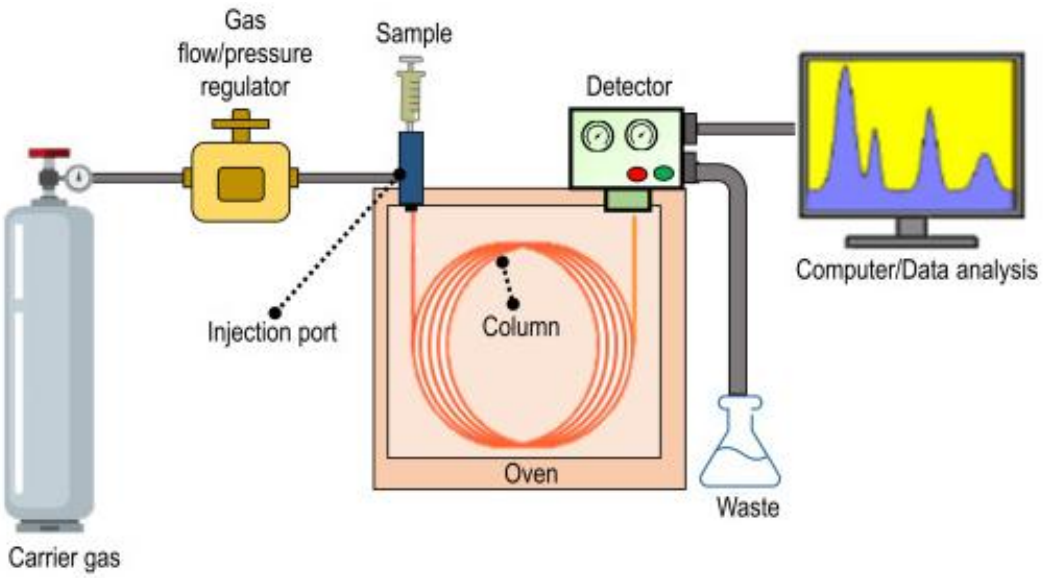

Figure 2.13. *Schematic Diagram of Gas Chromatography* [28]

The number of peaks determines the number of components present in the given sample; the identity of the components is determined by their characteristic retention times, and the area determines the quantity of the species defining the peaks in each sample. In chapters 3 and 4, the gas chromatography technique was extensively used to determine peak areas, enabling us to convert these peak areas into the number of moles produced to obtain the desired decoupling efficiency for hydrogen.

2.3.1. Gas chromatography Measurement

To determine the composition of gases in the anolyte and catholyte loops, 250 µL gas samples were collected from the headspace of the anolyte and catholyte reservoirs at regular intervals. Before collecting the gas from the headspaces, the cell producing hydrogen was purged with argon for 30 minutes at a flow rate of 250 mL/min. The collected gas samples were then analysed using a gas chromatography system (Agilent 8860) outfitted with a thermal conductivity detector. This system was configured with two Porapak Q columns and a molecular sieve 13X column. The initial oven temperature during analysis was set to 50 °C and maintained for 4 minutes, followed by a temperature ramp of 10 °C per minute until a final temperature of 120 °C was reached. The total analysis time was 11 minutes. Before analysis, the GC system was calibrated using certified hydrogen gas standards (1%, 2%, 3%, and 5% H_2 in Ar) supplied by CK Gas Products Limited (UK). Linear fits were then generated (Fig. 2.14), enabling the conversion of peak areas into the volume percentage of H_2 in the measured gas.

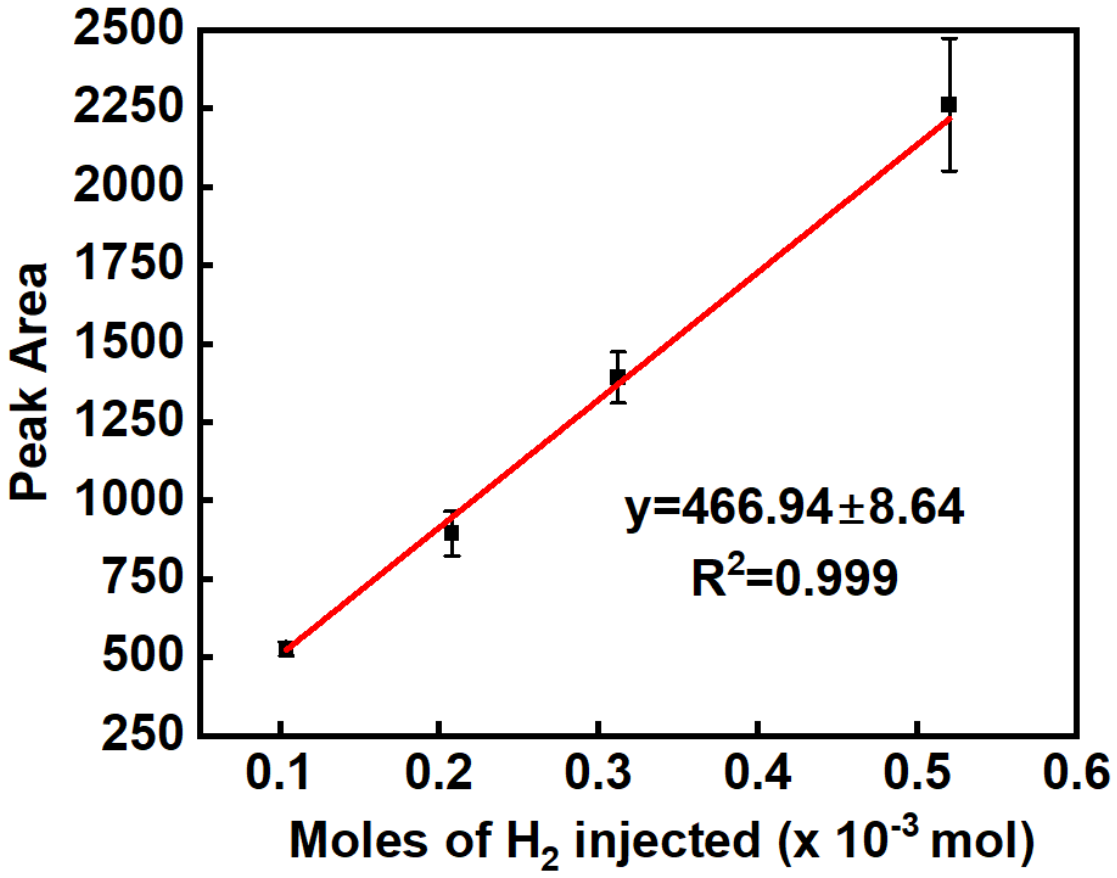

Figure 2.14. *The hydrogen calibration curve used in this work*

From this, the number of moles of hydrogen produced in a given experiment was then calculated by considering that the volume of 1 mole of an ideal gas at room temperature and pressure is 24 L. This, in turn, allowed the decoupling efficiency of the mediator reduction step to be calculated by the equation:

$$Decoupling\ efficiency\ (\%) = 1 - \frac{Number\ of\ moles\ H_2\ produced\ in\ oxygen\ generating\ cell}{Theoretical\ moles\ of\ H_2} \times 100$$

Where "theoretical moles of H_2" corresponds to the amount of hydrogen that one would typically expect to observe in a conventional ("coupled") electrolyser, based on the total charge passed.

2.4. Inductively coupled plasma-optical emission spectrometry (ICP-OES)

Inductively coupled plasma-optical emission spectrometry (ICP-OES) is a technique in which the composition of elements in (mostly water-dissolved) samples can be determined.[34] The method has been commercially available since 1974, and thanks to its reliability, multi-element options, and high throughput, it has become widely applied in routine research and more specific analysis purposes. [29,30]

A peristaltic pump conducts the solution to be analysed through a nebuliser in a spray chamber. The produced aerosol is fed into an argon plasma. Plasma is the fourth state of matter, next to the solid, liquid, and gaseous states. In the ICP-OES (Fig.2.15), the plasma is generated at the end of a quartz torch by a cooled induction coil through which a high-frequency alternating current flows. Consequently, an alternating magnetic field is induced, which accelerates electrons into a curved trajectory.

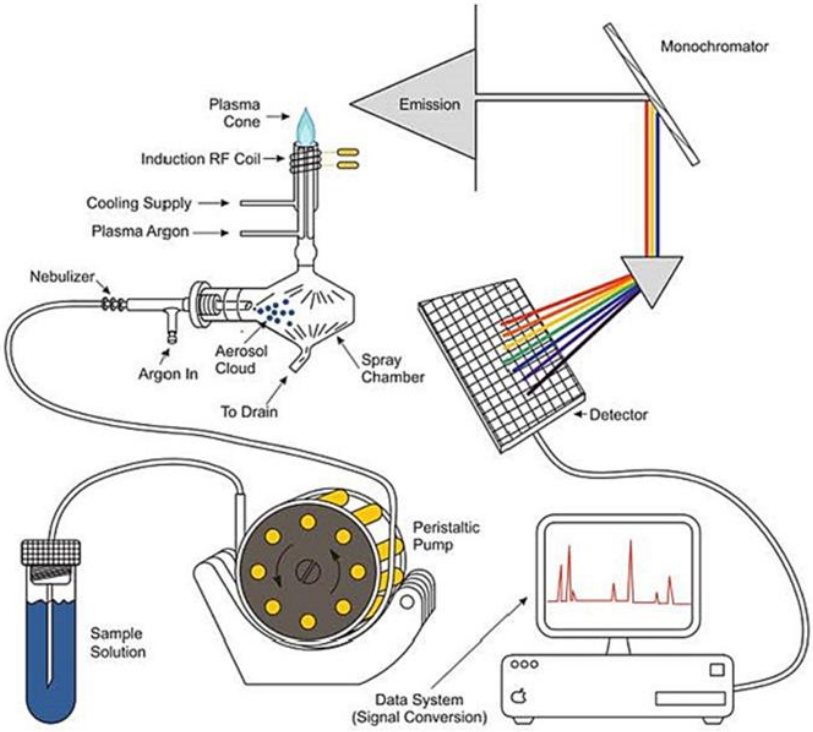

***Figure 2.15**. Typical components of an ICP-OES system* [30]

Due to the collision between an argon atom and an electron, ionisation occurs, giving rise to a stable plasma. The plasma is extremely hot, 6000-7000 K. In the induction zone, it can even reach 10000 K. In the torch, desolation, atomisation, and ionisation of the sample occur. Due to their thermal energy, electrons reach a higher "excited" state. When the electrons return to

ground level, energy is liberated as light (photons). Each element has its characteristic emission spectrum that is measured with a spectrometer. The light intensity at the specified wavelength is measured and calibrated to determine the concentration.[29,30] This technique was employed in Chapters 3 and 4 of this thesis to investigate the potential leaching of iridium into the anodic and cathodic streams.

2.5. Materials and Methods

2.5.1. Electrochemical cell design and construction

Fig. 2.16 illustrates the schematic of the flow cell system used in this work. The geometric area of the electrodes in both the oxygen- and hydrogen-producing cells was 13.7 cm^2 (3.7 × 3.7 cm). Silicotungstic acid ($H_4SiW_{12}O_{40}$), purchased from Merck, was used as the redox mediator at a concentration of 0.5 M in ultrapure water (resistivity, 15.2 MΩ.cm).

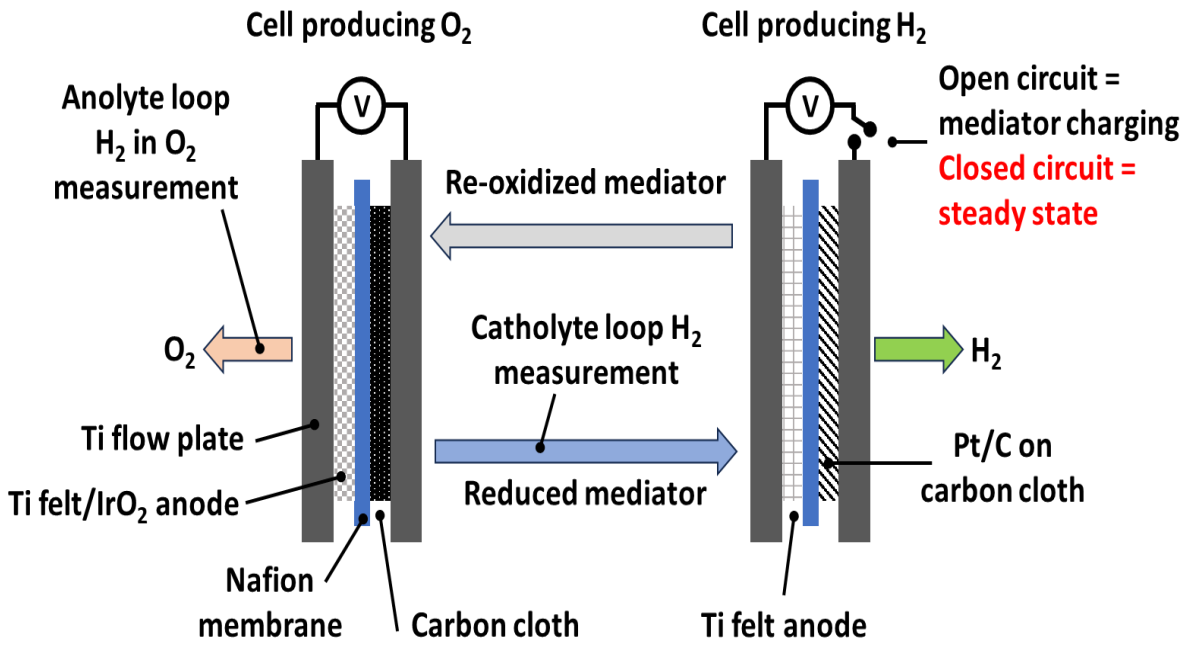

Figure 2.16. *A schematic of the flow cell system designed, constructed, and used in this study.*

2.5.2. Components of the flow cell

The flow cell components of the oxygen- and hydrogen-generating electrochemical system are illustrated: these components are used to assemble the oxygen-producing flow electrochemical cell employed in this study. Components are as listed below (these are described in the main text):

Table 2.1. The cell components of the oxygen- and hydrogen-generating electrochemical flow cells are shown in Fig. 4.1.

Components	Oxygen-Generating Cell	Hydrogen-Generating Cell
	Anode-side components	
1	Titanium plate	
2	Polytetrafluoroethylene insulating plate	
3	Polytetrafluoroethylene insulating gasket	
4	Ti serpentine flow plate	
5	Teflon gasket	
6	Ti fiber felt coated with IrO_2	Ti fibre felt (no catalyst)
7	Regenerated Dialysis Membrane	Nafion 117 membrane
	Cathode-side components	
8	Carbon cloth with a microporous layer	Carbon cloth with 0.5 mg Pt/C
9	Teflon gasket	
10	Ti serpentine flow plate	
11	Polytetrafluoroethylene insulating gasket	
12	Polytetrafluoroethylene insulating plate	
13	Titanium end plate	

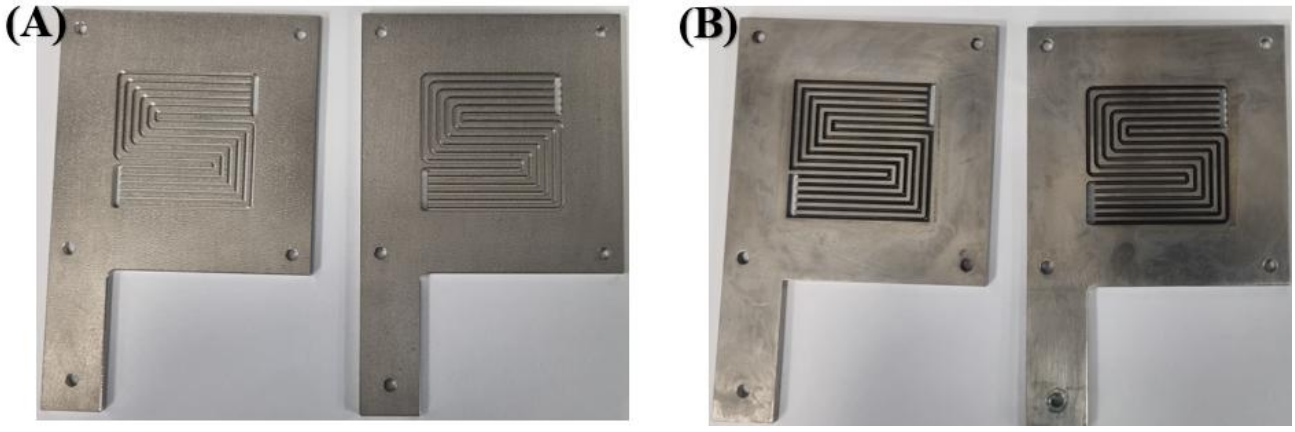

Figure 2.17. *Pictorial of Ti serpentine flow fields used in this study (a) before electrolysis, (b) after electrolysis (>180 days in contact with the redox mediator).*

The anode of this cell consisted of a 3 mm-thick titanium serpentine flow field (with flow channels 1 mm deep and 1 mm wide cut into it) and a titanium fiber felt (thickness: 0.3 mm) coated with 2.0 mg/cm^2 IrO_2 catalyst (supplied by Fuelcellstore) as the active electrode (see below for details of the electrode preparation). These elements were sealed using a 0.127 mm-thick Teflon gasket (supplied by Fuelcellstore). The cathode side also consisted of a titanium serpentine flow field (identical to that used at the anode) and carbon cloth with a microporous layer as the active electrode (Fuelcellstore). No catalyst was added to the cathode side. These elements were sealed using a 0.127 mm-thick Teflon gasket supplied by Fuelcellstore. A Nafion 117 membrane supplied by Ion Power separated the anode and cathode. The anode and cathode were compressed against the membrane through 10 mm-thick polytetrafluoroethylene (PTFE) insulating plates and 10 mm-thick titanium end plates. The bolts fastening the cells were tightened to a torque of 5 Nm. Before cell assembly, the serpentine flow plates were immersed in concentrated phosphoric acid (85%, Thermo Scientific) for 2 hours, then scrubbed with a sponge and rinsed with deionised water to ensure they were completely clean.

The construction of the second cell, which produces hydrogen, was similar to that of the oxygen-generating cell. Hence, the anode of this hydrogen-generating cell consisted of a 3 mm-thick titanium serpentine flow plate (identical to those used in the oxygen-generating cell), in combination with a Ti fibre felt (thickness: 0.3 mm) as the electrode. No catalyst was applied to this Ti fibre felt. The cathode side of this cell consisted of a 3 mm thick titanium serpentine flow plate, combined with a carbon cloth coated with 0.5 mg/cm^2 of Pt/C (Fuelcellstore) as the cathode catalyst and transport layer. These elements were sealed using 0.127 mm-thick Teflon gaskets supplied by Fuelcellstore. A Nafion 117 membrane supplied by Ion Power separated the anode and cathode. The anode and cathode were compressed against the membrane through 10 mm-thick PTFE insulating plates and 10 mm-thick titanium end plates, and the bolts fastening the cells were tightened to a torque of 5 Nm. The same materials and procedures were used in Chapter 4 of this thesis, with Nafion membrane replaced by a cellulose-regenerated dialysis membrane in the Oxygen-Generating Cell.

References

1. N. Elgrishi, K. J. Rountree, B. D. McCarthy, E. S. Rountree, T. T. Eisenhart, and J. L. Dempsey. *J. Chem. Educ*. 2018, 95, 197-206.
2. B.D. McCarthy, D. J. Martin, E. S. Rountree, A.C. Ullman, J.L. Dempsey, *Inorg. Chem*. 2014, 53, 8350-8361.
3. G. Inzelt, A. Lewenstam, and F. Scholz, *Handbook of Reference Electrodes*, Springer Berlin Heidelberg, Berlin, Heidelberg, 2013.
4. M. Chatenet, B. G. Pollet, D. R. Dekel, F. Dionigi, J. Deseure, P. Millet D. *Chem. Soc. Rev.* 2022, 51, 4583-4762.
5. R. A. Rozendala, V.M. Hubertus, J.W. Hamelersa, S.J. Euverinkb, J.N. Metzb, *Int. J. H. Ener,* 2026*,* 31, 1632-1640.
6. P. D. Cavaliere, A. Perrone, and A. Silvello. *Metals*, 2021, 11, 1816-1834.
7. M. E. Orazem and B. Ulgut. *J. Electrochem. Soc.* 2024, 171 040526
8. W. Choi, H.C. Shin, J.M. Kim, J.Y. Choi, W.S. Yoon. *J. Electrochem. Sci. Tech*., 2020, 11, 1-13.
9. C. Temiz (2022) Scanning Electron Microscopy. Electron Microscopy. IntechOpen. Available at: http://dx.doi.org/10.5772/intechopen.103956.
10. M. J. Park, D. H. Kim, K. Park, D. Y. Jang, and Dong-Chul Han. *J. of Mech Sci & Tech,* 2008, 22, 1734-1746.
11. G. Vereecke, and P. G. Rouxhet. *Surf. Int. Anal*. 1998, 26, 490-497.
12. F. A. Stevie, and C. L. Donley. *J. Vac. Sci. Technol*, 2020, 38, 1-21.
13. C. D. Wagner, D. E. Passoja, H. F. Hillery, T. G. Kinisky, H. A. Six, W. T. Jansen, and J. A. Taylor. *J. Vac. Sci. Technol,* 1982, 21, 933-944.
14. R. Guinebretière, A. Boulle, O. Masson, and A. Dauger. *Pow. Diff,* 2005, 20, 294-307.
15. W. W. Andualem, *W. J. Pharm. Res*, 2020, 9, 29-51.
16. R. Guinebretière. X-Ray Diffraction by Polycrystalline Materials, 2013, John Wiley.
17. S.A. Khan, S.B. Khan, L.U. Khan, A. Farooq, K. Akhtar, A.M. Asiri. *Handbook of Materials Characterisation,* 2018, 317-344.
18. V. K. Undavalli, C. Ling, B. Khandelwal. *Avi. Fuels*, 2021, 113-132.
19. M. A. Mohamed, J. Jaafar, A. F. Ismail, M.H.D. Othman, M.A. Rahman. *Mem. Char*, 2017, 3-29.
20. N. Sousa, M.J. Moreira, C. Saraiva, J.M.M.M. De Almeida., *Foods*, 2018, 55-64.

21. B. Patrizi, M. Siciliani de Cumis, S. Viciani, F. D'Amato. *Int. J. Mol. Sci.* 2019, 20, 2671-2690.
22. S. Loganathan, R. B. Valapa, R. Mishra, G. Pugazhenthi, S. Thomas. *Ther. And Rheo. Measure*, 2017, 67-108.
23. N. Saadatkhah, A. Carillo Garcia, S. Ackermann, P. Leclerc, M. Latifi, S. Samih, G.S. Patience. *Can. J. Chem. Eng.* 2020*,* 98*,* 34-43.
24. G. Pletikapić, and N. Ivošević DeNardis. *Nat. Hazards Earth Syst. Sci*. 2017, 17, 31-44.
25. Y. Sugimoto, P. Pou, M. Abe, P. Jelinek, R. Pérez, S. Morita, O .Custance., *Nature*, 2007, 446, 64-68.
26. T.R. Arruda, B.R.C.L. Junior, C.S. Marques, P.C. Bernardes, C.G. Magalhães, P.F. Pinheiro. *Green. Prod. Food Safety*, 2023, 29-79.
27. S.J. Lehotay, and J. Hajšlová. *Trends in Analy. Chem*, 2002, 21, 687-699.
28. S. Thurnhofer, and W, Vetter. *J. Agric. Food Chem*. 2005, 53, 8896−8903.
29. C. Douvris, T.Vaughan, D. Bussan, G. Bartzas, R. Thomas. *Sci. Total Ent,* 2023, 905, 16724-16741.
30. A. Harris, S.J. Xanthos, J.K. Galiotos, C. Douvris. *J. of Microchem*, 2023, 142, 140-143.

CHAPTER THREE
DECOUPLED WATER ELECTROLYSIS AT HIGH CURRENT DENSITIES USING A SOLUTION-PHASE REDOX MEDIATOR

This chapter contains expanded and updated sections from the following publication ''Decoupled water Electrolysis at high current densities using a solution-phase redox mediator'' Obeten Mbang Eze, Zeliha Ertekin, and Mark D. Symes.

***ACS Energy Fuels*, 2025, 39, 7129−7136.**

https://doi.org/10.1021/acs.energyfuels.5c00092

Acknowledgements and Declarations

The content of this chapter was initially developed in collaboration with my supervisors, Prof. Mark Symes and Dr Zeliha Ertekin. I thank both for their valuable contributions to the original manuscript. Any sections not authored by me in the original script have been either omitted or entirely rewritten, ensuring that the work presented here is solely my own.

3.1. Introduction

The research work presented in this chapter employed a decoupled electrolysis system utilising silicotungstic acid as the redox mediator in a flow cell assembled from two electrochemical cells (Fig. 2.15): one for oxygen production and mediator reduction, and the other for hydrogen production and mediator re-oxidation. In the oxygen-producing cell, IrO_2 was sprayed directly onto the gas diffusion layer (Ti fibre felt) as the anode catalyst, while in the hydrogen-producing cell, 0.5 mg/cm^2 Pt/C on carbon cloth was used as the cathode catalyst. Hence, neither cell used a catalyst-coated membrane; instead, both used a more straightforward arrangement of an undecorated membrane and catalysts deposited on the gas diffusion layers, which were in contact with the membrane. In this work, we significantly expanded the range of current densities over which decoupling is demonstrated, from 0.05 A/cm^2 to 1.35 A/cm^2, the latter of which exceeds both the previous highest current density explored for this mediator (0.5 A/cm^2)[15] and the current densities at which commercial alkaline electrolysers operate. In conventional water electrolysis, the water oxidation and reduction reactions are tightly coupled in terms of time, rate and space, as they occur simultaneously at the two electrodes (the anode and cathode) inside the same cell. This coupling introduces operational challenges, such as H_2/O_2 crossover.[1-6] This is especially problematic when operating under low and/or fluctuating power inputs (as often characterised by renewable power).[6,7] Such crossover of hydrogen into the oxygen stream accelerates the degradation of expensive components in the electrolyser.[7] If unchecked, it can lead to the production of explosive mixtures of hydrogen and oxygen.[8] Thus, developing more efficient and robust electrolysis systems that are inherently compatible with renewable power sources is vital if large-scale green H_2 production is to become a reality. In this work, the oxygen-generating step of water splitting occurred electrochemically, whilst the hydrogen generation step occurred in a completely separate reactor external to the electrochemical cell ("ex-cell") at rates that were largely independent of the rate of the oxygen generation step. Gas analysis showed that essentially complete decoupling of the oxygen evolution and hydrogen evolution reactions could be achieved with rates of gas crossover that were well below the lower explosion limit for hydrogen in oxygen.

3.2. Electrode preparation

3.2.1. The anode catalyst ink preparation

The anode catalyst preparation involves two main steps:

Step 1: Micro-porous layer (MPL) Ink preparation

In the first step, the Ti micro porous layer is formed, and second, the coating is done with an IrO_2 (99.9%, Sigma-Aldrich) catalyst. In the first step, the Ti fibre felt was coated using Ti microparticles (5 μm, US Nanomaterials Research, Inc.) by weighing out 2.5 g of the Ti particles (≈ 52 mmol) under an inert nitrogen atmosphere into a suitably sized vial in a glovebox (to prevent combustion in air). The vial was sealed with a septum and removed from the glove box. 2.5 mL of Nafion solution (5 wt% in lower aliphatic alcohols and water, containing 15-20% water, Sigma Aldrich, CAS: 31175-20-9) was added to the vial containing the Ti particles using a syringe. The septum was removed, and 10 mL of isopropanol was pipetted into the suspension. The vial containing the suspension was then placed in an ultrasonication bath (Fisher Scientific FB 15050) at 37 kHz for 15 min, after which another 10 mL of ethylene glycol (Alfa Aeasar, 99%) was added to the solution. Then, ultrasonication was continued for a further hour. After this time, the vial containing the suspension was moved to a refrigerator and cooled to 4 °C. Once at 4 °C, spraying was undertaken. To this end, the gas diffusion layer (13.7 cm^2 Ti fibre felt) was rinsed with water, ultrasonicated in acetone for 5 minutes, then dried. The Ti felt was then sprayed using an AB-182 (Everything Airbrush) double-action suction airbrush (0.5 mm), with a 22 ml detachable glass jar bottle attached to the air compressor (Royal Max TC-80T single-piston compressor). The spraying support (Fig. 3.1) was made from 5 mm foamboard.

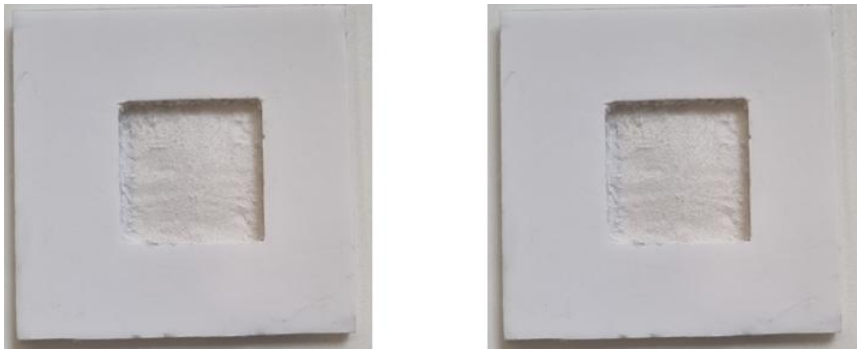

Figure 3.1. *Foamboard structure used to support the Ti felt electrode during the air-spraying of the IrO_2 catalyst onto the Ti felt.*

The gas diffusion layer was tightly fitted into the supporting foamboard and held perpendicular to the spraying platform at a comfortable height in the fume hood. After spraying, it was dried in an oven at 100 °C for 5 minutes and then weighed. Fig. 3.2 illustrates the steps involved in the air-spraying process.

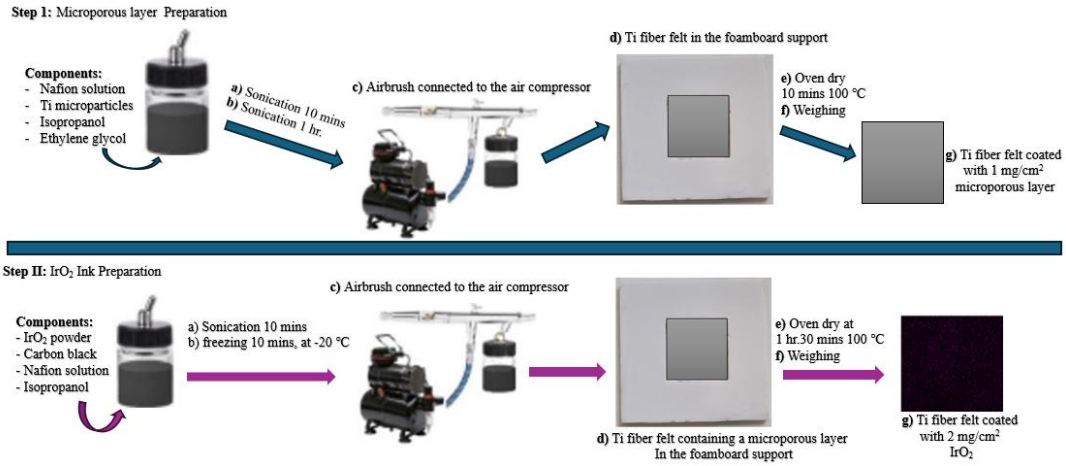

Figure 3.2. *Showing the air-spraying steps during anode catalyst preparation.*

Step ll. In the second step, the IrO_2 catalyst ink was prepared by mixing 63 mg of carbon black (acetylene, 50% compressed, 99.9+%, Thermo Fisher Scientific), 55 µL of Nafion solution, and 205 mg of IrO_2 in a 22 mL airbrush paint bottle. Then, 4.5 mL of isopropanol was added, and the mixture was gently stirred with a glass pipette to disperse any clumps. The bottle was sealed with tape to close all openings, then covered with aluminium foil and parafilm. It was then sonicated in an ultrasonic bath with ice for about 3 hours. Ice was added every 10–15 minutes to minimise temperature increases during sonication. After 1.5 hours, the bottle was removed, unsealed, and mixed with a pipette tip to break up clumps. It was then resealed and returned to the ultrasonic bath for another 1.5 hours. After sonication was complete, the ink was stirred and stored in the refrigerator at 4 °C until it was required for spraying. Once the temperature reached 4 °C, spraying was undertaken. Immediately before spraying, the prepared and chilled ink was removed from the refrigerator, ultrasonicated at 37 kHz for 30 minutes on ice, shaken vigorously, and then returned to the fridge for an additional 10–15 minutes. The ink was then loaded into the airbrush. One side of the gas diffusion layer was then sprayed inside the fume hood (at a working distance of 10 -15 cm), ensuring that the gas diffusion layer was coated evenly by spraying, starting from the perimeter and moving towards the centre at a pressure of 1.5 bar. After spraying, the gas diffusion layer was removed from the support and

put in an oven in air at 100 °C for 5 min. After this time, the felt was weighed and further rounds of spraying were undertaken as necessary until the desired loading mass (2.0 mg/cm^2 of IrO_2) was obtained using the relation:

$$Loading\ mass\ (mg) = \frac{Wt.of\ GDL\ with\ catalyst - Wt.of\ GDL\ with\ MPL}{13.7} \times 65\%$$

3.2.2. Standard Procedure for Obtaining the Foamboard Support Structure Used to Support the Ti Felt Electrode before Air Spraying

The standard operating procedure for obtaining the foamboard support (see Fig. 3.1) before air-spraying a Ti felt gas diffusion includes the following:

a) Making the support that holds the gas diffusion layer: First, cut a 10 cm x 10 cm square of the foam board
b) Using a scalpel, cut a 3.7 cm x 3.7 cm square at the centre of the foam board, piercing all the way through
c) Remove the 3.7 cm x 3.7 cm square opening
d) Pull out the cut foam from the square ring, leaving a surface of a lip for the gas diffusion layer to rest against.
e) Ensure that the 13.7 cm^2 Ti felt (GDL) has been cut and cleaned by rinsing with ultra-pure water, ultrasonicating for 5 minutes, soaking in water, repeating with acetone, and drying the gas diffusion layer.
f) Dry the gas diffusion layer by air or in an oven using a dish for 2 minutes at 100 °C
g) Place the gas diffusion layer into the support (as shown in Fig. 3.2). It should be fitted and tight so that it does not fall off when held perpendicular to the spraying platform.
h) Ensure that it cools down to room temperature before spraying
i) Ensure to note any distinguishing marks that may be on the gas diffusion layer for remembering which side has been sprayed with the microporous layer (If a microporous layer is involved)

It is advisable to have two separate airbrushes, one for spraying the microporous layer and one for spraying the catalyst ink. Furthermore, remember to place the foam board containing the gas diffusion layer in a comfortable position (height) in the fume hood.

3.3. Electrochemical Measurements

3.3.1. Cyclic Voltammetry

For the cyclic voltammetry tests, a conventional three-electrode system was employed, consisting of a glassy carbon button working electrode (area = 0.071 cm^2; Basi Research Products), a platinum wire as the counter electrode, and an Ag/AgCl (3 M NaCl) reference electrode. The electrolyte was 0.5 M $H_4SiW_{12}O_{40}$ in ultrapure water. A single-chamber cell was used. The cyclic voltammetry measurements were performed using a Gamry potentiostat, version 7.4.8, at a scan rate of 10 mV/s. The potentials reported in this work were converted to the reversible hydrogen electrode (RHE) scale using the following equation: $E_{RHE} = E_{Ag/AgCl} + E^0_{Ag/AgCl} + 0.059$ pH, where $E_{Ag/AgCl}$ is the observed potential during the experiments using a Ag/AgCl (3 M NaCl) reference electrode and $E^0_{Ag/AgCl}$ is the potential of Ag/AgCl (0.1976 V) versus the normal hydrogen electrode. Control experiments were performed with 1 M sulphuric acid (Fisher Scientific, > = 95 %, with S.G. 1.83) using a BioLogic SP-150 potentiostat coupled to a BioLogic VMP-3B 20 A/20 V booster.

3.3.2. Controlled current electrolysis

Controlled current electrolysis was performed using a BioLogic SP-150 potentiostat coupled to a BioLogic VMP-3B 20 A/20 V booster. Before each experiment, the mediator solution was bubbled with argon for 45 min to remove any oxygen from the system. The Biologic SP-150 was used to apply a fixed current to the cell, which generated oxygen. The second cell responsible for making hydrogen was driven by an Admiral SquidstatPlus potentiostat to supply the current. The same current was applied across both cells during the working period to maintain the system in a steady state.

3.4. Physicochemical Measurements

X-ray photoelectron spectroscopy was performed using a Kratos Axis Supra+ instrument, equipped with a monochromated Al Kα line (1486.6 eV, 30 mA) as the X-ray source. Data analysis was performed using ESCApe software, which employed Gaussian-Lorentzian fitting for each component peak. Scanning electron microscopy (SEM) and X-ray diffraction (XRD) were employed to examine the surface morphology of the prepared IrO_2/Ti electrodes and to assess the crystallinity of the IrO_2 layer. The prepared IrO_2 electrodes were characterised using a Rigaku MiniFlex instrument, employing Cu Kα radiation.

The scanning diffraction angle 2θ ranged from 10 - 90° at a speed of 5 minutes per data point and a scanning rate of 1° min^{-1}. SEM (TESCAN CLARA) equipped with EDX (Oxford Instruments Ultim Max) was used to probe the surface morphology and phase composition, confirming the loading mass on the electrode surface. The possible presence of metallic residuals in both the anolyte and catholyte streams following controlled current electrolysis was probed by sampling the electrolyte reservoirs and then analysing these samples using inductively coupled plasma optical emission spectroscopy (ICP-OES, Agilent 5900). The residuals were diluted in 2% HNO_3 before analysis.

3.5. Results and Discussion

Fig. 3.3 shows a cyclic voltammetry study of the redox mediator (0.5 M $H_4SiW_{12}O_{40}$) to determine the position of its redox waves. The first two redox peaks in Fig. 3.6a are labelled and correspond to one-electron processes.[17] The reduction of $H_4SiW_{12}O_{40}$ to $H_5SiW_{12}O_{40}$ has a midpoint potential of around 0 V vs. RHE, whereas the reduction of $H_5SiW_{12}O_{40}$ to $H_6SiW_{12}O_{40}$ has a midpoint potential of around −0.3 V *vs.* RHE at pH 0.5. The pH was measured using a pH meter. The ratio of the peak currents for the oxidation and reduction processes is unity in both cases, suggesting that both processes are reversible electron-transfer reactions. Similarly, expanded reductive scans were performed to measure and compare the redox activity of the redox mediator.

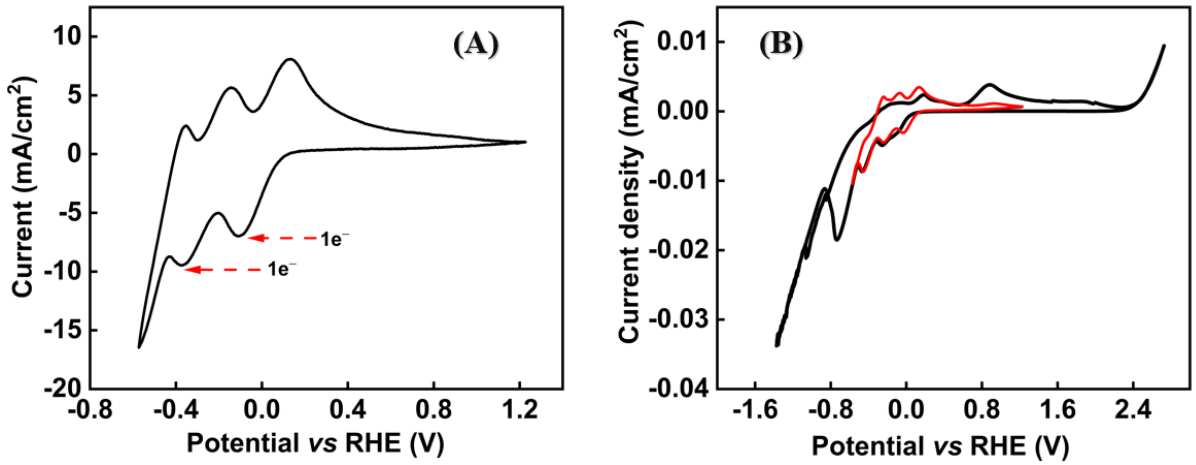

Figure 3.3. *Cyclic voltammogram (a) and (b) Expanded Reductive voltammogram (black) and Restricted potential window (Red) of 0.5 M Silicotungstic acid (pH 0.5) in a conventional three-electrode system at a scan rate of 10 mV/s on a glassy carbon working electrode (0.071 cm^2), at room temperature (~25 ºC).*

Therefore, the reduction of $H_4SiW_{12}O_{40}$ to the two-electron-reduced form, $H_6SiW_{12}O_{40}$ (Fig. 3 .3a), takes place in two steps, via the formation of the singly reduced species $H_5SiW_{12}O_{40}$. In previous work, Rausch *et al.*[14] Showed that the introduction of suitable catalysts (e.g., Pt/C) to $H_6SiW_{12}O_{40}$ results in spontaneous hydrogen generation, enabling complete conversion to $H_5SiW_{12}O_{40}$, and converting a further 30% of the $H_5SiW_{12}O_{40}$ onwards to the fully oxidised $H_4SiW_{12}O_{40}$ form. Meanwhile, in the presence of Pt/C and hydrogen gas, $H_5SiW_{12}O_{40}$ and the fully oxidised $H_4SiW_{12}O_{40}$ form are in equilibrium.[14]

Significantly, the redox waves for both the $H_5SiW_{12}O_{40}/H_6SiW_{12}O_{40}$ couple and the $H_4SiW_{12}O_{40}/H_5SiW_{12}O_{40}$ couple lie between the hydrogen evolution and oxygen evolution potentials under these conditions on a glassy carbon electrode (Red line in Fig. 3.3b), enabling the mediator to be fully reduced by two electrons without any competing hydrogen evolution.

3.5.1. Controlled current decoupled water electrolysis

Next, a two-cell flow system (as shown in Fig. 2.15) was assembled, with 100 mL of an aqueous 0.5 M fully oxidised silicotungstic acid ($H_4SiW_{12}O_{40}$) solution in both the anolyte and catholyte loops. The flow rate of the anolyte solution through the anode side of the oxygen-generating cell was 40 mL/min, while the flow rate of the catholyte solution through the cathode side was set to 250 mL/min. The reservoir temperatures for both the anolyte and catholyte were maintained using oil baths, ensuring that the feed temperatures entering the cell were 40 °C. Various current densities were applied across this oxygen-generating cell (see Table 1) whilst the circuit on the second (hydrogen-producing) cell was open. The effect of this was to progressively charge the mediator up to a state of "70% charge" (corresponding to the equilibrium position between the $H_5SiW_{12}O_{40}$ and $H_4SiW_{12}O_{40}$ forms when in contact with a Pt/C catalyst at 1 bar, as determined by Rausch *et al.*[14] *i.e.* the minimum level of reduction at which one could expect spontaneous hydrogen evolution upon exposure to Pt/C at 1 bar. Given that there was 100 ml of 0.5 M mediator in the catholyte loop, this required the passage of 3370 C across the oxygen-generating cell. Fig. 3.4a illustrates the charging process for a 0.5 M $H_4SiW_{12}O_{40}$ solution at a current density of 250 mA/cm².

Once the system reached 70% state of charge, it was placed into steady state by closing the circuit to the hydrogen-producing cell and setting the current across that cell to match that across the oxygen-generation cell. In this way, it was possible to reduce the mediator in the oxygen-generation cell and reoxidise it in the hydrogen-producing cell without changing the global state of charge of the mediator solution. Table 3.1 shows the voltages required to maintain the system in a steady state at various current densities. In all cases, these cell voltages are averaged for approximately 5 hours. In all cases, the mediator solution in the catholyte loop had previously been charged to 70% state of charge by applying a current density of 100 mA/cm^2 before placing the cell into steady state. Fig. 3.7b shows an example voltage-time curve (at a steady-state current density of 250 mA/cm^2), with 53,225 C being passed after the system reaches steady state. Given that the charge required to fully convert this amount of the $H_4SiW_{12}O_{40}$ form of the mediator to the $H_5SiW_{12}O_{40}$ form is 4824 C, 53,225 C corresponds to

over 11 turnovers of the mediator, suggesting that the mediator is capable of cycling between the $H_5SiW_{12}O_{40}$ and $H_4SiW_{12}O_{40}$ forms multiple times without noticeable loss of performance on this timescale.

Table 3.1. Average cell voltages across the OER cell (over approximately 5 hours) at different steady-state current densities with a silicotungstic acid concentration of 0.5 M, at 40 °C, with an anolyte flow rate of 40 ml min^{-1} and a catholyte flow rate of 250 ml min^{-1}. In all cases, the silicotungstic acid mediator solution was charged to 70% state of charge by passing 3370 C at a current density of 100 mA/cm^2 before placing the cell into steady state.

Steady state current density (A/cm²)	0.05	0.1	0.25	0.5	1.0	1.2	1.35
Initial state of charge (%)	70	70	70	70	70	70	70
Final state of charge (%)	70	70	70	70	70	70	70
Total charge passed in steady state (C)	11363	22646	53225	107543	212672	255450	287385
OER Cell Voltage (V)	2.16	2.25	2.43	2.72	2.94	3.14	3.44
Decoupling Efficiency (%)	100	100	99.9	99.9	99.9	99.9	99.9

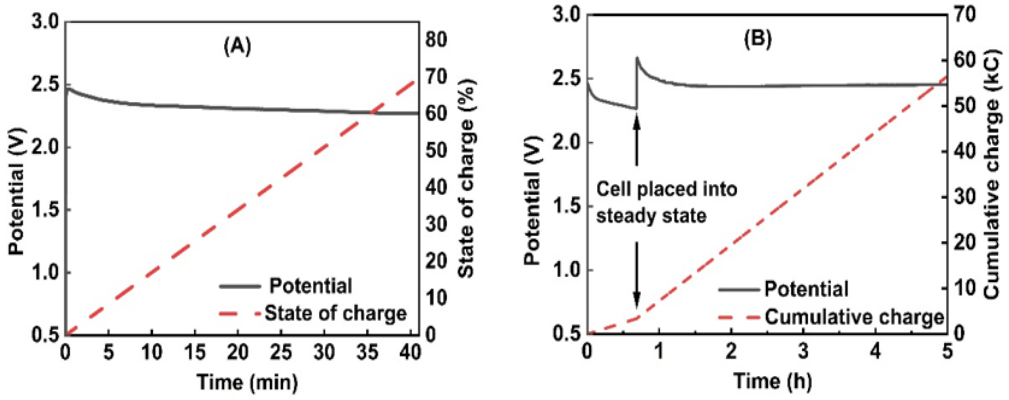

Figure 3.4. (a) *The voltage-time curve shows the charging of a 0.5 M $H_4SiW_{12}O_{40}$ solution to a 70% state of charge at a current density of 100 mA/cm^2 in the flow system.* ***(b)*** *Steady-state operation curves (at 250 mA/cm^2) for 0.5 M silicotungstic acid in the flow system. The silicotungstic acid was first charged to 70% state of charge at a current density of 100 mA/cm^2 (see also panel A), after which the current density was changed to 250 mA/cm^2 at approximately 41 minutes.*

A current potential curve (Fig. 3.5) from the primary cell (OER) was obtained for the flow cell shown in Fig. 2.15. This curve was obtained by stepping the current (after the charging period) at 41-minute intervals.

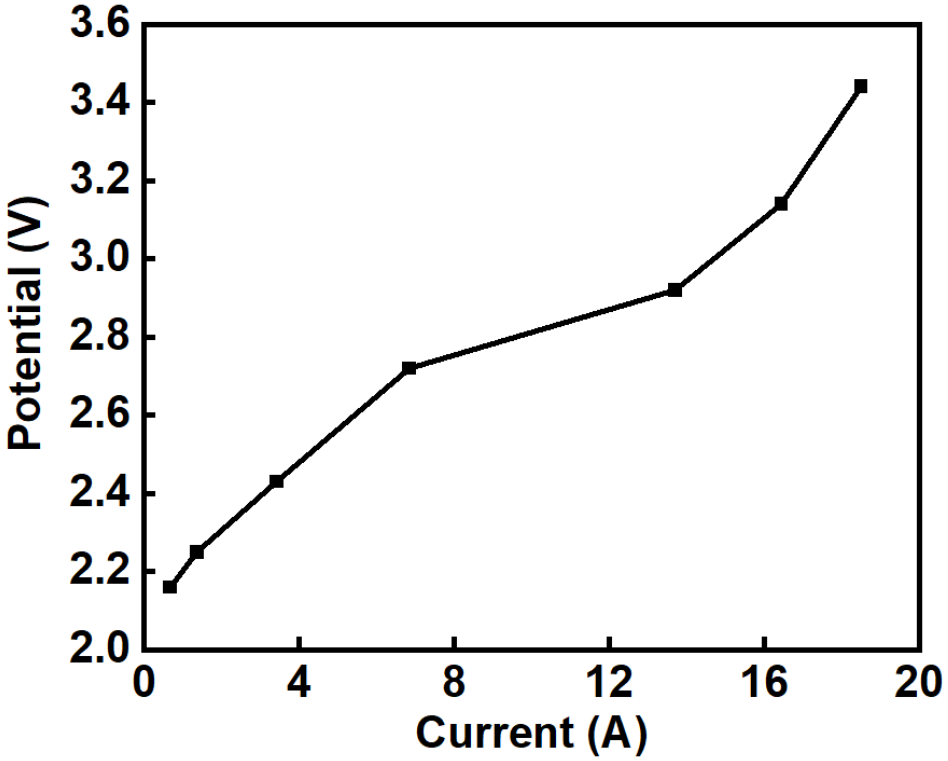

Figure 3.5. *Current-potential (OER cell) curve for the flow cell system used in this work with a Nafion membrane.*

The average cell voltages for the OER were then measured over 5 h for each applied current. The performance of the flow cell system was comparable to that of conventional proton exchange membrane electrolysers of similar construction and operating at similar temperatures, as reported in the literature.[14,15] As expected, the cell voltage increases with increasing current.

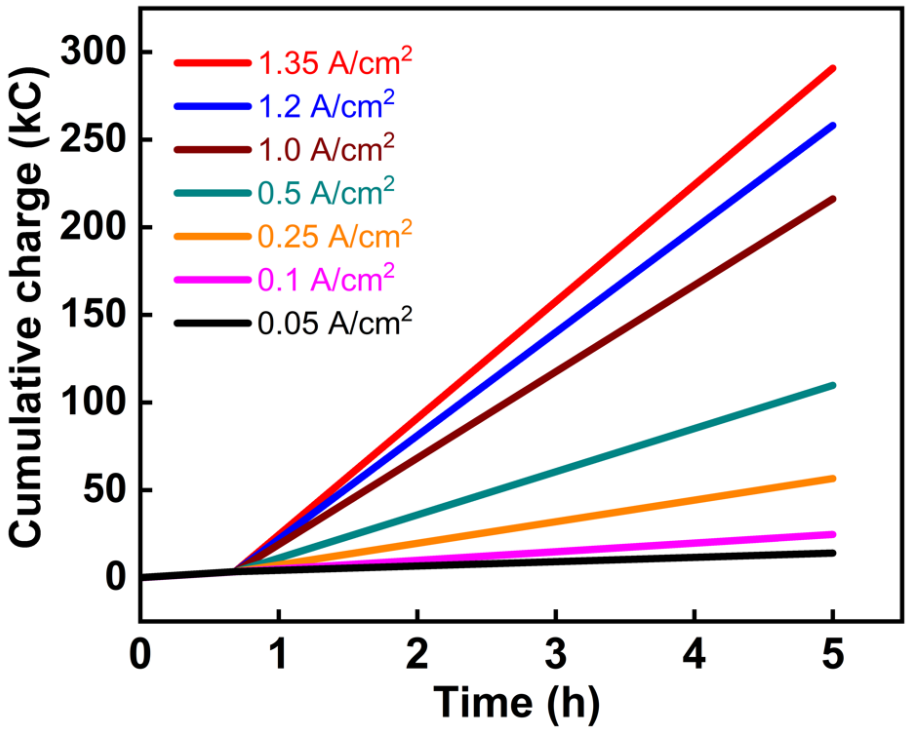

Figure 3.6. *Charge-time curves at different steady state current densities for 0.5 M silicotungstic acid at 40 °C and a catholyte flow rate of 250 mL* min^{-1}*. In all cases, the silicotungstic acid mediator solution was charged to 70% state of charge by passing 3370 C at a current density of 100 mA/*cm^2 *before placing the cell into steady state.*

Fig. 3.6 shows Charge-time curves for the range of steady-state current densities given in Table 3.1. During these steady-state experiments, regular gas measurements were taken to determine the extent of hydrogen gas evolution at the cathode of the oxygen-producing cell and the degree to which any hydrogen produced crossed over into the oxygen stream in the anolyte loop. Table 3.2 shows the percentage (%) of hydrogen detected in the anolyte and catholyte loops as a function of current density, as well as the decoupling efficiency for mediator reduction calculated based on the amount of hydrogen observed in the catholyte loop head space as shown in Fig. 3.7. Hydrogen has a retention time of 1.8 minutes, oxygen 7.9 minutes, and nitrogen 8.7 minutes. The nitrogen and some of the oxygen originate from air leaks within the GC apparatus; in panel b, almost all the oxygen present originates from the air. It was assumed that hydrogen remained fully contained within the headspace throughout the measurement.

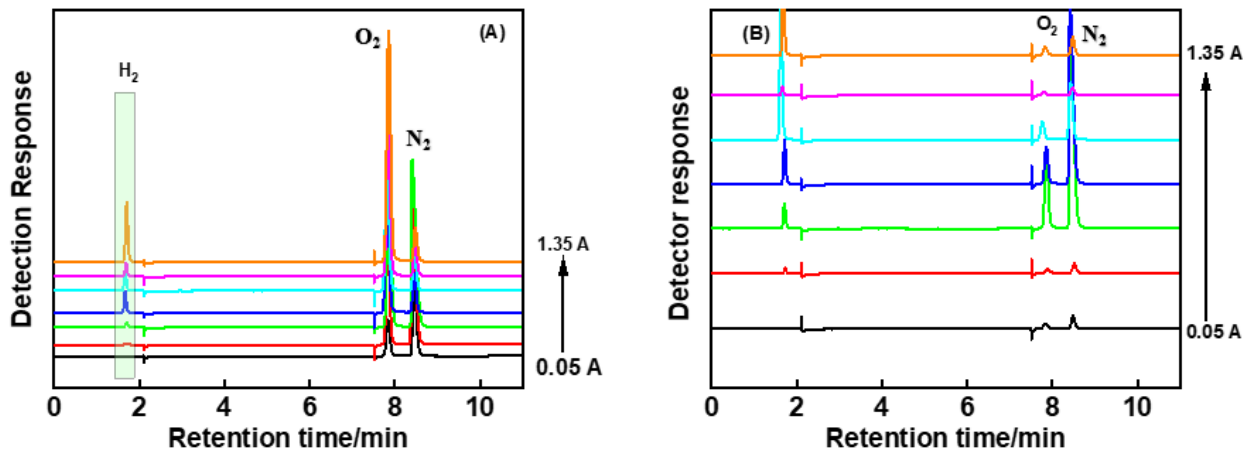

Figure 3.7. *Gas chromatograms obtained (A) Anode stream and (B) Cathode stream at different current densities during a 5-hour test for a 0.5 M silicotungstic acid at 40 °C and a catholyte flow rate of 250 mL* min^{-1}.

These chromatograms show the H_2 peak observed at each retention time, along with a small peak for O_2 (from the air) in the catholyte stream (Fig. 3.7b) and negligible hydrogen in the anolyte stream (Fig. 3.7a) for most current densities. This suggests excellent decoupling of the hydrogen evolution reaction from the oxygen evolution reaction in the oxygen-generating cell. Table 3.2. Percentage hydrogen by volume in the catholyte and anolyte loop headspaces (each of which is 250 mL) after roughly 5 h of electrolysis at the current densities indicated, using a silicotungstic acid concentration of 0.5 M at 40 °C with an anolyte flow rate of 40 mL min^{-1} and a catholyte flow rate of 250 mL min^{-1}.

Current density (A/cm^2)	**% hydrogen in the catholyte headspace**	**Decoupling efficiency (%)**	**% hydrogen in the anolyte headspace**
0.05	0.02	99.99+	0.0
0.1	0.02	99.99+	0.01
0.25	0.03	99.99+	0.02
0.5	0.04	99.99+	0.02
1.0	0.06	99.99+	0.03
1.2	0.74	99.99	0.05
1.35	0.83	99.99	0.64

Table 3.2 shows that the gas crossover of hydrogen into the oxygen stream at the anode of the oxygen-producing cell was negligible even at low current densities (0.05 A/cm^2).

After running in a steady state for around 5 hours, the mediator solution in the catholyte loop was fully re-oxidised by opening the circuit on the oxygen-generating cell and applying a potential to the hydrogen-generating cell only. The amount of charge passed was fixed at 3370 C. Towards the very end of the passage of this amount of charge, the mediator solution turned from blue to colourless, further suggesting complete re-oxidation..

3.7.2. Anode electrode characterisation

The IrO_2/Ti felt electrode surface was analysed by X-ray photoelectron spectroscopy (XPS) before and after electrolysis at different current densities to determine the presence of IrO_2 catalyst after electrolysis, with an anolyte flow rate of 40 mL min^{-1}, for 5 hours at 40 °C. Fig. 3.8a illustrates the XPS survey spectra for the prepared IrO_2/Ti felt electrodes before and after electrolysis, alongside a bare (undecorated) Ti felt for comparison. "After electrolysis" refers to the extensive usage at a range of current densities between 0.05 and 1.35 A/cm^2. The tungstic (W) and fluoro (F) peaks were attributed to silicotungstic acid and Nafion, respectively; the latter was used as an ionomer during electrode preparation.

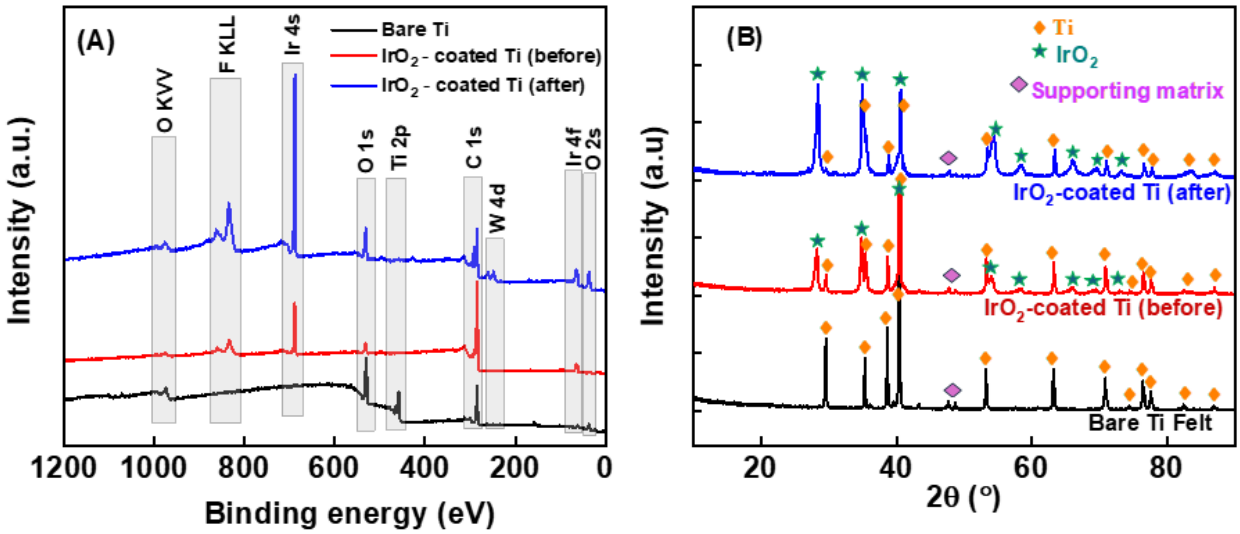

Figure 3.8. *Wide-scan (**a**) XPS and (**b**) XRD spectra of a bare Ti felt and an IrO_2-coated Ti electrode before and after electrolysis in a flow cell containing 0.5 M silicotungstic acid at 40 °C and a catholyte flow rate of 250 mL min^{-1}.*

Fig. 3.9 presents the XPS analysis of the bare Ti substrate. The XPS spectra were deconvolved to determine the specific binding energies (eV) of the Ti 2p, O 1s, and Ir 4f signals at the surface of the IrO_2-coated electrode, both before and after electrolysis (Fig. 3.10).

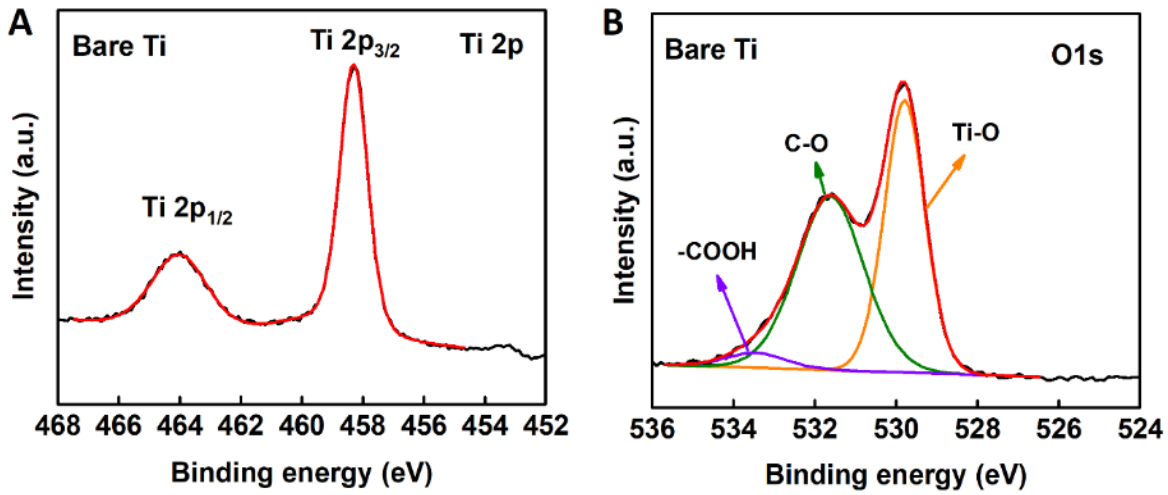

Figure 3.9. *Deconvoluted Ti 2p (a) and O 1s (b) for a fresh (undecorated) Ti felt.*

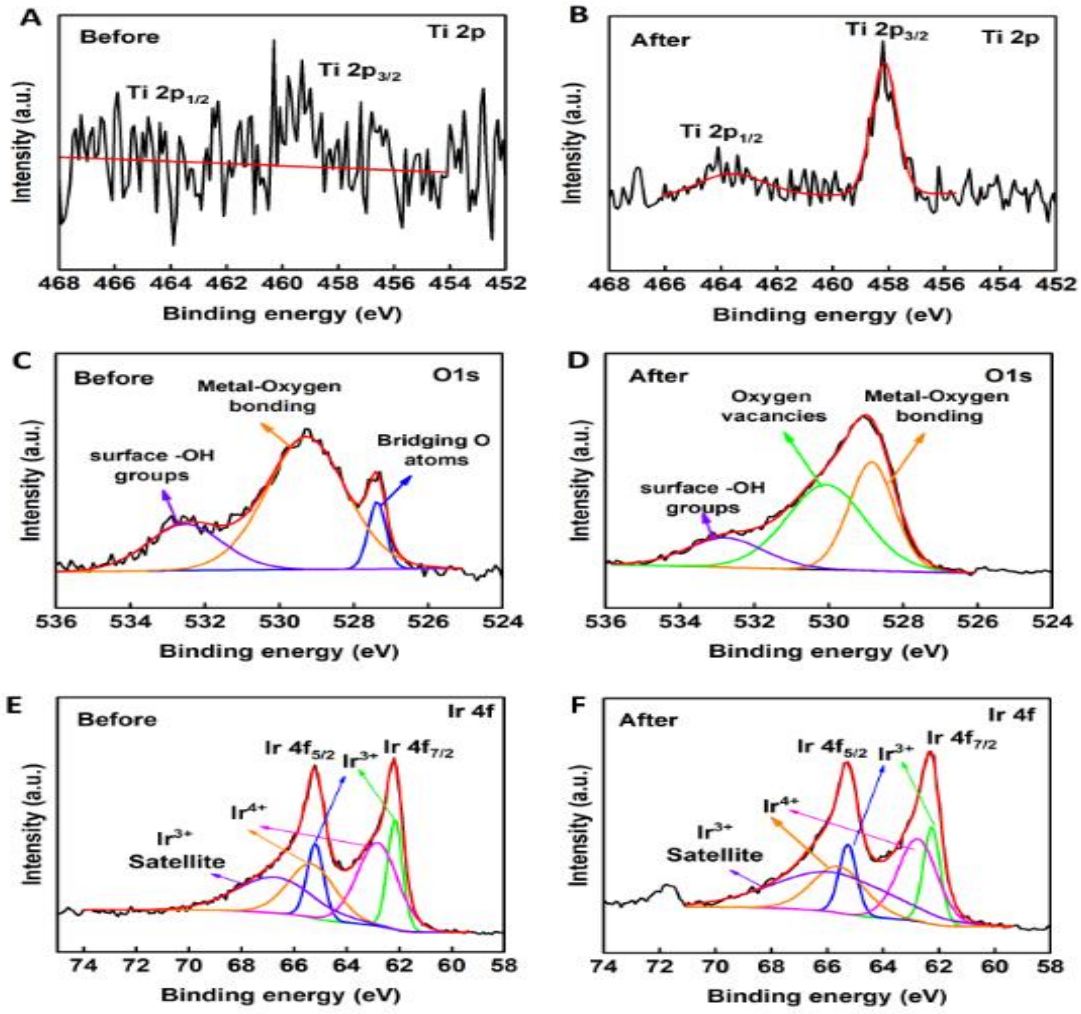

Figure 3.10. *Deconvoluted XPS spectra for an IrO_2-coated Ti felt electrode are as follows: (a) Ti 2p before electrolysis, (b) Ti 2p after electrolysis, (c) O 1s before electrolysis, (d) O 1s after electrolysis, (e) Ir 4f before electrolysis, (f) Ir 4f after electrolysis. Electrolysis was performed in a flow cell containing 0.5 M silicotungstic acid at 40 °C and a catholyte flow rate of 250 mL min^{-1}.*

Following electrolysis (obtained after 180 days of contact with silicotungstic acid in the cell, while varying the current density from 0.05 to 1.35 A/cm^2), analysis of the Ti 2p peaks at 459.3 eV (Ti $2p_{3/2}$) and 465.0 eV (Ti $2p_{1/2}$) indicated some breakthrough of the underlying Ti. However, there is no total loss of the Ir catalyst, as Ir is still clearly present at the electrode surface (Fig. 3.10b) after electrolysis.[18] The O 1s XPS spectra of the IrO_2-coated electrode before and after the electrolysis can be deconvoluted into three peaks (Fig. 3.10c and d). Slight differences are observed. The primary O 1s peak at 529.8 eV is attributed to Ir-O bonding, while a minor peak at 532.9 eV corresponds to surface hydroxyl groups present on both

electrodes. On the other hand, the peak at 528.4 eV, corresponding to 2-fold coordinated bridging oxygen atoms, is evident before electrolysis. In contrast, the peak around 531.3 eV is associated with oxygen vacancies (oxygen defects) formed after electrolysis.[18-20] The XPS spectra of Ir 4f (Fig. 3.10e and 3.10f) exhibit similarity before and after the experiments, suggesting that the IrO_2 catalyst is not completely leached at the surface of the anode electrode. The XPS spectra of Ir 4f revealed distinct peaks at 65.1 eV ($4f_{5/2}$) and 62.1 eV ($4f_{7/2}$), indicating the presence of the Ir^{3+} state. Additionally, peaks were observed at 66.4 eV ($4f_{5/2}$) and 63.5 eV ($4f_{7/2}$), corresponding to the unscreened component of the Ir^{4+} state.[20, 21] The peak at 66.4 eV is also attributed to the shake-up satellite of the Ir^{3+} species.[19, 22, 23]

To probe the phase composition of the Ti/IrO_2-coated electrode, X-ray diffraction (XRD) analysis was performed. The diffractograms revealed characteristic peaks related to the substrate and well-defined peaks for the IrO_2 layer, characteristic of a crystalline structure (Fig. 3.11b). The XRD data for the prominent peaks observed in the diffractograms were compared with XRD data from the JCPDS (Joint Committee on Powder Diffraction Standards). As shown in Fig. 3.10b, the characteristic peaks corresponding to the Ti felt were relatively narrow and intense and assigned to the rutile crystal structure. In the case of Ti/IrO_2, single peaks were observed for the 110 and 220 phases ($2\theta = 28°$, 58°, 65°, and 69°, respectively), corresponding to PDF card number 1538153, confirming the presence of IrO_2 after the electrolysis process. Similar observations have been reported in the literature.[23, 24] Furthermore, diffraction peaks corresponding to the Ti substrate were observed, but no TiO_2 was detected. SEM micrographs (Fig. 3.11a) depict the morphology of the IrO_2/Ti surface and, combined with EDX analysis (Fig. 3.11b), confirm the presence of iridium on the titanium surface.

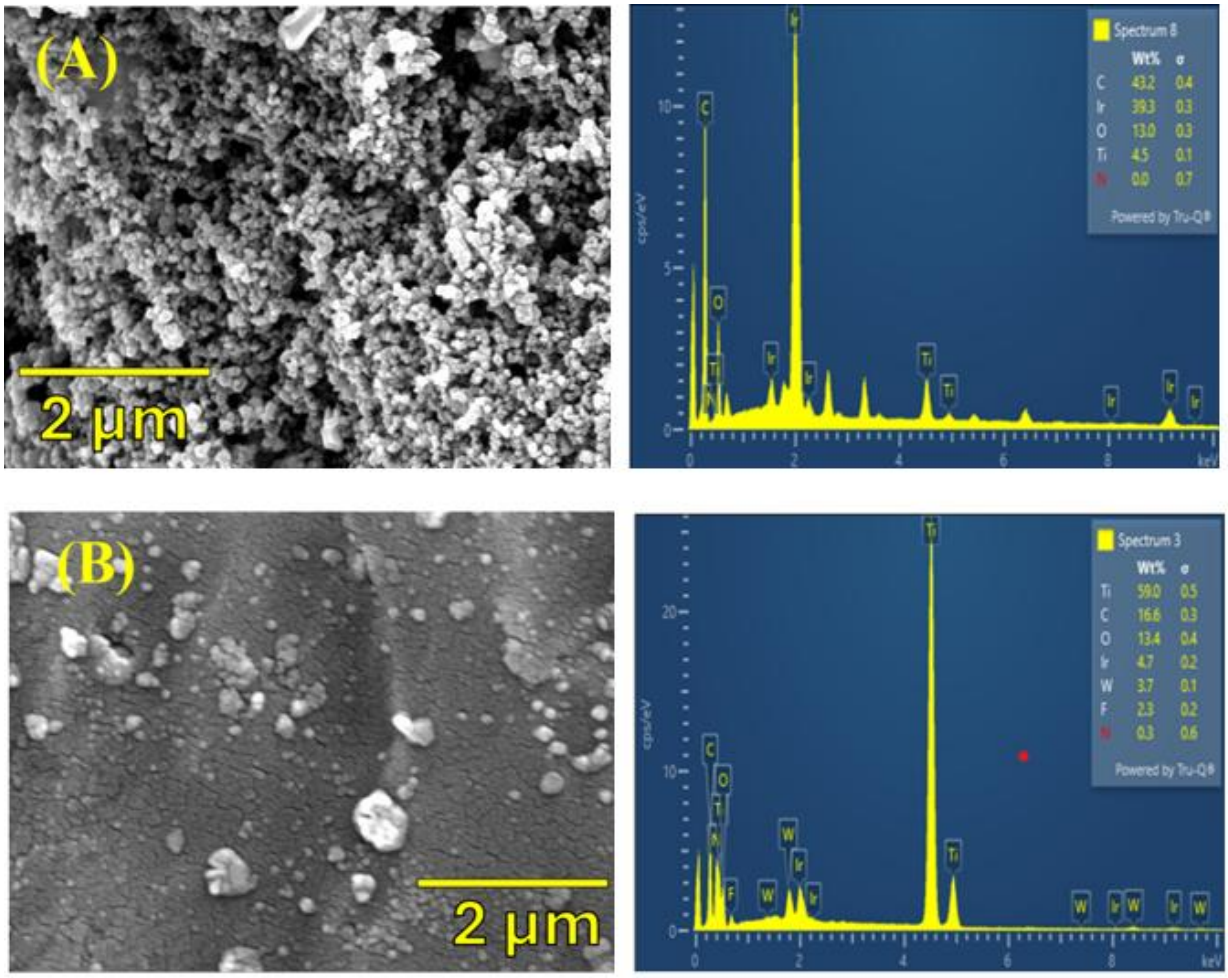

Figure 3.11. *SEM/EDX images of (**a**) the IrO_2/Ti electrode prepared by air spraying deposition before electrolysis and (**b**) after electrolysis at a range of current densities in a flow cell containing 0.5 M silicotungstic acid at 40 °C and a catholyte flow rate of 250 mL min^{-1}.*

Fig. 3.11(a) and (b) present the (before and after) surface morphology of the IrO_2/Ti electrode. The micrographs and EDX analysis indicate that, before electrolysis, the IrO2 particles are evenly dispersed on the Ti felt surface, as expected from the air-spraying deposition process, forming large spots and numerous nanoparticles, which are visible in the SEM images as white patches (Fig. 3.12a). One can also notice that the IrO_2 on the Ti surface (Fig. 3.11b) has not been completely leached out even after electrolysis. Based on EDX analysis, the Ir/Ti composite had 4.5 wt% Ti and 39.3 wt% Ir before electrolysis and 59.0 wt% Ti and 4.7 wt% Ir after electrolysis. The change in the composition of Ir after electrolysis can be attributed to prolonged contact (>180 days) with the silicotungstic acid solution at various current densities (0.05–1.35 A/cm^2). The EDX spectrum in Fig. 3 .11 shows the composition of the other elements present at the electrode surface.

Finally, to determine the extent to which Ir had been leached from the anode after 180 days in contact with the silicotungstic acid solution at various current densities (0.05–1.35 A/cm^2), ICP-OES measurements were performed. The samples were diluted in 2% HNO_3 and analysed by ICP-OES. The ICP-OES measurements showed Ir below the detection limit (≤ 0.1 ppm), indicating that no Ir was leached into the anolyte stream during a 24-hour test period, and no leachates were detected in the cathode stream. However, 576.83 ppm of Ir was leached into the anode stream after more than 180 days of contact with the silicotungstic acid solution, with 34.45 ppm detected in the catholyte stream during this period.

3.8. Conclusions

In this work, we have demonstrated the operation of a flow cell system using silicotungstic acid as a redox mediator for the near-complete decoupling of the oxygen and hydrogen evolution reactions, utilising a water oxidation catalyst (IrO_2) applied directly to the gas diffusion layer (Ti felt) across a range of current densities. The system was placed in steady state for numerous mediator turnovers at these current densities, undergoing approximately 60 turnovers at the highest current density probed (1.35 A/cm^2). Across the full range of current densities probed (0.05 – 1.35 A/cm^2), the decoupling efficiency remained well in excess of 99%, suggesting that even at the higher current densities, the reduction of the mediator can be engineered to out-compete hydrogen evolution within the oxygen-generating electrochemical cell. Current densities of 1.35 A/cm^2 are approaching those achievable with conventional proton exchange membrane electrolysers, highlighting that rapid oxygen production with coupled redox mediator reduction is possible without compromising decoupling efficiency. At the other end of the scale, current densities as low as 0.05 A/cm^2 could be harnessed for oxygen production and mediator reduction without co-generation of hydrogen, thereby eliminating the risk of hydrogen permeation into the oxygen stream.

By moving the catalyst for the oxygen evolution reaction to the gas diffusion layer (as opposed to applying this catalyst directly on the membrane as a membrane electrode assembly), the construction of the cells was simplified, raising the prospect that membranes of different sorts could be readily swapped in and out of the electrochemical cell. Very little attempt was made to optimise the deposition or performance of these IrO_2/Ti anodes; nevertheless, they displayed passable activity and stability under the reaction conditions, retaining sufficient Ir to remain active after 180 days in contact with the electrolyte and after performing many hours of electrolysis. Given the expense of membrane electrode assemblies, the ability to deposit catalysts on the gas diffusion layer and to use undecorated membranes could be a distinct advantage, especially as decoupled systems based on liquid electrolytes, such as in this case, only require a membrane to prevent the reduced mediator from being re-oxidised at the anode (which would result in wasteful redox cycling). Moving the catalyst to the gas diffusion layer should enable a broader range of potential separators to be screened and assessed for efficacy. Furthermore, carbon black was incorporated into the ink during preparation to enhance conductivity; however, it likely did not withstand the anodic conditions of the OER and should therefore be omitted in future work.

References

1. F. Kourougianni, A. Arsalis, A.V. Olympios, G. Yiasoumas, C. Konstantinou, P. Papanastasiou. *Ren. Energy,* 2024, 231, 120911.
2. F. Chen, B. Chen, Z. Ma, and M. Mehana. *Ren. and Sust. Energy Transition,* 2024, *5*, 100077.
3. F.R. Malik, H.B. Yuan, J.C. Moran, N. Tippayawong. *Eng. Sci. and Tech, an Int. J.,* 2023, *43*, 101452.
4. S.S. Kumar, and V. Himabindu. *Mat. Sci for Energy Tech.* 2019, *2*, 442-454.
5. S.H. Kim, B.T.D. Nguyen, H. Ko, M. Kim, K. Kim, S.Y. Nam, J.F. Kim. *Int. J.of Hydrogen Energy,* 2021, *46*, 15135-15144.
6. S. Garbe, U. Babic, E. Nilsson, T.J. Schmidt, L. Gubler. *J. of the Elect. Society,* 2019, *166*, 873-877.
7. M. Schalenbach, M. Carmo, D.L. Fritz, J. Mergel, D. Stolten. *Int. J. of Hydrogen Energy* 2013, *38*, 14921-14933.
8. H. Ito, N. Miyazaki, M. Ishida, A. Nakano. *Int. J. of Hydrogen Energy,* 2016, *41*, 20439-20446.
9. P.J. McHugh, A.D. Stergiou, And Symes, M. D. *Adv. Energy Mat.* 2020, *10*, 2002453.
10. M.D. Symes, and L. Cronin, *Nature Chemistry,* 2013, *5*, 403-409.
11. Z.P. Ifkovits, J.M. Evans, M.C. Meier, K.M. Papadantonakis, And N.S. Lewis, N. *Energy & Env. Sci.* 2021, *14*, 4740-4759.
12. I. Slobodkin, E. Davydova, M. Sananis, A Breytus, A Rothschild. *Nature Materials,* 2024, *23*, 398-405.
13. J. Huang, And Y. Wang, *Cell Reports Physical Sci.* 2020, *1*, 100138.
14. B. Rausch, M.D. Symes, G. Chisholm, L. Cronin. *Science,* 2014, *345*, 1326-1330.
15. G. Chisholm, L. Cronin, M.D. Symes. *Electrochimica Acta,* 2020, *331*, 135255.
16. M.M. Tellez-Cruz, J. Escorihuela, O. Solorza-Feria. *Polymers,* 2021, *13*, 3064-3118.
17. B. Keita, L. Nadjo, L. *J. of Elect. Chemistry and Interfacial Electrochemistry,* 1987, *227*, 77-98.
18. C. Van Pham, M. Bühler, J. Knöppel, M. Bierling, D.Seeberger, D.Escalera-López, K.J. Mayrhofer. *Appl. Catalysis B: Env,* 2020, *269*, 118762.
19. Y. Park, J. Lee, And Y. Park. *Frontiers in Chemistry,* 2020, *8*, 593272.
20. G. Liu, F. Hou, X. Wang, B. Fang. *Appl. Surface Science,* 2023, *615*, 156333.

21. R. Badam, M. Hara, H.H. Huang, M. Yoshimura. *Int. J. of Hydrogen Energy* 2018, *43*, 18095-18104.
22. D.N.G. Krishna, And J. Philip. *Appl. Surface Science Advances,* 2022, *12*, 100332.
23. R. Martin, M. Kim, C. Lee, V. Mehar, S. Albertin, U. Hejral, L.R. Merte, L. *The J. of Phy. Chemistry Letters,* 2020, *11*, 7184-7189.
24. Z.S. Rajan, T. Binninger, P.J. Kooyman, D. Susac, R. Mohamed. *Catalysis Sci. & Tech.,* 2020, *10*, 3938-3948.

CHAPTER FOUR

Solution-Phase Decoupled Water Electrolysis In A Flow Cell With A Simple Size Exclusion Membrane Separator.

This chapter contains expanded and updated sections from the following publication "Solution-Phase Decoupled Water Electrolysis In A Flow Cell With A Simple Size Exclusion Membrane Separator"

Obeten Mbang Eze, Zeliha Ertekin, Paula L. Lalaguna, Malcolm Kadodwala and Mark D. Symes.

Fuel 409 (2026) 137740.

https://doi.org/10.1016/j.fuel.2025.137740

Acknowledgements and Declarations

I would like to sincerely thank Paula L. Lalaguna and Malcolm Kadodwala for their assistance with the atomic force microscopy micrographs. The content of this chapter was initially developed in collaboration with Zeliha Ertekin and my supervisors, Prof. Mark Symes. I thank everyone for their valuable contributions to the original review. Any sections not authored by me in the original manuscript have been either omitted or entirely rewritten, ensuring that the work presented here is solely my own.

4.1. Introduction

This chapter explores the performance of a decoupled electrolysis flow system over 5 hours at a range of current densities (25-750 mA/cm^2), utilising a commercially available cellulose-based dialysis membrane. Key potential advantages of such an approach are that size-exclusion separators are typically cheaper and more environmentally friendly than the industry-standard perfluorinated membranes used in proton exchange membrane electrolysers, which are classified as so-called "forever chemicals" and are very difficult to recycle.[1-11]

Symes *et al.* in 2013 demonstrated that a commercially available benzoylated cellulose dialysis membrane designed to exclude molecules with molecular weights above 1,200 could replace the Nafion membrane in a simple glassware H-cell .[12] This membrane was found to be freely permeable to H_2 while effectively suppressing crossover of the larger redox mediator, with a measured crossover rate of less than 1.5×10^{-10} mol h^{-1} over two weeks. Current–voltage analysis demonstrated that cell performance remained comparable to that achieved with a Nafion separator, suggesting that cellulose-based dialysis membranes could be viable in decoupled electrolysis systems. However, that study examined performance only at low current densities (<50 mA/cm^2) in glassware H-cells operated in batch mode.[12]

In this Chapter, the extent of parasitic hydrogen gas production and crossover during electrolysis with a commercially available cellulose-based dialysis membrane was quantified. The results bear out that decoupled electrolysis using such size-exclusion membranes could be viable; however, challenges related to membrane resistance and stability during operation (particularly at current densities above 500 mA/cm^2) remain significant. The work identifies lower-resistance, more stable size-exclusion membranes as a key research challenge for this field going forward.

4.2. Materials and Methods

The electrochemical flow cells used in this study are shown in Fig. 4.1, which includes all components of the electrochemical cell setup, with the only difference being the replacement of the membrane in the OER cell with a cellulose dialysis membrane. The system consisted of two separate electrochemical cells: one for oxygen generation and one for hydrogen generation, operated simultaneously and connected via two peristaltic pumps (MasterFlex) to circulate the redox mediator. The oxygen-generating cell was controlled using a BioLogic SP-150 potentiostat coupled to a BioLogic VMP-3B 20 A/20 V booster, while the hydrogen-generating cell was operated using an Admiral SquidstatPlus potentiostat.

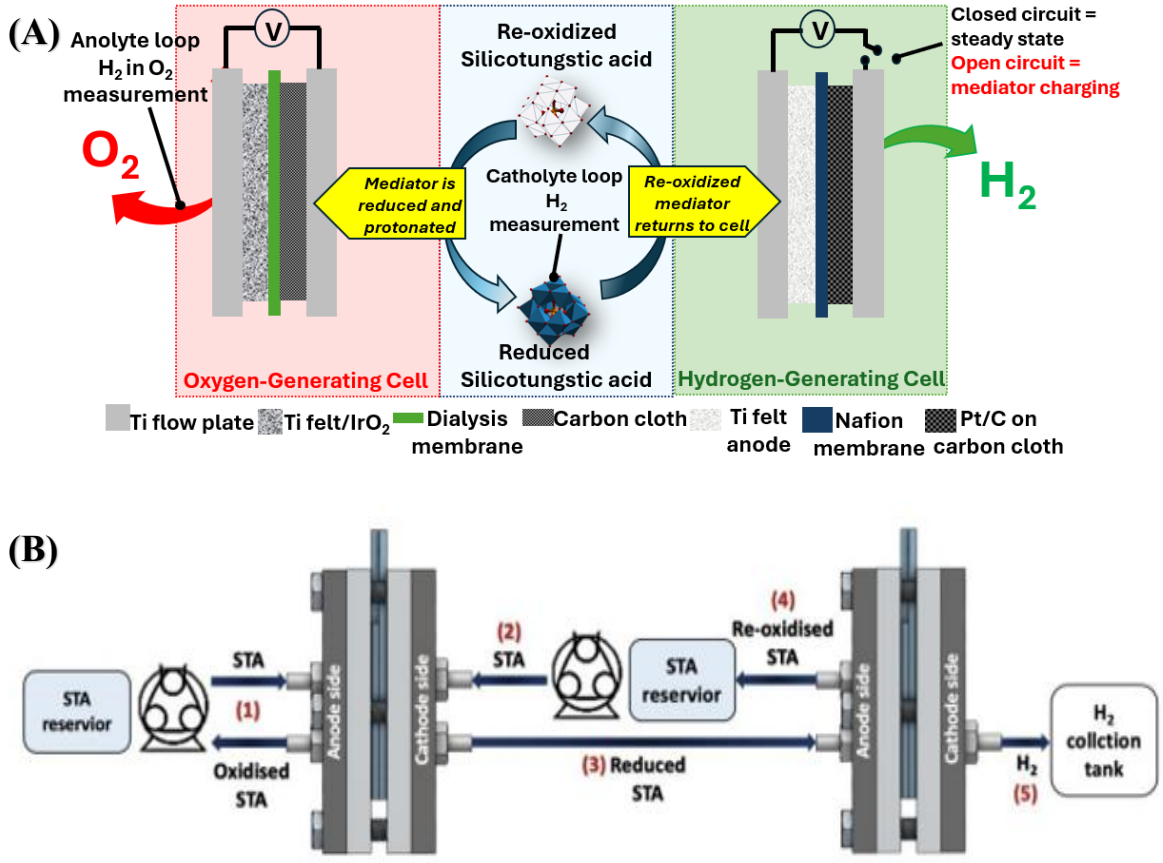

Figure 4.1. *(**A**) Schematic of the flow cell system designed, constructed, and used in this study, **(B)** 2-D drawing of the flow cell showing the peristaltic pumps and the STA reservoir.*

4.3. Bulk electrolysis

Oxygen production in the first cell was achieved by applying a fixed current with the BioLogic SP-150. Before each experiment, argon was bubbled through the mediator solutions for 45 minutes to eliminate residual oxygen in the system. Meanwhile, hydrogen generation in the second cell was powered by an Admiral SquidstatPlus potentiostat, which supplied the current. Equal currents were maintained across both cells in order to place the system into steady-state operation.

4.4. Electrochemical impedance spectroscopy

The flow cell was constructed and tested using parameters presented in Table 4.1, which utilises a least-squares optimisation routine to determine the flow cell resistance. The frequency range was from 50 kHz to 10 mHz with 6 measurement points per decade. Each 6-point per decade scan takes approximately 11 minutes and 20 seconds. The amplitude value is set to 10% of the applied current density. The flow cell voltage was monitored during scans to verify that there was no noticeable drift. This determination was qualitative, as the signal slightly affected the cell's output potential, most notably at low frequencies.

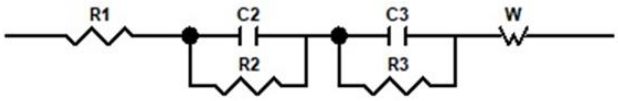

Figure 4.2*. The equivalent circuit model used in the electrochemical impedance spectroscopy analysis. Circuit components are defined in the main text.*

Table 4.1. The experimental parameters used in the electrochemical impedance measurements.

Applied Current Density (mA/cm^2)	500
Amplitude (mA/cm^2)	50
Initial Frequency (mHz)	10
Final Frequency (kHz)	50
Points/ Decade	6

In this model, R1 represents the ohmic resistance of the flow cell components. The charge-transfer resistances at the cathode and anode are denoted R2 and R3, respectively. Additionally, C2 and C3 correspond to the constant phase elements associated with the cathodic and anodic processes. W represents a Warburg element, which models diffusion. It has a phase of 45° and its magnitude decreases with the square root of frequency. A finite-length Warburg adjusts for limited diffusion distance.[14]

4.5. Membrane Characterisation

The membrane morphology after electrolysis was characterised by scanning electron microscopy. The scanning diffraction angle 2θ ranged from 10° to 90° at a rate of 5 minutes per data point, with a scanning rate of 1° min^{-1}. A scanning electron microscope (TESCAN CLARA) equipped with Energy-Dispersive X-ray Spectroscopy (Oxford Instruments UltimMax) was used to analyse surface morphology. Atomic force microscopy (AFM) measurements were performed using a Bruker Dimension Icon Atomic Force Microscope System in ScanAsyst and PeakForce tapping modes with a silicon tip (ScanAsyst-Air-HPI). Atomic force microscopy was performed on the dialysis membrane (1 cm × 1 cm) sample to detect the membrane's mean roughness parameter (R_a) both before and after electrolysis. To provide insights into the membrane's molecular structure and composition, as well as to identify its functional groups and chemical bonds, Fourier Transform Infrared (FTIR) spectroscopy was performed using a Nicolet™ Summit™ FTIR Spectrometer. Thermogravimetric analyses were performed using a TA Instruments thermogravimetric analyser (Discovery TGA-5500), and a DSC–TGA instrument (SDT Q600) was used to evaluate the membrane's thermal stability and degradation behaviour before and after electrolysis. The analysis was conducted at a heating rate of 100 °C to 600 °C in an argon flow of 100 mL/min.

4.6. Water Uptake and Ion Exchange Capacity Measurement

Water uptake was determined by measuring the weight difference between thoroughly dried and fully hydrated dialysis membranes. The membranes were dried in a desiccator for 24 hours and then soaked in deionised water for another 24 hours. Afterwards, the membranes were removed, wiped with tissue paper, and quickly weighed using a microbalance. The water uptake (W_{up}) of the membrane was calculated using equation 1:

$$W_{up} = \frac{W_w}{W_d} \times 100\%, \qquad [1]$$

where W_w and W_d are the weights of the wet and dry membranes, respectively.

Ion exchange capacity allows the determination of the accessible number of functional groups within a membrane, which directly or indirectly determines the thermal stability, water uptake, and conductivity of the membrane.[19] A regenerated cellulose dialysis membrane (SpectraPor® RC Membranes 3) comprises natural cellulose derived from cotton linters. The polymer structure of the membrane is based on cellulose fibres, which consist of repeating glucose units connected by β(1→4) glycosidic linkages.[19,20] These glucose units, in turn, contain hydroxyl (−OH) groups.[19] For the ion exchange capacity measurements, the regenerated cellulose dialysis membrane was first dried in a desiccator for 24 hours to remove any traces of water from the membrane and then immersed in a 0.01 M HCl solution for another 24 hours at room temperature. Before titration, the membrane was removed from the solution. The solution was then titrated with 0.01 M NaOH using phenolphthalein as the indicator. The experimental ion exchange capacity values were recorded as the average value for the sample in units of millimoles of NaOH per gram of the polymer membrane (mmol g^{-1}) and calculated using Equation 2:

$$Ion\ Exchange\ Capacity = \frac{0.01\ x\ W_{NaOH}}{W_d} \times 100\%, \qquad [2]$$

where W_d was the weight of the dried membrane (g), and V_{NaOH} was the titrimetric volume (mL) of the NaOH solution consumed during the titration.

4.7. Results and Discussion

4.7.1. Controlled current decoupled water electrolysis

The flow cell system (Fig. 4.1) was assembled with the anolyte and catholyte loops, each containing 100 mL of an aqueous 0.5 M fully oxidised silicotungstic acid ($H_4SiW_{12}O_{40}$) solution. The flow rate of the anolyte solution through the anode side of the oxygen-generating cell was 40 mL/min, while the flow rate of the catholyte solution through the cathode side was set to 250 mL/min. The reservoir temperatures for both the anolyte and catholyte were maintained using oil baths, ensuring that the feed temperatures entering the cell were 40 °C.

To begin, the silicotungstic acid mediator solution was always charged to 100% state of charge (corresponding to the complete one-electron reduction of $H_4SiW_{12}O_{40}$ to $H_5SiW_{12}O_{40}$) by passing a charge of 4824 C at a current density of 50 mA/cm^2 across the oxygen generation cell, while the circuit on the second cell was left open. Once the system had been fully charged to 100% state of charge, it was placed into steady state by closing the circuit on the hydrogen-producing cell and setting the current across that cell to match the current across the oxygen-generation cell (Fig. 4.3). In this way, it was possible to reduce the mediator in the oxygen-generation cell and re-oxidise it in the hydrogen-producing cell without changing the global state of charge of the mediator solution.

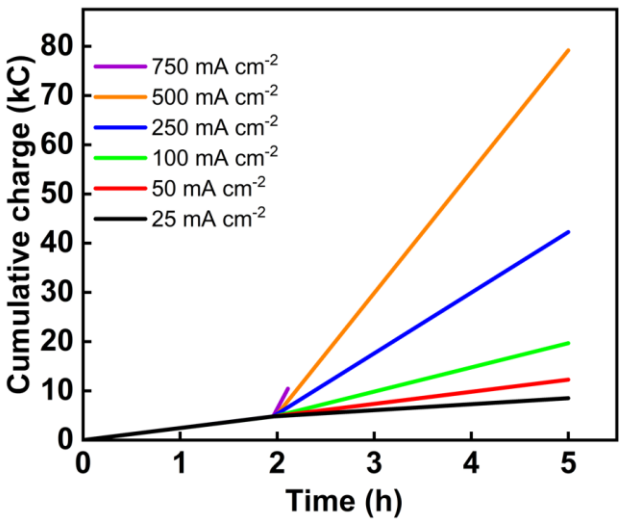

Figure. 4.3. *Charge-time curves at different steady-state current densities for 0.5 M silicotungstic acid at 40 °C and a catholyte flow rate of 250 mL min^{-1}. The mediator solution was charged to 100% state of charge by passing 4824 C at a current density of 50 mA/cm^2 before placing the cell into a steady state at various current densities as indicated.*

Table 4.2 shows the cell voltages obtained when various steady-state current densities were applied across the two cells. For each current density, the experiment was repeated three times, and the cell voltages reported are the mean of the final cell voltages (obtained at the end of each 5 h experiment). Error margins are the standard deviations from these mean values.

Table 4.2. Average cell voltages across the OER cell at different steady state current densities with a silicotungstic acid concentration of 0.5 M, at 40 °C, with an anolyte flow rate of 40 mL min^{-1} and a catholyte flow rate of 250 mL min^{-1}. The energy efficiency was calculated by dividing the thermoneutral voltage for water splitting at 40 °C (approximately 1.48 V) by the applied cell voltage for each current density.

Steady-state current density (mA/cm^2)	25	50	100	250	500
Total charge passed in steady state (C)	3753	7506	15012	37530	75060
OER Cell Voltages (V)	2.19 ± 0.03	2.26 ± 0.06	2.61 ± 0.03	4.01 ± 0.07	5.44 ± 0.52
Initial Stage of Charge (%)	100	100	100	100	100
~~**Final Stage of Charge (%)**~~	~~100~~	~~100~~	~~100~~	~~100~~	~~100~~
Energy efficiency (%)	67	65	57	37	27
Decoupling Efficiency (%)	99.91	99.90	99.93	99.84	99.76

A range of current densities from 25 to 750 mA/cm^2 was probed. However, at 750 mA/cm^2, the membrane appeared to fail, with holing observed in the dialysis membrane (Fig. 4.8c). At the highest current density tested at which stable performance could be obtained (500 mA/cm^2), the total charge passed was 75,060 C, over the ~3 h of steady state operation, corresponding to over 15 turnovers of the mediator, suggesting that the mediator is cycling between the

$H_5SiW_{12}O_{40}$ and $H_4SiW_{12}O_{40}$ forms multiple times. Fig. 4.4 shows the average OER cell voltages obtained during this steady-state operation.

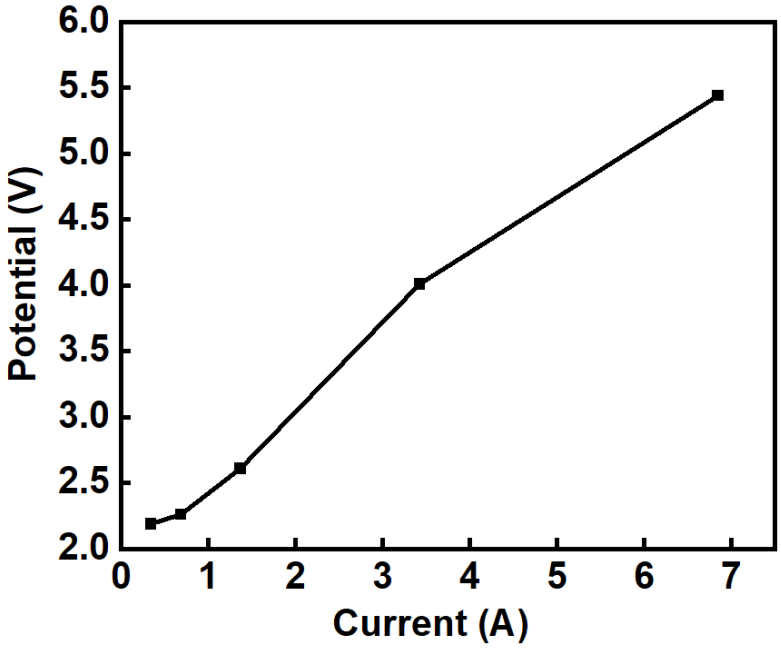

Figure 4.4. *Current-potential curve for the flow cell system used in this work with a dialysis membrane.*

After running the system in a steady state for just over 3 h at each current density, the mediator solution in the catholyte loop was fully re-oxidised by opening the circuit on the oxygen-generating cell and applying a current to the hydrogen-generating cell only. The amount of charge passed during re-oxidation was fixed at 4284 C. Towards the very end of the passage of this amount of charge, the mediator solution turned from blue to colourless, suggesting complete re-oxidation. Fig. 4.5 illustrates the hydrogen percentage (%) detected in the oxygen (anode) stream and the mediator (catholyte) stream as a function of current density. In all cases, the crossover of hydrogen into the oxygen stream at the anode of the oxygen-producing cell was negligible even at low current densities (25 mA/cm^2). The amount of hydrogen generated parasitically (in competition with mediator reduction) at the cathode of the oxygen-generating cell was similarly low across the range of current densities probed. Error bars on these measurements were determined from the standard deviations of three repeat measurements in each case, with at least 99.9% decoupling efficiency observed at all current densities.

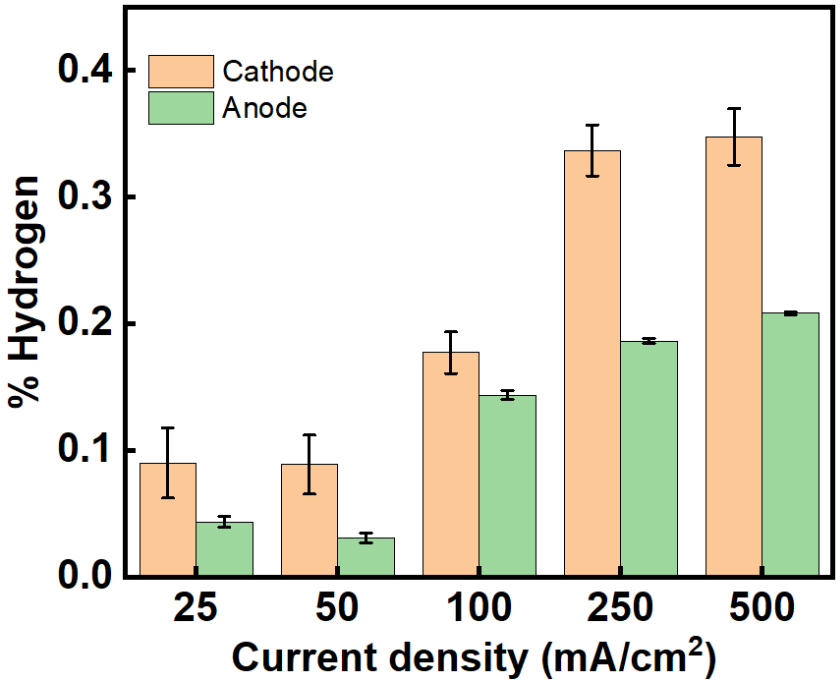

Figure 4.5. *Measurements of hydrogen in the anode and catholyte loops of the oxygen-generating cell at different current densities, using 0.5 M silicotungstic acid at 40 ℃ for 5 hours. "% Hydrogen" indicates the headspace volume measurements obtained under various current densities (25-500 mA/cm^2). The data suggest that, in all cases, the hydrogen concentration in oxygen (green columns) remains below 0.4%, consistent with expectations for a properly decoupled system.*

Fig. 4.6 shows a Nyquist plot of the impedance data obtained at 500 mA/cm^2. The Nyquist plot helps identify resistances in the cell at the high-frequency (to the left of the curve) and low-frequency (to the right of the curve) intercepts on the Z' axis.[14-18]

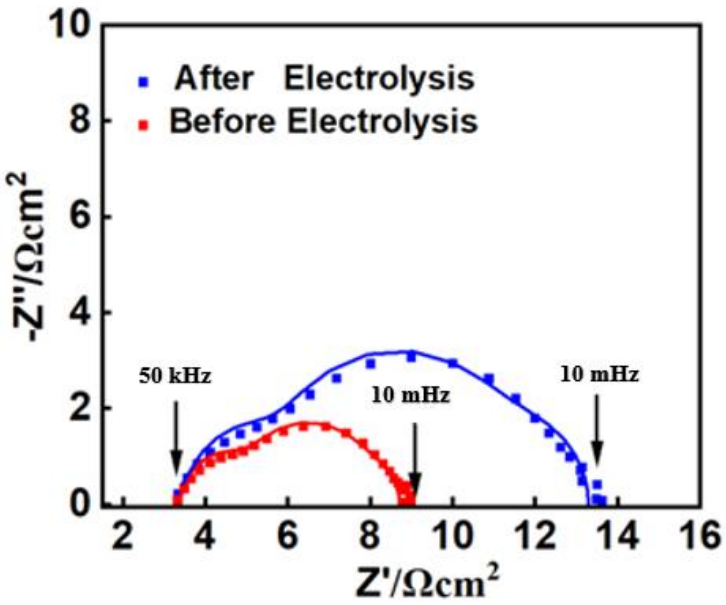

Figure 4.6. *Nyquist plots of the flow cell using Ti fibre felt at the anode and carbon cloth at the cathode (without any catalyst on the cathode electrode), separated by a regenerated cellulose dialysis membrane before and after electrolysis over a frequency range from 50 kHz to 10 mHz (50 kHz > 10 kHz > 1 kHz > 100 Hz > 10 Hz > 1 Hz > 0.1 Hz > 0.01 Hz) with 6 measurement points per decade in 0.5 M silicotungstic acid with anode flow rate of 40 mL* $min^{-1,}$ *while the cathode flow rate was 250 mL* min^{-1} *at 40 ℃. The fitting results for the equivalent circuit (see Fig. 4.2) are shown as Nyquist plots (solid lines).*

The total resistance of the dialysis membrane layer (R_{total}), calculated as the sum of the individual resistances ($R_1 + R_2 + R_3$), is presented in Table 4.3.

Table 4.3. Electrical parameters of the proposed equivalent circuit obtained after fitting the electrochemical impedance spectroscopy data results. Fitting errors for these measurements were determined from the chi-squared fitting values before and after measurements.

Applied Current Density (500 mA/cm²)	$R_1/\Omega cm^2$	$R_2/\Omega cm^2$	C_2/F	$R_3/\Omega cm^2$	C_3/F	W/Ohm	Fitting Error	R_{total} (Ωcm^2)
Before	3.123	3.048	$0.147x10^{-3}$	1.956	$1.24x10^{-3}$	0.222	$16.5x10^{-9}$	8.110
After	4.014	3.178	$1.014x10^{-3}$	5.845	0.0214	0.422	$80.6x10^{-6}$	13.028

Before electrolysis, the membrane exhibited a total resistance (Rtotal) value of 8.1 Ω/cm^2, which increased to 13.0 Ω/cm^2 after electrolysis. This increase in resistance could reflect progressive membrane deterioration, primarily caused by the rise in charge-transfer resistance (linked to electrode-electrolyte interactions), as reported in the literature.[21] These results show that at higher current densities, the membrane displays relatively high initial resistance, which then increases during electrolysis, which is likely to contribute directly to lowering the energy efficiency of the electrochemical cell (Table 4.2).

The membrane morphology before and after electrolysis (Fig. 4.7) was analysed using SEM, together with EDX analysis to evaluate any changes in elemental composition. Based on EDX analysis, the membrane had 34.4 wt% oxygen (O_2) and 65.6 wt% carbon before electrolysis, and 21.6 wt% tungsten, 46.1 wt% carbon, and 32.3 wt% oxygen after electrolysis at various current densities in a flow cell containing 0.5 M silicotungstic acid. The tungsten presumably originates from the silicotungstic acid mediator. Neither the data in Fig. 4.7 nor the associated EDX analysis gave any evidence for iridium being present on the membrane. However, several cracks were observed on the membrane surface after electrolysis (Fig. 4.8).

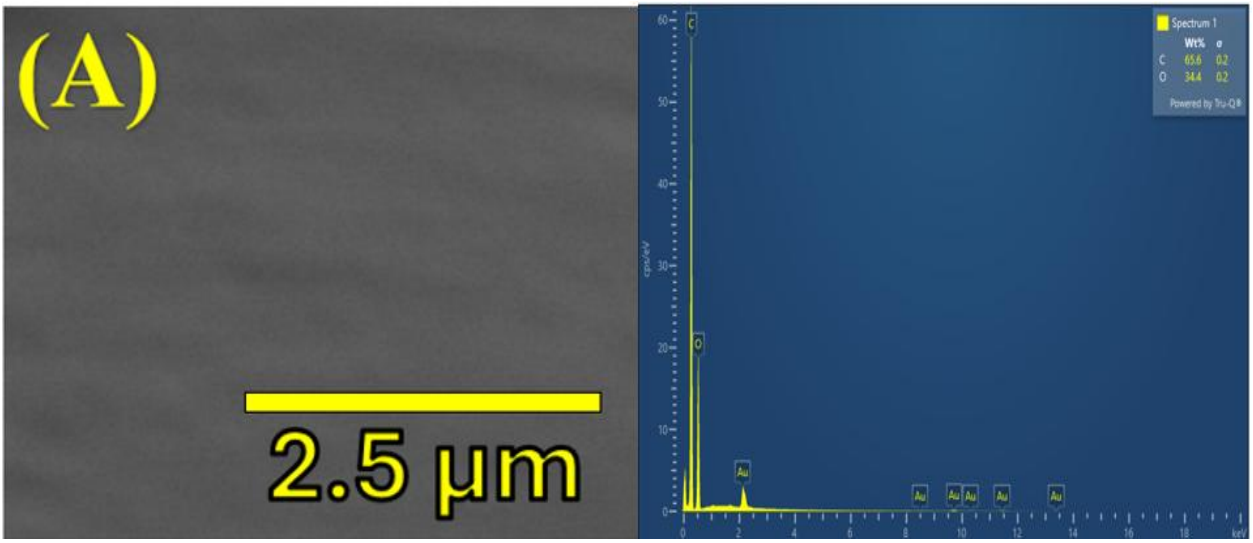

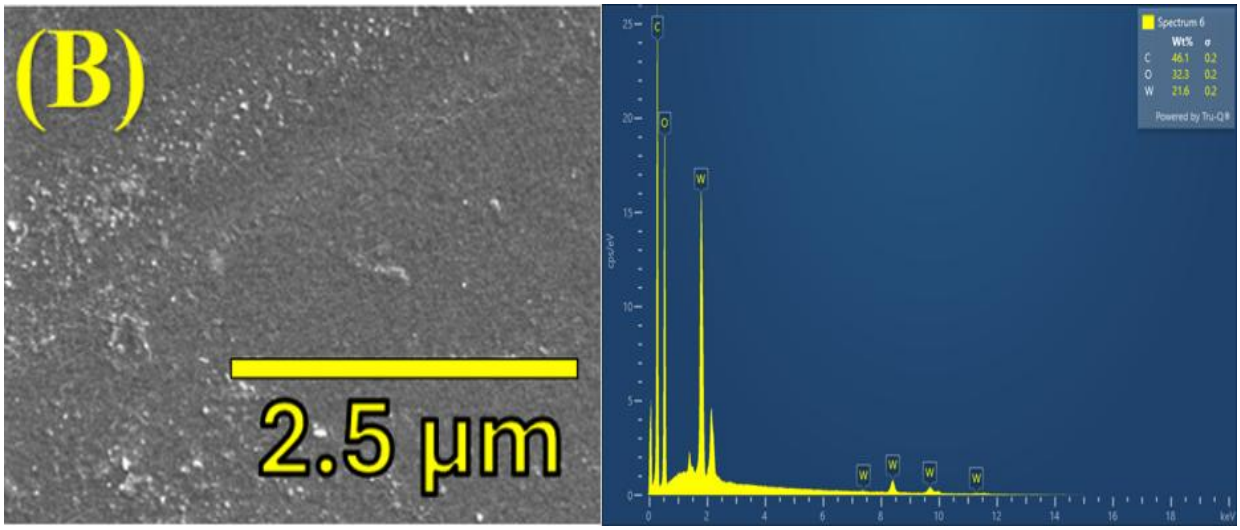

Figure 4.7*. SEM-EDX images of (A) the dialysis membrane before electrolysis and (B) the anode side of the dialysis membrane after electrolysis at various current densities in a flow cell containing 0.5 M silicotungstic acid at 40 °C and a catholyte flow rate of 250 mL/min.*

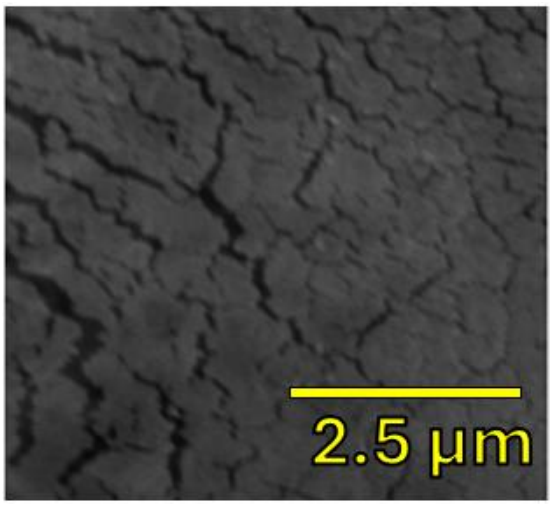

Figure 4.8. *SEM images of the regenerated dialysis membrane after electrolysis in a flow cell containing 0.5 M silicotungstic acid at 40 ℃ for 5 hours.*

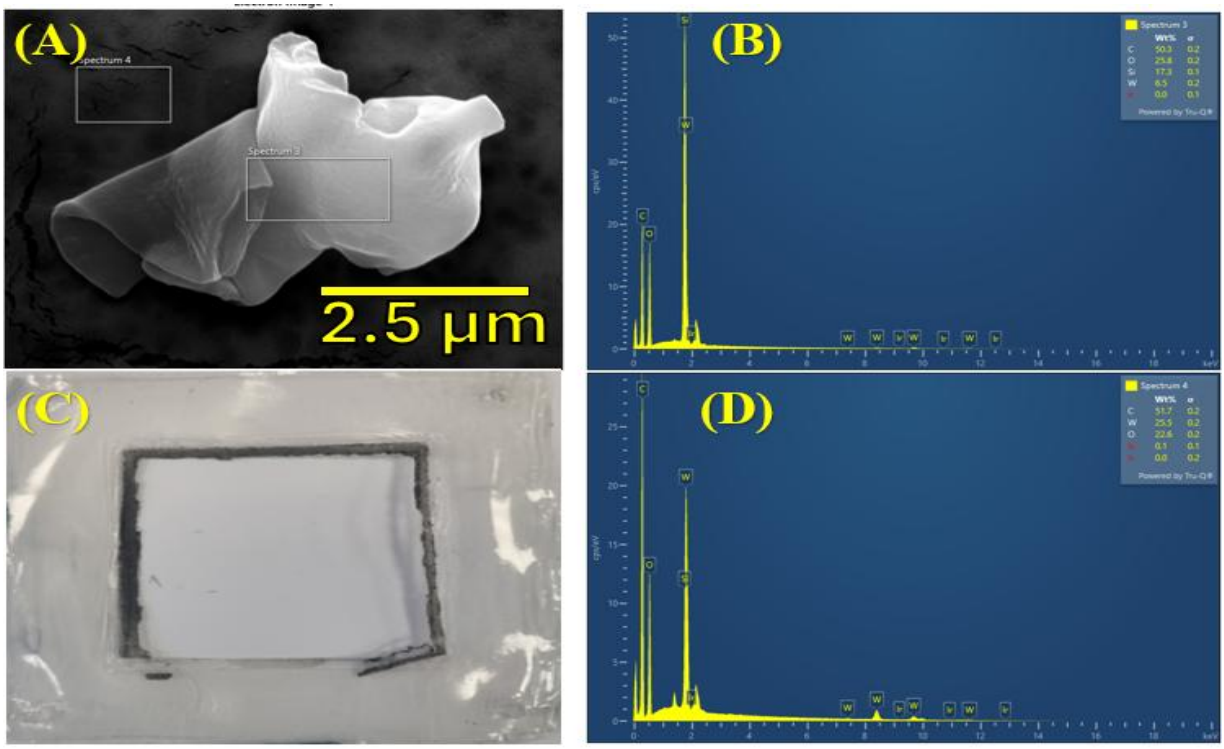

Figure 4.9. *The following were collected on a membrane after one complete set of steady-state current densities (25, 50, 100, 250, and 500 mA/cm^2) had been applied, each for 5 h, in a flow cell containing 0.5 M silicotungstic acid at 40 °C. (A) SEM mapping of the regenerated dialysis membrane, (B) EDX spectrum of the area covering the white material ("spectrum 3") in panel A, (C) photograph showing damage to the dialysis membrane after being placed into a steady state at a current density of 750 mA/cm^2 (the damaged area corresponds to a square 3.7 cm on each side) and (D) EDX spectrum of the area within the black box in panel A ("spectrum 4").*

The SEM/EDX analysis conducted on both the white spot and a region devoid of such features (as shown in Fig. 4.9, panel B) indicates a negligible presence of tungsten (W) with 17% silicon (Si). These elements, however, become apparent in the SEM images mapping following membrane exposure to the mediator $H_4SiW_{12}O_{40}$ in the flow cell environment (Fig. 4.9, panel B), suggesting a chemical interaction between the membrane surface and the mediator during electrolysis. Before electrolysis, EDX measurements revealed the membrane composition to be predominantly oxygen (65.6 wt%) and carbon (34.4 wt%), consistent with its original material structure. After electrolysis, the elemental profile shifted significantly, showing 21.6 wt% tungsten, 46.1 wt% carbon, and 32.3 wt% oxygen. This compositional change implies that

the mediator components were deposited or chemically bound to the membrane surface during operation.

The emergence of white spots on the membrane surface, as shown in SEM imaging, can be attributed to localised accumulations of silicotungstic acid. EDX mapping (Fig. 4.10) supports this hypothesis, showing concentrated regions of these elements corresponding to the white spots. These findings suggest that the electrochemical process not only alters the elemental makeup of the membrane but also induces morphological changes, potentially through the formation of carbon-rich domains. Such transformations influence membrane performance, durability, and interactions with other cell components, demanding further investigation into the long-term effects of mediator exposure on this membrane.

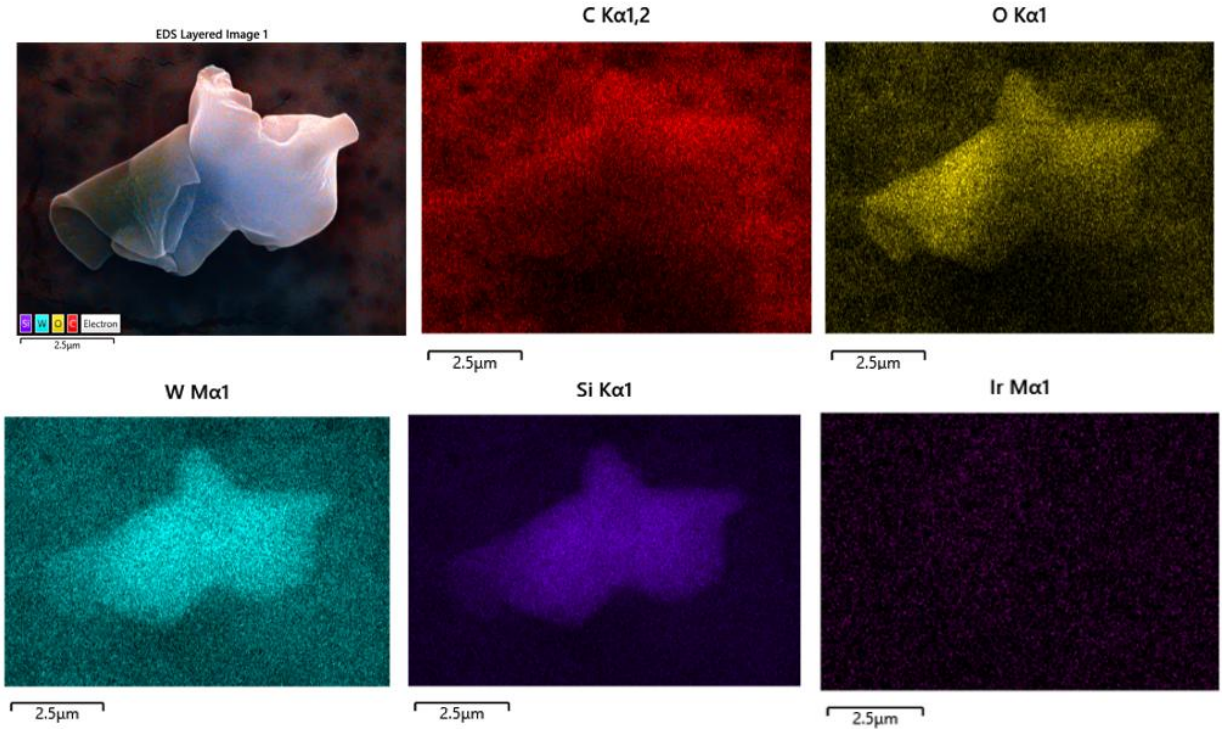

Figure 4.10. *(a) SEM image, and corresponding elemental maps of (b) C, (c) O, (d) W, (e) Si and (f) Ir of a regenerated cellulose dialysis membrane after being used for electrolysis. The system was held at each current density (25, 50, 100, 250, and 500 mA/cm^2) for 5 hours in a flow cell system containing 0.5 M Silicotungstic acid at 40 °C.*

Likewise, ICP-OES analysis revealed no detectable Ir leachate (Ir was below the detection limit of 0.1 ppm) in the electrolyte solution after a 120-day test period.

Figure 4.11 shows surface images of the regenerated cellulose dialysis membrane obtained by atomic force microscopy before and after electrolysis. During the scan, the force between the tip and the sample alters the cantilever's oscillation frequency and amplitude. The amplitude and frequency changes, with respect to the reference amplitude and frequency, are used as feedback signals to obtain the topography of the membrane surface (Fig. 4.11a, b and c). After electrolysis, variations in roughness can be observed (Fig. 4.11d, e and f). This may be due to oxidation of the membrane, as suggested by the greater presence of C=O stretches after electrolysis (see Fig. 4.12). The membrane was also noticeably more brittle after electrolysis.

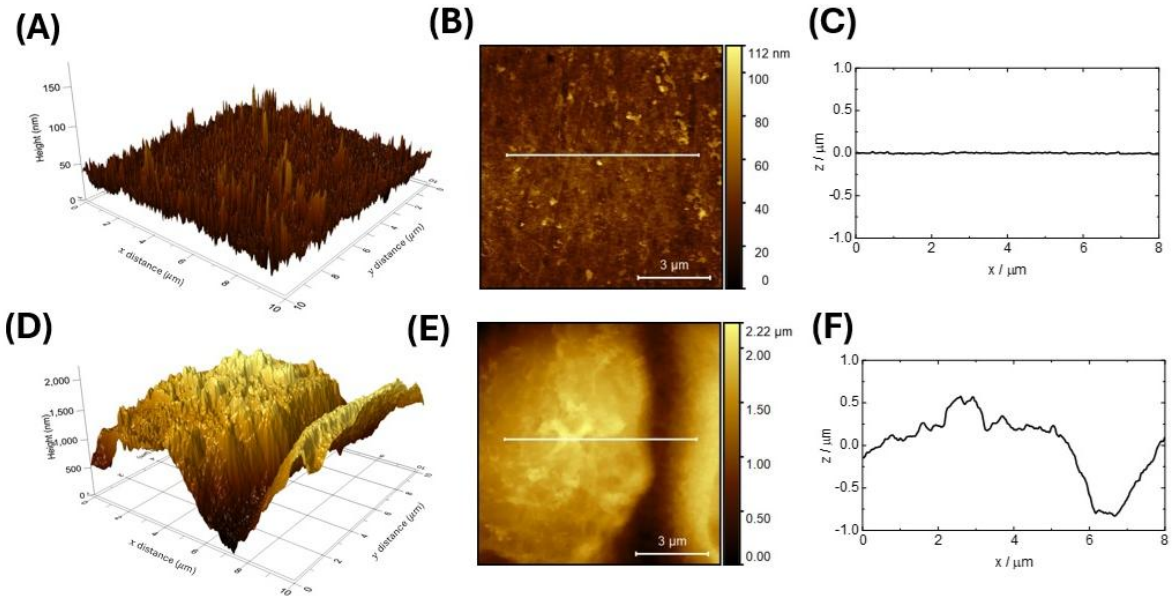

Figure 4.11. *Atomic force microscopy analysis of a regenerated cellulose dialysis membrane before (A and B) and after electrolysis (D and E). Panels (C and F) show height variation across the white cut lines in (B) and (E), respectively.*

Similarly, the mean roughness (R_a) parameter was obtained before electrolysis, with a R_a value of 6.93 nm. The roughness value obtained after electrolysis was relatively high, with a R_a of 354.8 nm, compared to previous studies, as shown in Table 4.3. Similarly, the membrane's surface height rises significantly: as shown in Fig. 4.11c and f, the maximum height rises from 111.8 nm before electrolysis to 2.224 µm after electrolysis.

Table 4.3. Comparison of Contact Angle and Surface Roughness

Cellulose source	Contact angle/°	Mean roughness (R_a)/nm		References
		Before	After	
Regenerated Cellulose Dialysis Membrane	26 ± 3	6.93	354.8	This work
Recycled Newspaper-Pulp	55.65 ± 3.83	18.5 ± 0.6	-	[22]
Softwood pulp	28 - 40	2.17 – 6.31	-	[22]

Contrary to the SEM image of the free surface of the regenerated dialysis membrane in Figure 4.10, a slightly rough surface of the dialysis membrane was observed in the AFM images. The high surface roughness is likely due to the formation of cracks (see Fig. 4.7), which promote irregularities on the membrane surface.

Similarly, Fourier transform infrared spectroscopy (FTIR) was used to probe changes in the membrane's chemical composition resulting from electrolysis (Fig. 4.12).

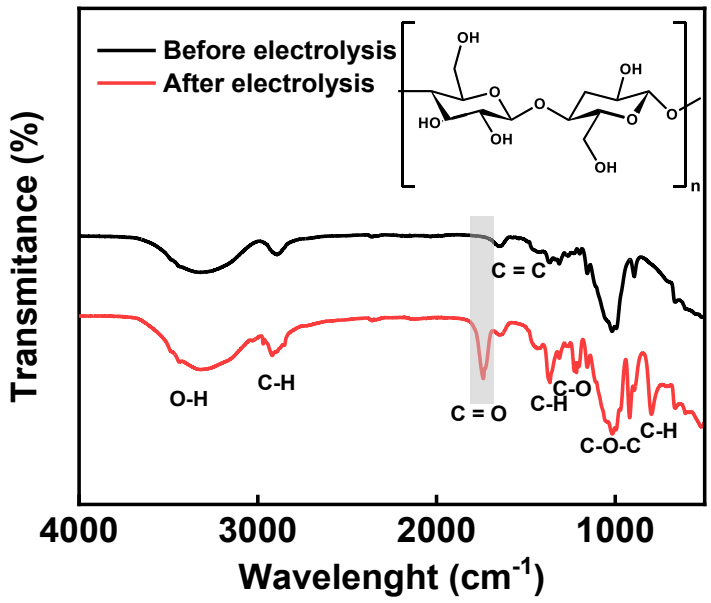

Figure 4.12. *Fourier transform infrared spectra of a regenerated cellulose dialysis membrane (before and after electrolysis) in a 0.5 M silicotungstic acid at 40 °C.*

Fourier-transform infrared (FTIR) spectroscopy of the regenerated cellulose dialysis membrane provides valuable insights into the chemical modifications induced by electrolysis. The spectrum of the membrane (before electrolysis) displays a broad O–H stretching band in the 3300–3700 cm^{-1} range, characteristic of hydroxyl groups commonly found in cellulose. Additionally, a distinct C–H stretching peak at 2895 cm^{-1} confirms the presence of aliphatic hydrogen atoms within the polymer backbone.

After electrolysis, slight but meaningful spectral shifts are observed. The C–O–C stretching band, typically located at 897 cm^{-1}, shifts slightly to 891 cm^{-1}, while the CH_2 bending vibration moves from 1423 cm^{-1} to 1419 cm^{-1}. These shifts suggest minor structural rearrangements or conformational changes in the cellulose membrane, possibly due to interactions with electrochemical species or the mediator. However, the most prominent spectral change after electrolysis is the development of a new peak at 1740 cm^{-1}, corresponding to the C=O stretching vibration.[23] This peak is indicative of carbonyl group formation, which strongly suggests oxidative modification of the cellulose structure under electrolysis conditions. The presence of carbonyl functionalities indicates partial oxidation of hydroxyl groups or ring-opening reactions within the glucose units of cellulose.[23]

Such oxidative transformations can compromise the integrity of the polymer linkage, leading to reduced mechanical strength and flexibility. This degradation mechanism aligns with observed losses in membrane robustness after electrolysis, highlighting the importance of controlling electrochemical conditions to preserve membrane performance. The FTIR data thus not only confirm chemical changes but also suggest an explanation for the membrane's physical deterioration.

Thermogravimetric analysis was employed to evaluate the thermal stability of the regenerated cellulose dialysis membrane before and after electrolysis. Thermogravimetric analysis curves of the regenerated cellulose dialysis membrane are shown in Fig. 4.13. The thermal degradation of the regenerated dialysis membrane after electrolysis reveals a distinct two-step degradation pattern. The first weight loss was observed at approximately 170 °C, attributed to the elimination of hydroxyl groups from the polymer structure, indicating the onset of chemical instability and the breakdown of hydroxyl groups.[23] The second, and more pronounced degradation phase occurs around 280 °C and is likely associated with the scission of the polymer's main chain, marking the collapse of the membrane's structural integrity.[23,26]

At lower temperatures, particularly in the range of 50–100 °C, the membrane demonstrates reasonable thermal stability. It shows a moderate weight loss of ~2.8% before electrolysis and ~2.3% after electrolysis, as illustrated in the inset graph of Fig. 4.12. This slight weight reduction suggests minimal moisture loss and indicates that the membrane's thermal strength is not severely compromised in this temperature range.

For comparison, Nafion, a benchmark material in electrochemical applications, exhibits a weight loss of approximately 3% at 100 °C and maintains structural stability up to 100–120 °C in its hydrated state.[26] The regenerated dialysis membrane's thermal behaviour up to 100 °C closely compares that of Nafion, highlighting its potential suitability for similar low-temperature electrochemical measurements. This comparable performance suggests that the regenerated dialysis membrane could serve as a cost-effective alternative to Nafion, particularly in applications where moderate thermal stability is sufficient.

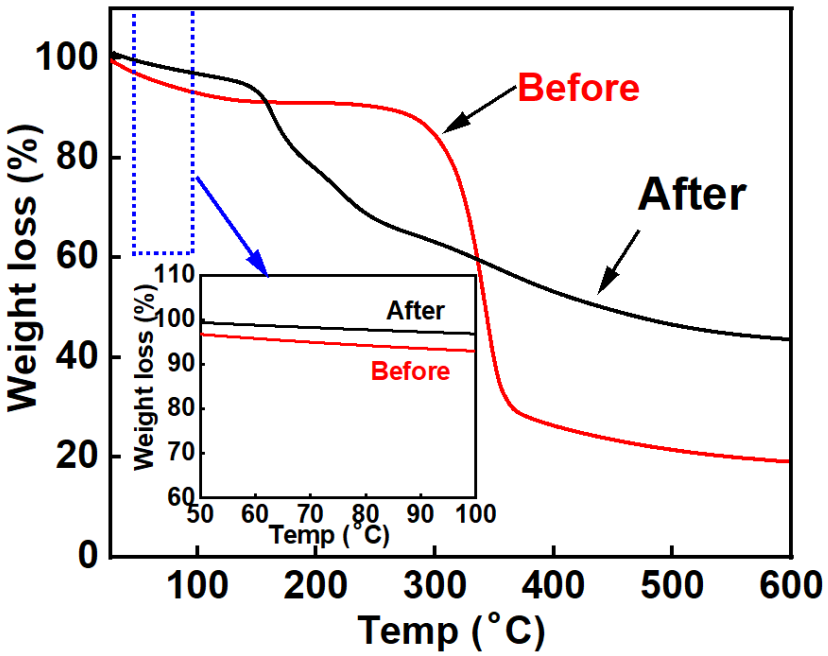

Figure 4.13. *Thermogravimetric analysis (TGA) curves of the regenerated cellulose dialysis membrane before (red line) and after (black line) electrolysis. The inset graph indicates the highlighted area corresponding to the low-temperature range (50–100 ℃).*

Water uptake is a crucial parameter for both proton transport and mechanical stability in proton exchange membranes.[19,20] Proton transport through the membrane requires significant water to coordinate with the protons. Water uptake increases with increasing ion exchange capacity. For example, the regenerated cellulose dialysis membrane had an ion-exchange capacity of 1.41 meq g^{-1} and a water uptake of 61%. Comparisons with other membranes depend on factors such as structural modifications and intended applications. For instance, cellulose triacetate membranes, which are also used in dialysis, have different biocompatibility characteristics.[19] In addition, the dialysis tubing made from regenerated cellulose typically has a molecular weight cut-off around 14,000 Da, which influences its permeability. [24]

The experimental ion-exchange capacity obtained in this work was broadly consistent with literature values,[24] indicating that most O-H groups interacted with H^+ ions during the electrolysis process. These IEC values suggest that the regenerated dialysis membrane exhibits moderate ion-exchange capability and is suitable for water splitting applications.[24] At the same time, its water uptake indicates good hydration properties, which can influence ion transport efficiency. Thus, sufficient water absorption generally promotes proton conduction, while excessive water uptake impairs the dimensional and oxidative stability of the membranes.[25] However, the water uptake does not seem to depend only on the ion exchange capacity value, but also on the porosity of the membranes. Makarov *et al*. suggested that water permeability is related to the size of membrane pores.[26] Therefore, compared to previous studies,[23,26] it is worth noting that the water permeability in the dialysis membrane in this study is due to the membrane pore size and porosity. The value shows an increasing trend with increasing hydrophilic chain length. The water retention of proton exchange membranes has a significant impact on their proton conductivity, particularly at high temperatures.[26]

5. Conclusions

In this work, we have demonstrated that decoupled electrolysis using liquid-phase mediators can be achieved in a flow system over a current density range of 25-500 mA/cm^2, with an oxygen-generating electrochemical cell using a simple cellulose-based size-exclusion membrane. Across this range of current densities, and despite the membrane's simplicity, the oxygen produced at the anode contained hydrogen levels that were well below the lower explosion limit for hydrogen in oxygen. This was possible because decoupled electrolysis allows hydrogen gas to be generated in an entirely separate device from the one producing oxygen, preventing hydrogen gas from forming inside the electrochemical cell that generates oxygen. However, our results also show that the type of membrane used in this work suffers from stability issues during electrolysis, especially at current densities above 500 mA/cm^2. That said, these results do suggest that there is scope to replace expensive and environmentally-damaging perfluorinated membranes in decoupled electrolysis systems with cheaper alternatives, without impacting on gas crossover and safety standards, by virtue of the fact that electrochemical decoupling prevents the gases from being made together inside the same electrochemical cell at the same time.

References

1. Q. Hassan, S. Algburi, A.Z. Sameen. *Energy Harvesting and Systems,* 2024, 11, 20220127.
2. R. Angelico, F. Giametta, B. Bianchi, P. Catalano. *Energies,* 2025, 18, 404.
3. Ifkovits, Z. P.; Evans, J. M.; Meier, M. C.; Papadantonakis, K. M.; Lewis, N. S. *Energy & Environmental Science,* 2021, *14*, 4740-4759.
4. P.J. McHugh, A.D. Stergiou, M.D. Symes. *Adv. Energy Mater,* 2020**,** 10, 200245.
5. G. Chisholm, L. Cronin, M. D. Symes. *Electrochimica Acta*, 2020, 331, 135255.
6. M. E. Obeten, Z. Ertekin and M. D. Symes. *Energy Fuels,* 2025, 39, 7129−7136.
7. B. Rausch, M.D. Symes, G. Chisholm, L. Cronin. *Science,* 2014, 345, 1326–1333.
8. A. Paul and Mark D. Symes. *Current Opinion in Green and Sustainable. Chemistry,* 2021, 29,100453.
9. I. Slobodkin, E. Davydova, M. Sananis, A. Breytus, A. Rothschild. *Nature Materials*, 2024, 23, 398–405.
10. Y. Liu, G.H. Wen, J. Liang, S.S. Bao, J. Wei, H. Wang, P. Zhang, M. Zhu, Q. Jia, J. Ma, L.M. Zheng. *ACS Energy Lett.* 2023, 8, 387−397.
11. A.A. Rand, S.A. Mabury. *Toxicology,* 2017, *375*, 28–36.
12. Symes, M. D.; Cronin, L. *Nature Chemistry,* 2013, *5*, 403-409.
13. M.T. de Groot, P. Vermeulen. *J. of Electroanalytical Chemistry,* 2024, 974, 118709.
14. Muralidharan VS. Warburg impedance - basics revisited. Anti-corrosion Methods & Mater 1997;44(1):26e9.
15. A.H. Faqeeh, and M. D. Symes. *Electrochimica Act,* 2023, 444, 14203–142036.
16. Babak Ghorbani, Jake DeVaal, Greg Afonso, and Krishna Vijayaraghavan. *Int. J. of Hydrogen Energy*, 2023, 48, 3264 –32671.
17. X. Huo, G. Shan, L. Yang, L. Gao, Y. Wang, M. Zhang, Y. Fu, W. Li, J. Zhang. *Int. J. of Hydrogen Energy,* 2024, 53, 684-697.
18. P. Millet, N. Mbemba, S.A. Grigoriev, V.N. Fateev, A. Aukauloo, C. Etiévant. *Int. J. of Hydrogen Energy*, 2011, 36, 4134-4142.

19. J. Wang, S.C. Abbas, L. Li, C.C. Walker, Y. Ni, Z. Cai. *Membranes*, 2024,14, 148–182.

20. P. Grzybek, G. Dudek, B. van der Bruggen. *Chemical Engineering Journal,* 2024, 495, 153500 – 153518.

21. M.A. Mohamed, W.N.W. Salleh, J. Jaafar, A.F. Ismail, M. Abd. Mutalib, S.M. Jamil. *J. of Applied Polymer Sci*, 2015, 1-10.

22. L. Zhang, D. Ruan, And J. Zhou. *Industrial & Engineering Chemistry Research,* 2001, 40, 5923-5928.

23. Y. Xie, A. Ringuette, D. Liu, J. Pang, H. Mutlu, D. Voll, P. Théato. *Eur. Polymer J.,* 2023, 186, 11183–11193.

24. I.S. Makarov, L.K. Golova, G.N. Bondarenko, T.S. Anokhina. *Membranes,* 2022, 12, 297-310.

CHAPTER FIVE

Final Conclusion and Future Recommendations

5.1. Final Conclusion

The work presented in this thesis explores in detail the use of silicotungstic acid as a redox mediator in decoupled electrochemical water splitting for hydrogen production.

In Chapter 1, we introduced sustainable hydrogen production from renewable energy sources, as well as electrochemical hydrogen production, and the use of redox mediators in hydrogen production, along with the potential benefits associated with this technology. The global shift to renewable energy requires an effective method of energy storage when intermittent renewable sources (e.g., wind, solar) are unavailable.[1,2] Decoupled electrolytic water splitting is a potential solution to this problem, storing renewable energy as hydrogen fuel. The use of redox mediators in water splitting offers potential advantages in terms of electrolyser and component degradation processes, as well as reduced gas crossover.[3] We also discussed the primary factors behind the effectiveness of this approach, such as stability, reversibility, redox potential, cyclability, availability, cost, and the influence of the background electrolyte. Then, using examples reported in recent literature, we demonstrated how this approach is an attractive route to producing pure hydrogen.

In Chapter 3, we revisited this concept, employing silicotungstic acid ($H_4SiW_{12}O_{40}$) as the redox mediator at various current densities (50–1.35 mA/cm^2). We achieved a high decoupling efficiency of ~99.9% for each set of applied current densities after 5 hours. This was accomplished using a Pt/C cathode catalyst (in the cell producing hydrogen) and a Ti fibre felt coated with IrO_2 as the anode catalyst (in the cell producing oxygen) at 40 °C. One of the aims of this study was to investigate the decoupling efficacy of this process at more commercially attractive current densities than those previously used. Decoupled electrolysis was then performed, with the catalyst spread directly onto the gas diffusion layer at the anode rather than on a commercial catalyst-coated membrane (CCM). The anode catalyst performed well, with negligible (<0.2%) H_2% in the anode stream, when applied directly onto the gas diffusion layer. The promising results presented in this chapter demonstrate that decoupled water electrolysis can be utilised to prevent gas mixing across a wide range of current densities.

In Chapter 4, we reported the first application of a novel regenerated cellulose dialysis membrane for use in decoupled electrolysers. The membrane was employed as a separator in decoupled electrolytic water splitting to generate hydrogen and oxygen. It was found that the

membrane could not tolerate current densities above 500 mA/cm^2 and exhibited very high resistance.

SEM/EDX imaging of the membrane revealed significant morphological changes after electrolysis, characterised by extensive cracks. Meanwhile, AFM measurements showed a substantial increase in the mean roughness (R_a) after electrolysis. Comparison of FTIR spectra recorded on membrane samples before and after electrolysis revealed that the peaks associated with the terminal C-H stretches in the hydroxyl groups were not present in the used membrane (i.e., after electrolysis), seemingly confirming this deterioration. In Section 5.2, we suggest an alternative monomer that may be more resistant to this degradation mechanism, thereby improving membrane robustness during production. The work in this chapter highlighted that decoupled electrolysis works with this membrane and produces oxygen with suitably low levels of hydrogen. However, it is also apparent that much work needs to be done to optimise the membrane to improve its performance.

In all the examples cited across both chapters (3 & 4), the studies were performed on a laboratory scale; therefore, widespread implementation of this technique would require a significant scaling up of the process and, since the performance of the method is heavily reliant on the choice of mediator, it is evident that this approach is suited to less expensive mediators to scale up for commercialisation. As mentioned in Section 1.4, energy consumption may also hinder the widespread adoption of this approach. Reducing this energy cost will likely be a focal point for future investigations in this field.

5.2. Future Recommendations

Decoupled electrochemical water electrolysis offers a key advantage by separating the production of hydrogen and oxygen, a promising feature for renewable hydrogen applications. Recent studies have also demonstrated that a decoupled electrolysis system is not limited to water splitting but can also be applied to other organic transformations, indicating its broad applicability in various fields.[3] However, several challenges limit its commercial potential: the long-term durability of redox mediators and their compatibility with cell components (e.g., membranes, electrodes) remain uncertain. For membranes in water splitting, research should focus on polyimides, polyether ketone, and polyethene, among others, to lower membrane resistance and make them economically viable.[4] Future research should prioritise the synthesis and characterisation of polymers that offer enhanced ionic conductivity, greater chemical resilience under operational conditions, and compatibility with scalable manufacturing processes. Similarly, emphasis should be placed on new recyclable polymers that are more biodegradable and that reduce environmental impact, aligning with circular economy principles.

Continuous cycling of the mediator can lead to mediator degradation, structural failure, and reduced activity. The decoupled systems often require additional pumps and flow circuits, a key contribution to cost, and may use viscous decoupling agents, making them more complex than conventional electrolysis setups. Current decoupled technologies fall short of traditional systems in terms of efficiency. Improvements are needed in electrocatalyst performance, device architecture, and electrolyte conductivity. To enable real-world deployment, it is essential to demonstrate long-term stability, understand degradation pathways, and perform rigorous failure analysis. Pilot-scale testing and cost optimisation are also critical for commercial viability. Additionally, as interest continues to grow in leveraging redox mediators for various electrochemical processes, it is anticipated that future studies should focus on the synthesis and design of a broader array of cost-effective mediators for investigation across both aqueous and non-aqueous systems, thereby enhancing green hydrogen production.

References

1. B.S. Zainal, P.J. Ker, H. Mohamed, H.C. Ong, I.M.R. Fattah, S.M.A. Rahman, L.D. Nghiem, T.M.I. Mahlia. *Ren. and Sust. Energy Reviews*, 2024, 189, 113941.
2. M. Jaradat, S. Almashaileh, C. Bendea, A. Juaidi. *Energies,* 2024, *17*, 3992.
3. G. Chisholm, L. Cronin, M. D. Symes. *Electrochimica Acta*, 2020, 331, 135255.
4. X. Liu, J. Chi, B. Dong, Y. Sun. *ChemElectroChem,* 2019, 6, 2157 – 2166

Appendix

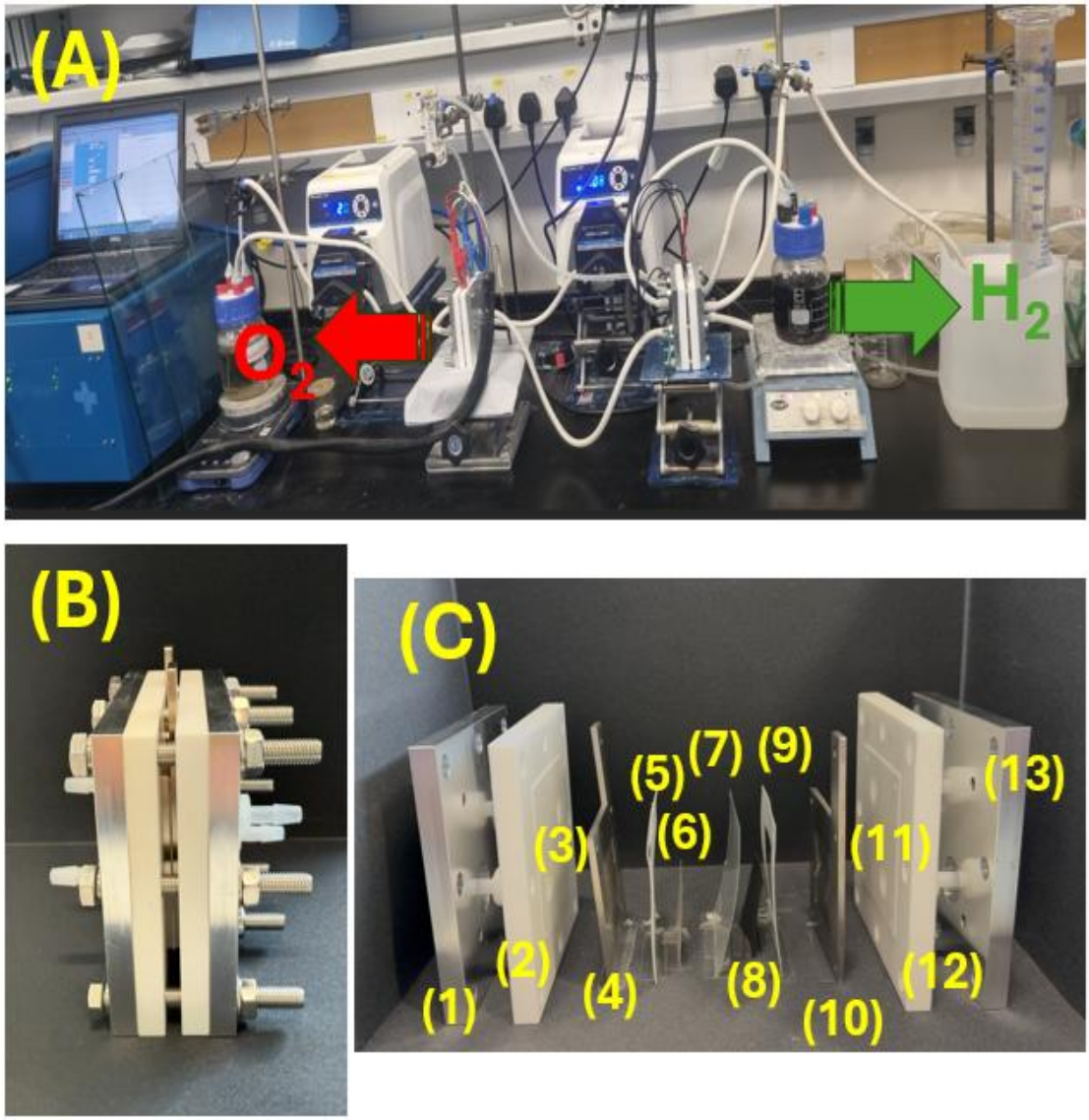

Appendix 1. *(a) Overall electrochemical flow cell setup. (b) Photograph of the individual electrochemical cell used in the system. (c) Simplified exploded view of the components used to assemble both the oxygen- and hydrogen-generating electrochemical flow cells, as described in the main text and listed in Table 2.1.*

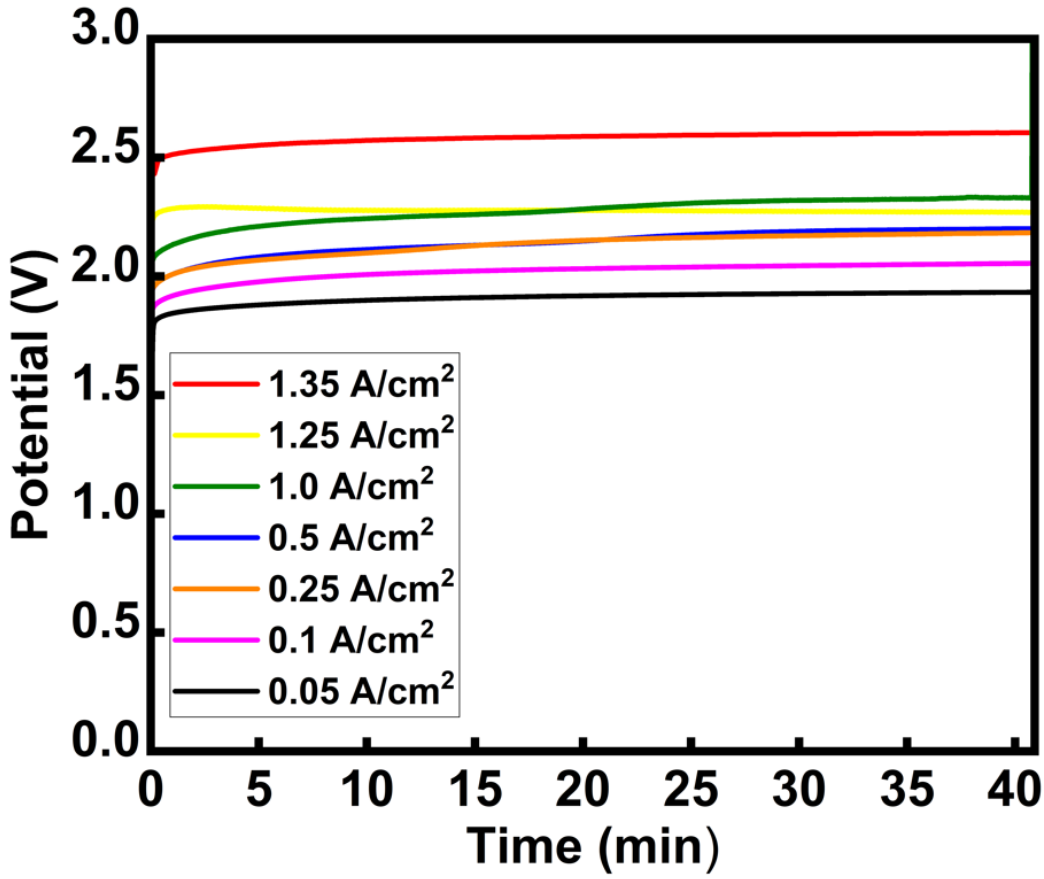

Appendix 2. *Potential-Time curve for the Reoxidation of the mediator at the cell making hydrogen (HER) at 41 minutes with Nafion membrane and at a flow rate of 250 mL/min. In all cases, the mediator was reoxidized at a fixed current of 100 mA/cm², which is the same current used in the initial (Reduction/charging) stage of the mediator.*

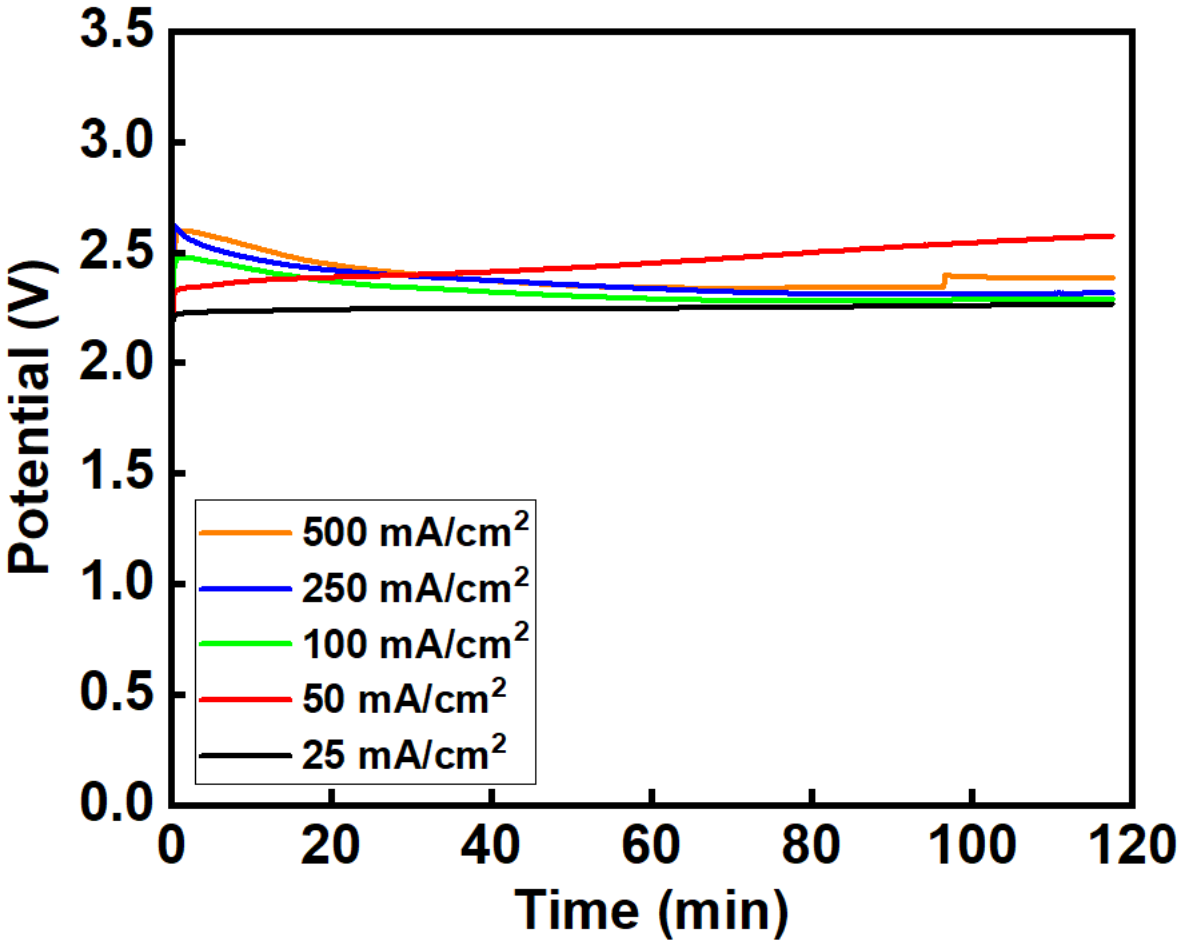

Appendix 3. *Potential-Time curve for the Reoxidation of the mediator at the cell making hydrogen (HER) until 4824 C was passed (taking approximately 117.4 minutes) at a cathodic flow rate of 250 mL/min. In all cases, the mediator was reoxidised at a fixed current density of 50 mA/cm^2, the same current used during the initial (Reduction/charging) stage.*

The cell voltages of the dialysis membrane exhibit similar behaviour to Nafion over the range of current densities applied.

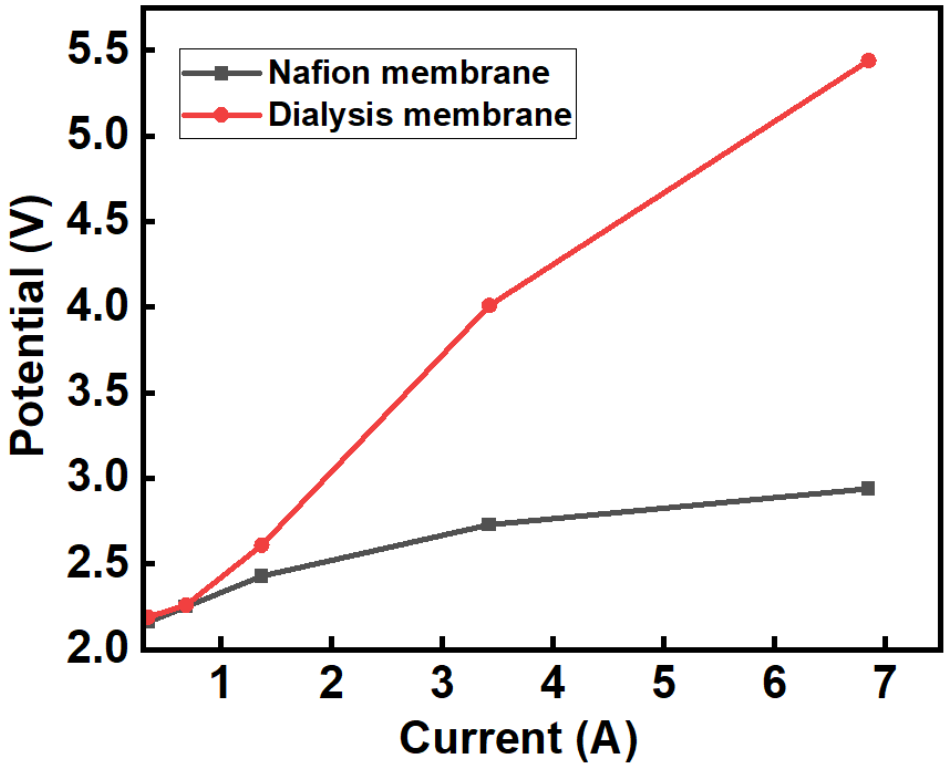

Appendix 4. *Comparison of the cell voltages obtained with a Nafion membrane and a dialysis membrane in the cell making hydrogen (HER) after 5 hours at a cathodic flow rate of 250 mL/min during steady-state operation.*

Mediator After Experiment **Mediator turns colourless after Re-oxidation**

Appendix 5. *How the colour of the mediator changes from dark blue (after experiment) to colourless after Re-oxidation. In all cases, the mediator was reoxidised at a fixed current density of 50 mA/cm^{2,} the same current used during the initial (Reduction/charging) stage.*